



저작자표시-비영리-변경금지 2.0 대한민국

이용자는 아래의 조건을 따르는 경우에 한하여 자유롭게

- 이 저작물을 복제, 배포, 전송, 전시, 공연 및 방송할 수 있습니다.

다음과 같은 조건을 따라야 합니다:



저작자표시. 귀하는 원저작자를 표시하여야 합니다.



비영리. 귀하는 이 저작물을 영리 목적으로 이용할 수 없습니다.



변경금지. 귀하는 이 저작물을 개작, 변형 또는 가공할 수 없습니다.

- 귀하는, 이 저작물의 재이용이나 배포의 경우, 이 저작물에 적용된 이용허락조건을 명확하게 나타내어야 합니다.
- 저작권자로부터 별도의 허가를 받으면 이러한 조건들은 적용되지 않습니다.

저작권법에 따른 이용자의 권리는 위의 내용에 의하여 영향을 받지 않습니다.

이것은 [이용허락규약\(Legal Code\)](#)을 이해하기 쉽게 요약한 것입니다.

[Disclaimer](#)

이학박사 학위논문

Topological ladders for neutral atoms in a
resonantly driven 1D optical lattice

공진하는 일차원 광격자 내 중성원자를 이용한 위상 사다리 연구

2020년 8월

서울대학교 대학원

물리 · 천문 학부

강 진 현

Topological ladders for neutral atoms in a resonantly driven 1D optical lattice

by

Jin Hyoun Kang, M.S.

Dissertation

Submitted to the Department of Physics & Astronomy
in partial fulfillment of the requirements for the degree of

Doctor of Philosophy

Seoul National University

August 2020

Abstract

Topological ladders for neutral atoms in a resonantly driven 1D optical lattice

Jin Hyoun Kang

Department of Physics and Astronomy
The Graduate School of
Seoul National University

The phases of matter have been mostly associated with symmetry breaking according to Landau theory. However, the discovery of the quantum Hall effect has brought about a new paradigm of classification. The quantum Hall states do not break any symmetry, but their phases are classified by their topological invariants of band structure. Featuring with fundamental physical properties that are determined by its topological invariant and insensitive to the microscopic details, the topological states of matter represent the frontiers of modern condensed matter physics.

Complex quantum many-body systems, such as correlated topological insulators, represent one of the challenging problems in modern physics. Ultracold atoms in optical lattices provide an ideal experimental platform for studying correlated topological physics due to its good isolation from environment and high experimental controllability including interactions. Referring to various well-known lattice models such as the Harper-Hofstadter model and Haldane model, topological bands can be generated in optical lattice systems by introducing strong magnetic field or next-nearest-neighbor tunneling. In this thesis, I describe a series of experimental works where we generate topological

ladders in an 1D optical lattice system via resonant modulations of the lattice potential. Taking Bloch states as a synthetic dimension, ladder models can be constructed with real 1D optical lattice sites.

Generation of complex tunneling phases between Bloch states are demonstrated by introducing moving optical lattice on the static optical lattice. When an atom hops around a unit cell in this synthetic ladder, it acquires non-zero quantum phase, which is equivalent to the Aharonov-Bohm phase accumulated on a charged particle in a magnetic field. The artificial gauge field result in a Harper-Hofstadter like model by breaking time-reversal symmetry. Using band state and momentum resolved measurements, the chiral ground state was directly observed, and its stability was also investigated. The quench dynamics of the system showed the strong uniform gauge field in the ladder system, and the momentum dependent quench dynamics demonstrated the characteristic next-nearest-neighbor tunneling in the synthetic ladder system.

Creutz ladder is demonstrated in a 1D optical lattice by resonantly driving the lattice position. When the shaking frequency reaches half of the energy difference between two band states, two-photon resonant process leads to band-state changing nearest-neighbor tunneling, which is equivalent to next-nearest-neighbor tunneling in ladder description. This diagonal tunneling leads to winding structure of pseudospin through the Brillouin zone, and formation of topological end states. Measured resonant frequency and interferometry results clearly showed the topological pseudospin winding structure of the driven lattice system. Moreover, a two-tone driving scheme, where the 1D optical lattice is driven by two harmonic frequencies, is proposed for realization of topological charge pumping in the driven lattice system.

Keywords : Ultracold atom, Optical lattice, Floquet engineering, Topological insulator, Topological ladder, Topological charge pump

Student number : 2015-30971

Contents

Abstract	i
List of Figures	vii
Chapter 1 Introduction	1
1.1 Quantum simulator	1
1.2 Topology in condensed matter	3
1.3 Ultracold atoms in optical lattices and topological band engineering	7
1.4 Outline of the thesis	8
Chapter 2 Overview of the experimental setup	11
2.1 Electronic structure of Yb and laser	12
2.1.1 Electronic structure	12
2.1.2 Laser system	14
2.2 Producing degenerate Fermi gas	25
2.2.1 Cooling procedures	25
2.3 Manipulation of nuclear spin states	32
2.4 Optical lattice	36
2.5 Two-photon Raman transition	39

2.6	Periodic shaking of optical lattice	42
Chapter 3	Floquet theory and stroboscopic dynamics	46
3.1	Floquet formalism	47
3.2	Perturbative inverse frequency expansion	49
3.3	Driven optical lattices	55
Chapter 4	Topological insulator	61
4.1	Harper-Hofstadter model	62
4.2	1D topological system	68
4.2.1	Su-Schrieffer-Heeger model	68
4.2.2	Creutz ladder	71
4.3	Synthetic dimension and topological ladders	73
Chapter 5	Cross-linked chiral Hall ladder with band states	76
5.1	Introduction	77
5.2	Experimental setup	78
5.3	Effective Hamiltonian	80
5.4	Ground state and chiral current	86
5.5	Quench dynamics in cross-linked chiral ladder	91
5.6	Topological phase transition	94
5.7	Conclusion	96
Chapter 6	Topological ladder in resonantly driven optical lattice	98
6.1	Introduction	99
6.2	Creutz ladder	101
6.3	Atom in a resonantly shaken optical lattice	102
6.4	Experiment and result	107

6.4.1	Experimental setup	107
6.4.2	Shaking spectroscopy	108
6.4.3	Ramsey interferometry	111
6.5	Discussions	116
6.5.1	Off-resonance coupling effect	116
6.5.2	Shaking with two resonant frequencies	118
6.6	Conclusion	120
Chapter 7 Topological pumping in resonantly driven optical lat-		
	tice	122
7.1	Introduction	123
7.2	Resonantly shaken optical lattice	124
7.2.1	Two-band model description	124
7.2.2	Effective static description	126
7.3	Topological properties and micromotions	128
7.3.1	Edge states and symmetry	129
7.3.2	Micromotions	131
7.4	Topological charge pumping	134
7.5	Discussions	137
7.6	Summary	140
Chapter 8 Conclusions and Outlook		142
초 록		171

List of Figures

1.1	Schematic illustration of quantum simulator.	2
2.1	Electronic structure of ytterbium atom frequently used in ultra-cold atom experiments.	12
2.2	Hyperfine structure of the $^1S_0 \rightarrow ^1P_1$ and $^1S_0 \rightarrow ^3P_1$ transitions for ^{173}Yb	13
2.3	View of laser table for Yb machine in QGL.	15
2.4	Schematic of the 398.9 nm blue laser system.	16
2.5	Schematic of the 555.8 nm green laser system.	21
2.6	Schematic of the IR laser ODT and transport system.	23
2.7	Schematic of the ODT and optical lattice setup at science chamber.	24
2.8	Photo of the fermionic ^{173}Yb magneto optical trap (MOT) during the loading at the main chamber.	26
2.9	Harmonic trap frequency measurement.	29
2.10	^{173}Yb degenerate Fermi gas with six spin states.	32
2.11	Schematic of the optical Stern-Gerlach method.	33
2.12	Schematic sequence of band-mapping process.	38
2.13	Two-photon Raman transition.	40
2.14	Piezo mirror system	45

3.1	Dynamics of two-level system under the resonant modulation. . .	54
4.1	Schematic drawing of Harper-Hofstadter model.	63
4.2	Energy spectrum of Harper-Hofstadter model at $\Phi = \pi/2$	67
4.3	Schematic diagram of Su-Schrieffer-Heeger model.	70
4.4	Concept of synthetic dimension.	74
5.1	Experimental setup for optical lattice and Raman coupling. . . .	79
5.2	Orbital-momentum coupling in an optical lattice.	82
5.3	Raman coupling coefficients C_α^l and S_α^l ($l = 0, 1$) as functions of k_R/k_L	84
5.4	Energy structures of the ladder system.	88
5.5	Experimental sequence for adiabatic loading and imaging of the synthetic ladder system.	89
5.6	Chiral currents in the fermionic three-leg ladder.	90
5.7	Quench dynamics of the ladder system and effects of the complex cross links.	93
5.8	Zak phase γ_Z of the ground band of the three-leg ladder system.	95
5.9	Topological phase transition of the three-leg ladder system. . .	95
6.1	Creutz ladder model.	101
6.2	Creutz ladder in a resonantly shaken optical lattice.	104
6.3	Shaking spectroscopy of fermionic atoms in an optical lattice. .	109
6.4	Schematic of Ramsey interferometry using two separate pulses of lattice shaking.	110
6.5	Momentum-resolved Ramsey interferometry signal.	113
6.6	Driving phase dependence of the Ramsey fringe signal.	115

6.7	Characterization of the Ramsey fringe signals.	117
6.8	Topological charge pumping in the Creutz ladder.	119
7.1	Effective ladder model of resonantly shaken optical lattice. . . .	127
7.2	Quasienergy spectrum of shaken 1D optical lattice of length $L =$ 150.	130
7.3	Zak phase of lower Floquet band γ_- in parameter space $\{x_{2\omega}, \varphi\}$. .	133
7.4	Example of topological pumping trajectory with $\varphi(t) = \varphi^0 +$ $\frac{\pi}{4} \sin(2\pi t/T_p)$, $x_{2\omega}(t) = x_{2\omega}^c + x_{2\omega}^m \cos(2\pi t/T_p)$	134
7.5	Numerically calculated pumped charge.	136
7.6	Dispersion of double well optical lattice as a function of V_1 , at $V_0 = 8E_r$	139

Chapter 1

Introduction

1.1 Quantum simulator

Simulating quantum mechanic problem has been regarded as a challenging problem, because of exponentially increasing computational cost. For example, a simple localized spin-half system with size N has 2^N different quantum states, and one must consider all of these states to expect ground state. In condensed matter, quantum statistics and interparticle interactions make quantum systems more complex. As the huge capacity of memory is required to store exponentially large number of quantum states, complex quantum systems are difficult to be understood with conventional computers, although its computing power increases gradually.

Ingenious cocept has been come out to solve the problem, which is referred as *quantum computer*. The key idea is employing quantum mechanical elements to calculate quantum mechanical problems [1]. These systems can store exponenetially large amount of information with smaller number of ele-

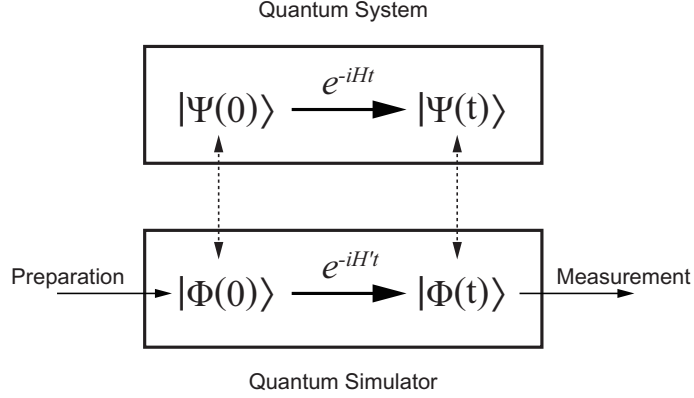


Figure 1.1: Schematic illustration of quantum simulator. The model quantum system, composed of wave function $|\Psi\rangle$ and Hamiltonian H , is directly mapped onto the wave function and Hamiltonian of quantum simulator, $|\Phi\rangle$ and H' . By preparing initial state $|\Phi(0)\rangle$ and measuring final state $|\Phi(t)\rangle$, evolved by Hamiltonian H' , model quantum system can be simulated.

ments compared to the conventional computers, so it is suitable for investigating complex quantum systems. For example, today's state of the art quantum processor with 53 qubits demonstrated quantum supremacy [2], where a quantum computer can solve a problem that is impossible for classical computer [3, 4]. Quantum computers rely on qubits rather than bits, and they can approach any quantum problems if their quantum gates are universal: different quantum simulations can be run by just changing the programs [5, 6]. General purpose quantum computers require high-fidelity, error-corrected logical gates composed of multiple qubits, and these requirements have been accomplished step by step, but many obstacles must be overcome [7–9].

In the middle of development of fully fledged quantum computers, interesting quantum physics can be explored by *quantum simulator* [10–13]. Quantum simulator is rather kind of problem-specific analog simulator, which employs simpler and intuitive quantum mechanical elements [14]. The Hamiltonian

of the interesting quantum system can be directly mapped onto the Hamiltonian of quantum simulator [15–19]. In spite of its simple structure, these toy models are powerful toolbox for studying difficult problems, such as high T_c superconductivity [10, 20], quantum magnetism [21–23], and quantum phase transitions [19, 24, 25].

1.2 Topology in condensed matter

Topology is concerned with invariant properties under the smooth deformations. Typically, the invariant properties are global properties rather than local property. One of examples is the Gauss-Bonnet theorem, which states the relation between curvature and the number of holes in a two-dimensional surface,

$$\frac{1}{2\pi} \int_S dA K = \chi(S) = 2(1 - g), \quad (1.1)$$

where K is Gaussian curvature and $\chi(S)$ is Euler characteristic of the surface S . Regardless of the local curvature, the net curvature of object has direct relation to the the number of holes, or *genus* g . For example, the coffee mug and torus have one hole in the surface ($g = 1$), so these are topologically equivalent. However, they cannot be smoothly deformed to the spherical cow ($g = 0$). Thus, topological objects can be classified by the *topological invariant*, such as genus g [26].

Topology in condensed matter is recognized after the discovery of the quantum Hall effect in 1980 [27, 28]. The integer quantum Hall effect arises when a 2D electron gas (2DEG) is under the strong magnetic field at low temperature. If the interaction between electrons are negligible, the Hamiltonian of 2DEG

under the constant magnetic field B is given by

$$\hat{H} = \frac{1}{2m}(p + eA)^2 = \frac{m}{2}v^2, \quad (1.2)$$

where p is the momentum operator, m is mass of electron, and A is the vector potential, and $v = [p + (e/c)A]/m$. Then the Hamiltonian can be written in the ladder operators in harmonic oscillators,

$$\hat{H} = \hbar\omega_c \left(a^\dagger a + \frac{1}{2} \right), \quad (1.3)$$

where

$$\begin{aligned} a &= \sqrt{\frac{m}{2\hbar\omega_c}}(v_x + iv_y), \\ a^\dagger &= \sqrt{\frac{m}{2\hbar\omega_c}}(v_x - iv_y), \end{aligned} \quad (1.4)$$

and $\omega_c = eB/m$ is cyclotron frequency. Then the energy spectrum is given by discrete levels,

$$E_n = \hbar\omega_c \left(n + \frac{1}{2} \right), \text{ with } n \in \mathbb{Z}^{\geq}, \quad (1.5)$$

and these are called the n th *Landau level*. Landau levels are highly degenerate as the number of states in area A is

$$N = \frac{A}{2\pi l_B^2} = \frac{eBA}{2\pi\hbar} = \frac{\Phi}{\Phi_0} \quad (1.6)$$

where $l_B = \sqrt{\hbar/eB}$ is the magnetic length, and $\Phi_0 = 2\pi\hbar/e$ is flux quantum and $\Phi = AB$ is the total flux on the sample. These Landau levels are separated by $\hbar\omega_c$, so it becomes insulating phase when the Fermi energy is located at the energy gap. However, it shows intriguing properties at the interface: the chiral conducting states at the edge of the system because of bending of Landau levels, while the bulk is insulator. In the semi-classical picture, the chiral states can be

understood as a skipping orbit motion at the edge under the strong magnetic field. Because of these chiral states, Hall currents are expected.

Unexpectedly, Hall conductivity was exactly quantized to integer multiples of fundamental conductance unit e^2/h . The value of quantized Hall conductivity is not altered by the geometry of the system, impurities, disorder, and it is even same in different type of materials. The robustness against the perturbations implies that the quantum Hall effect has topological nature, which was first explained by Thouless, Kohmoto, Nightingale and Nijs [29]. According to TKNN, the Hall conductivity can be described by winding of phase of the eigenstates around the 2D Brillouin zone,

$$\begin{aligned}\sigma_{xy} &= \frac{ie^2}{\hbar} \sum_j \int_{\text{BZ}} \frac{d^2k}{(2\pi)^2} \left[\left\langle \frac{\partial u}{\partial k_1} \middle| \frac{\partial u}{\partial k_2} \right\rangle - \left\langle \frac{\partial u}{\partial k_2} \middle| \frac{\partial u}{\partial k_1} \right\rangle \right] \\ &= \frac{e^2}{\hbar} \sum_j \int_{\text{BZ}} \frac{d^2k}{(2\pi)^2} \Omega_j(\mathbf{k}),\end{aligned}\tag{1.7}$$

where j is index of filled bands, and the $\Omega_j(\mathbf{k})$ is referred as *Berry curvature* later [30]. Because Brillouin zone is closed surface, the integral of Berry curvature over the Brillouin zone is given by the topological invariant, the *Chern number* C ,

$$C = \frac{1}{2\pi} \int_{\text{BZ}} d^2k \, \Omega(\mathbf{k}),\tag{1.8}$$

where the Chern number is always given by integer $C \in \mathbb{Z}$. Then the Hall conductivity is given by

$$\sigma_{xy} = \frac{e^2}{h} \sum_j C_j.\tag{1.9}$$

Therefore, the Hall conductivity is determined by topological invariant of filled bands. Because Chern number cannot be continuously changed, Hall conductivity shows a plateau until the abrupt change of topology. This explains the robustness of the Hall current at the edge.

The quantum Hall effect is an example of general class of materials that are referred as *topological insulators*. It was first believed that topological states can only exist by breaking time-reversal symmetry with external magnetic field, but after the proposal of quantum Hall states without magnetic field by Haldane [31], many types of topological insulators have been proposed and classified by its symmetry [32–34]. A key feature of the topological insulators is the *topologically protected edge states* at the boundary of the finite system. The edge states exists because of non-trivial topology of the bulk bands, which is called *bulk-boundary correspondence*.

The mathematical connection of topological insulators can be explained in single-particle description. It becomes complicated when the interaction plays major role in the system. The famous example is the fractional quantum Hall effect (FQHE), where the Hall current shows plateaus at fractional values of fundamental conductance unit e^2/h [35, 36]. The electron-electron interaction is responsible for fractionally charged quasiparticle, which cannot be understood in single-particle description. The discovery of FQHE has led to fractional statistics and people has been concerned with many-body topological states. However, because of complexity of the system, the exact solutions are not much known, and numerical simulations are also limited by the capacity of computational resource. Therefore, quantum simulation could be effective tool for studying exotic topological matters.

1.3 Ultracold atoms in optical lattices and topological band engineering

Ultracold atoms are dilute gas of neutral atoms, whose temperature are kept below the regime where the quantum mechanical properties become important. Over the past few decades, it has allowed the observation of Bose-Einstein condensation (BEC) [37–39] and degenerated Fermi gas [40–42], opening a new avenue in quantum simulation. It is an useful platform to study many-body physics in condensed matter, as interaction strength can be easily tuned in the periodic potential generated by interference between laser beams [43–45]. For example, Hubbard model contains quantum tunneling and on-site interactions can be demonstrated with ultracold atoms in optical lattice [16, 46, 47], and the quantum phase transition between superfluid to Mott insulator was directly demonstrated [19]. In this platform, kinetic energy and interaction strength can be fully tunable. Because of an exceptional experimental controllability, ultracold atoms in optical lattices would be also promising candidate for simulating topological states [48]. Band structures and interactions between atoms are highly tunable, offering opportunities for the realization of exotic topological phases of matter. Also, new detection techniques may provide a different point of view on underlying physics in conventional solid-state experiments [49–54].

However, ultracold atoms are charge neutral, so their dynamics under the electromagnetism fields is different to the electrons: a vector potential on atoms produced by external magnetic field would be negligible. Also, a complex geometry of periodic potential is hard to be constructed by laser interference only. The dynamics in optical lattice is mainly governed by the nearest-neighbor hopping, and higher order terms are difficult to be controlled independently. For

example, simple geometries, such as hexagonal lattices, can be easily obtained by monochromatic laser, and even Lieb [55] and Kagome lattice [56] can be generated by bichromatic fields, but lattices containing more than nearest-neighbor hopping, such as Mielke checkerboard lattice [57, 58], has not been much realized in a static optical lattice setup.

These limitations can be overcome by various experimental techniques. Rather than using external magnetic field, *artificial gauge field* was demonstrated by a rotation of the system [59] or laser-assisted tunneling [60]. For the latter method, a uniform flux of gauge field realized the Harper-Hofstadter model [61, 62], which is a lattice version of the integer quantum Hall effect [63–65]. In addition, the Haldane model was first demonstrated in a circularly shaken honeycomb optical lattice [66], which is a famous example of the quantum anomalous Hall effect, but had not been founded in nature [31]. It was recently realized in condensed matter system [67] as originally proposed by Oka and Aoki [68]. These topological bands can be efficiently engineered by periodic modulations, which are often referred as *Floquet engineering*.

1.4 Outline of the thesis

In this thesis, topological ladders are demonstrated with resonantly modulated 1D optical lattice. The structure of the thesis is given as below.

First, a brief overview of the apparatus for the production of Yb quantum gas used in this thesis is provided in Chapter 2. The configuration of the setup and experimental techniques will be described.

Chapter 3 provides an introduction of Floquet theory, and perturbative expansion methods to find simple description of effective Hamiltonian. This will

be illustrated with a two-states model and 1D optical lattice.

Theoretical background of topology and examples of model Hamiltonians for topological states are considered in Chapter 4. Topological ladders realized in 1D optical lattice based on synthetic dimension concept will be also discussed in this chapter.

The first demonstration of Hall ladder using band states of a 1D optical lattice is presented in Chapter 5. The band states are regarded as individual sites, and interband couplings are considered as hopping terms between these sites. Because of on-site energy modulation, atoms acquire quantum phase when the initial band state is converted to another band state. As a consequence, the dynamics of the system can be effectively described ladder under the arbitrary gauge field. It is equivalent to the Hofstadter Hamiltonian with finite lattice sites in synthetic dimension. In this system, ground states are chiral, which is an analogue of chiral Hall current in integer quantum Hall effect.

The demonstration of Creutz ladder in a resonantly shaken 1D optical lattice is shown in Chapter 6. The periodic shaking of lattice position can induce dynamical localization, but the resonant shaking can lead to topological states by a next-nearest-neighbor hopping in ladder description. The interband couplings can be described by resonant processes occurred by 'photon', analogous to the excitation in solid-state sample under the electromagnetic field. In this point of view, interband couplings can occur by absorbing or emitting n -photons when the integer multiples of modulation frequency is equivalent to the energy gap between band states. Particularly, a 2-photon process leads neighbor-hopping interband coupling, which can be described by a next-nearest-neighbor hopping in ladder. An interferometric measurement scheme is demonstrated to infer the winding structure of the effective Hamiltonian.

As an extension of Chapter 6, 1D optical lattice driven by two harmonic frequencies will be discussed in Chapter 7. The change of driving amplitude and a relative phase of two harmonic resonant drivings lead to topological pumping. Effective Hamiltonian descriptions and micromotions of the system will be discussed. Particularly, a pseudo-spin winding, or Zak phase of the system depends on the stroboscopic timeframe. The symmetry of the time-dependent Hamiltonian will be also considered in this chapter.

Finally, a summary of the thesis and outlooks for future directions will be considered in chapter 8.

Chapter 2

Overview of the experimental setup

The experiments in this thesis were performed with fermionic ^{173}Yb atoms. ^{173}Yb atoms were cooled down to quantum degeneracy regime, corresponding to about 60 nK in our optical trap, and loaded into the optical lattice. The ytterbium machine had been mainly developed by Min-Seok Kim, Moosong Lee, and Jeong Ho Han [69]. During my first year of PhD course, degenerate Fermi gas was achieved, and first experiment with degenerate fermionic ^{173}Yb atoms were reported [70]. In this section, I will look through basic properties of ytterbium, laser cooling, and experimental apparatus and techniques.

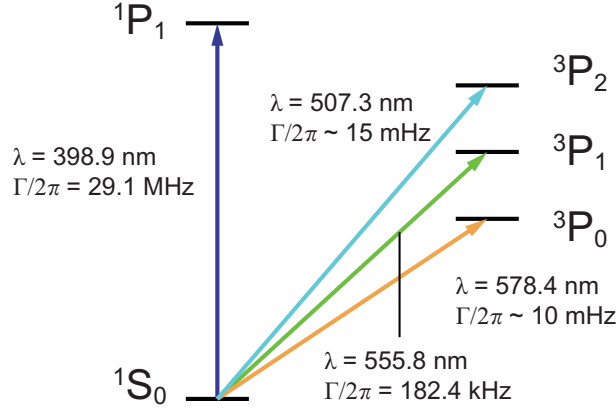


Figure 2.1: Electronic structure of ytterbium atom frequently used in ultracold atom experiments. Natural linewidth of each transition Γ is noted. $1S_0 \rightarrow 1P_1$ transition is employed for Zeeman slowing and absorption imaging, and $1S_0 \rightarrow 3P_1$ transition is used for magneto-optical trap (MOT) and spin manipulations.

2.1 Electronic structure of Yb and laser

2.1.1 Electronic structure

Ytterbium is a rare-earth element in the lanthanide series. Because of closed-shell electronic configuration $[\text{Xe}]4f^{14}6s^2$, two valence electrons in s-shell mostly determines its electronic property similar to alkaline-earth atoms. Ytterbium naturally occurs in stable isotopes with zero nuclear spin ($I = 0$; ^{168}Yb , ^{170}Yb , ^{172}Yb , ^{174}Yb , ^{176}Yb) or non-zero nuclear spin ($I = 1/2$; ^{171}Yb , $I = 5/2$; ^{173}Yb): the formers are bosonic while the latters are fermionic.

The electronic structure of ytterbium can be described by LS -coupling scheme, where the total electronic angular momentum is given by the combination of total orbital angular momentum \mathbf{L} and total spin angular momentum \mathbf{S} . Total electronic angular momentum is given by $\mathbf{J} = \mathbf{L} + \mathbf{S}$, and electronic levels

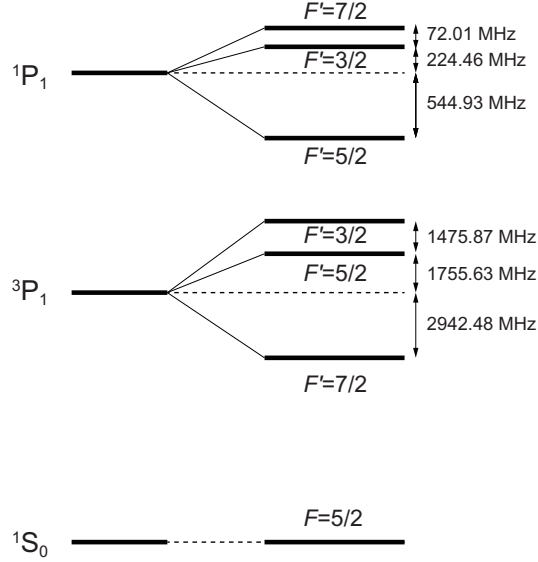


Figure 2.2: Hyperfine structure of the $^1S_0 \rightarrow ^1P_1$ and $^1S_0 \rightarrow ^3P_1$ transitions for ^{173}Yb .

are denoted by $^{2S+1}L_J$. Electronic levels of ytterbium typically used in ultracold experiment are shown in Figure 2.1. Two valence electrons can be arranged in spin singlet ($S = 0$) or spin triplet ($S = 1$) configuration. The lowest lying electronic state is 1S_0 , and excited states with $L = 1$ in spin singlet (triplet) configuration 1P_1 ($^3P_{0,1,2}$) are shown. Because laser field cannot change electronic spin directly, so electric dipole transition (E1) is only allowed to $^1S_0 \rightarrow ^1P_1$ transition. Other transitions are forbidden by selection rule. However, significant mixing between 1P_1 and 3P_1 states via spin-orbit interaction provides transition probability on $^1S_0 \rightarrow ^3P_1$, which is called intercombination line. In addition, hyperfine mixing between 3P_1 and $^3P_{0,2}$ also enables direct transitions of $^1S_0 \rightarrow ^3P_{0,2}$, which are referred as clock transitions. Among these transitions, dipole allowed $^1S_0 \rightarrow ^1P_1$ transition and intercombination line $^3S_0 \rightarrow ^1P_1$ are mainly harnessed for laser cooling of ytterbium atoms.

The natural linewidth of dipole allowed $^1S_0 \rightarrow ^1P_1$ transition ($\lambda = 398.9$ nm) is $\Gamma_{399}/2\pi = 29.1$ MHz. This transition is not completely closed because of decay channel from 1P_1 to metastable $^3P_{0,2}$. Atoms which are leaked to metastable $^3P_{0,2}$ states can be brought into cooling cycle again by optical repumping. The non-closed transition is an crucial issue for MOT, but it is not much significant for Zeeman slowing. Therefore, $^1S_0 \rightarrow ^1P_1$ transition is suitable for Zeeman slowing and imaging due to its strong photon scattering rate.

Intercombination line $^1S_0 \rightarrow ^3P_1$ ($\lambda = 555.8$ nm) is closed transition with narrow linewidth of $\Gamma_{556}/2\pi = 182.4$ kHz. Owing to the narrow linewidth, using intercombination line would be a double-edged sword for laser cooling: low Doppler cooling limit and low capture velocity. Atoms can be cooled down to few μK owing to the lower Doppler temperature $T_D = \hbar\Gamma_{556}/2k_B$, but low capture velocity restricts direct loading of hot atoms into MOT. Therefore, proper aid must be taken. In our laboratory, we adopted Zeeman slowing using $^1S_0 \rightarrow ^1P_1$ transition as a pre-cooling stage before MOT loading. Large photon scattering rate and capture velocity of $^1S_0 \rightarrow ^1P_1$ transition offer sufficient flux of cold atoms to MOT, which can allow efficient loading.

2.1.2 Laser system

For efficient laser cooling of ytterbium, both lasers with wavelengths of 398.9 nm and 555.8 nm are employed. Typical laser cooling experiment demands high power (several hundreds of mW) and narrow linewidth (narrower than linewidths of each transition). High-power lasers can be often produced by amplifying diode lasers via optical amplifiers such as tapered-amplifiers (TA) of doped fiber amplifiers. Unfortunately, standard high-power, narrow linewidth

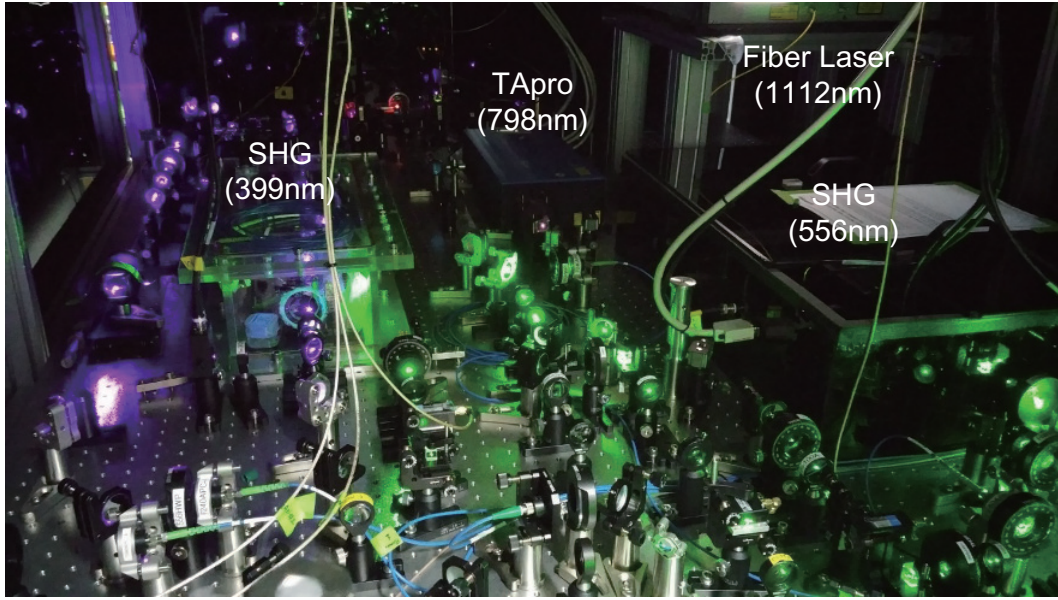


Figure 2.3: View of laser table for Yb machine in QGL. Bright violet and green light make spectacular scene.

lasers for ytterbium were not available, because optical amplifiers had not been much developed under the wavelength of 600 nm. In QGL, we opted second harmonic generation (SHG) of IR lasers to achieve proper laser lights for laser cooling experiment.

Blue laser

The fundamental laser with wavelength of 797.8 nm are generated by TA pro (*Toptica*) which consists of external cavity diode laser (ECDL) and TA. The gain chip TA-808-2000-1 had been used about 3 years and we barely managed required laser power, because its power had significantly degraded. We have replaced the old gain chip with new one TA-790-2000-1, which can provide plenty of laser power maximum 2.8 W. The elliptical beam after TA is shaped into circular beam with anamorphic prism pairs.

The blue light at 398.9 nm is generated by SHG of fundamental laser. When the light passes non-linear medium, frequency is doubled by second-order nonlinear effect inside the medium. Nonlinear effect in single-pass configuration is typically inefficient, but the efficiency can be largely enhanced with resonant cavity. Our SHG module is composed of lithium triborate (LBO, *Raicol Crystals*) crystal as a nonlinear medium and external bow-tie cavity for enhancement. For LBO, phase matching condition can be achieved by angle, type-1 critical phase matching (CPM), at the wavelength of 797.8 nm. In type-1 CPM condition, spatial walk-off angle make the frequency-doubled blue beam elliptical, so it is reshaped with cylindrical lens pair.

The length of cavity is stabilized by mirror mounted on a piezo-electric actuator via Hänsch-Couillaud method [71]. LBO crystal inside the cavity acts as a polarizing element, so reflectance of input beam depends on the polarization. Error signal is produced by substituting the intensity of reflected wave with different polarization. Therefore it can generate error signal without modulating the frequency of laser light. Then the cavity length is locked with fast PID (SIM960, *SRS*). At optimal condition, the conversion efficiency of SHG module is about 20%, where maximum power of blue light is about 500 mW. In typical, 250 mW of 398.9 nm light was enough for our experiment. After optimization of cavity, whole SHG module has been sealed with acryl box and filled with oxygen to prevent the degradation of LBO in humid environment. The temperature of the LBO crystal is stabilized at room temperature.

The frequency of the blue laser is locked to the atomic reference by using modulation transfer spectroscopy (MTS), where the frequency modulation of pump beam is transferred to the unmodulated probe beam by nonlinear interaction in atomic medium [72]. The pump-probe configuration of MTS allows

sub-Doppler spectroscopy, and its zero-crossing is accurately located at the center of atomic transition due to the characteristic background-free dispersive-like signal. In our scheme, small amount of the beam is detuned +418 MHz before spectroscopy by acousto-optic modulator (AOM). Pump beam is modulated by passing electro-optic modulator (EOM-02-25-U, *Photonics technologies*) with modulation frequency of 25 MHz. Hollow cathode lamp (L2738 Yb-Ne, *Hammatsu*) is used as atomic reference. Then modulated pump beam and unmodulated probe beam are aligned collinearly through the atomic reference. The transferred signal of probe beam is detected by photodiode, and frequency lock is achieved by feeding error signal to the locking electronics of TA pro (DigiLock 110, *Toptica*).

Absorption imaging

Our experiments are demonstrated by measuring the atomic density distribution via absorption imaging technique. We use vertical imaging path, where the objective lens ($5\times$ telecentric, *Mitutoyo*) is installed in front of the CCD camera (iXon ultra 888, *Andor technology*). The nominal numerical aperture and magnification of our objective are 0.13 and $5\times$ respectively. The resolution of imaging system is measured with USAF1951 test pattern, and we can achieve the resolution about $2.2\ \mu\text{m}$. The magnification of the imaging was calibrated by using Raman scattering on atomic gas, where departed momentum are precisely defined. Measured magnification is $6.5\times$, which is mainly affected by divergence of imaging beam in our system. Considering the pixel size of our CCD camera ($13\ \mu\text{m}$), each pixel corresponds to $2\ \mu\text{m}$ at the imaging plane.

In absorption imaging scheme, the atoms are illuminated with a resonant beam to dipole-allowed transition $|^1S_0, F = 5/2\rangle \rightarrow |^1P_1, F' = 7/2\rangle$, whose

intensity $\approx 0.02I_{\text{sat}}$ is much lower than the saturation intensity. In this low intensity limit, the intensity ratio of transmitted light $I(\mathbf{x})$ to incident light $I_0(\mathbf{x})$ through the atomic sample with density $n(\mathbf{r})$ follows the Beer-Lambert law,

$$I(\mathbf{x}) = I_0(\mathbf{x})e^{-\sigma \int n(\mathbf{r})dz}, \quad (2.1)$$

where \mathbf{x} is vectors in imaging plane, $\mathbf{r} = (\mathbf{x}, z)$, and $\sigma = 3\lambda^2/2\pi$ is resonant scattering cross section. Therefore, integrated atomic density per each pixel (column density) along the imaging beam axis is given by

$$n_{\text{col}}(\mathbf{x}) = \int n(\mathbf{r})dz = -\frac{1}{\sigma} \ln \frac{I(\mathbf{x})}{I_0(\mathbf{x})}. \quad (2.2)$$

In principle, two images that correspond to initial intensity of probe light and transmitted light is required to construct the atomic density. In experiment, three consecutive images are taken to reduce systematic error in imaging system: image of transmitted light through atomic sample $I(\mathbf{x})$, image of initial intensity of light without atoms $I_0(\mathbf{x})$, and background image without any light $I_B(\mathbf{x})$. Then atomic density can be constructed as

$$n_{\text{meas}}(\mathbf{x}) = -\frac{1}{\sigma} \ln \frac{I(\mathbf{x}) - I_B(\mathbf{x})}{I_0(\mathbf{x}) - I_B(\mathbf{x})}. \quad (2.3)$$

The number of atoms can be simply given by $N_{\text{meas}}(\mathbf{x}) = (A/M^2)n_{\text{meas}}(\mathbf{x})$, where A is area of each pixel in CCD camera, and M is magnification.

Typically the absorption imaging is used to measure momentum distribution of the atoms. The time-of-flight (TOF) absorption imaging is taken after the switching off the all potentials, and allowing atomic samples to evolve freely. When all trapping potentials are abruptly switched off, atoms can freely expand according to their initial momentum if interaction between atoms are negligible.

After sufficient expansion time, atomic distribution directly represents momentum distribution of atoms right before abrupt potential switching. After TOF, imaging beam is applied for 100 μ s per a shot. Then the absorption image is constructed with three consecutive images.

Green laser

The fundamental laser with wavelength of 1111.6 nm had been generated by commercial fiber laser (Orange one, *Menlo systems*). Its seed laser diode had been significantly degraded, so it was difficult to maintain the system. We have installed new fundamental laser from Quantel (EYLSA-L-1111.6-3-P-SN-W-CO v2.0), which is composed of seed laser (Koheras ADJUSTIK Y10, *NKT Photonics*) and ytterbium-doped fiber amplifier (CYFL-KILO-02-LP-1111.6-WT1-FM1-STO-OM1-B301-FA, *Keopsys*). The linewidth of laser is <20 kHz, which is narrower than the natural linewidth of the intercombination transition.

Similar to the blue laser, 555.8 nm laser light is generated by SHG of fundamental laser at 1111.6 nm. LBO crystal is used as a nonlinear medium, but phase matching condition is achieved with temperature, type-2 non-critical phase matching (NCPM), at the wavelength of 1111.6 nm. Although NCPM condition typically away from the room temperature, but it has advantage on insensitivity to the misalignment and the absence of spatial walk-off. Length of bow-tie cavity is again stabilized by Hänsch-Couillaud method, and its optimal conversion efficiency is about 20%.

The frequency of the green laser is stabilized by MTS. Small portion of the beam is detuned by -160 MHz before spectroscopy, and pump beam is modulated by EOM (EOM-02-3-U, *Photonics technologies*) with modulation frequency of 3 MHz. The small saturation intensity $I_{\text{sat}} = 0.14 \text{ mW/cm}^2$ of intercombination

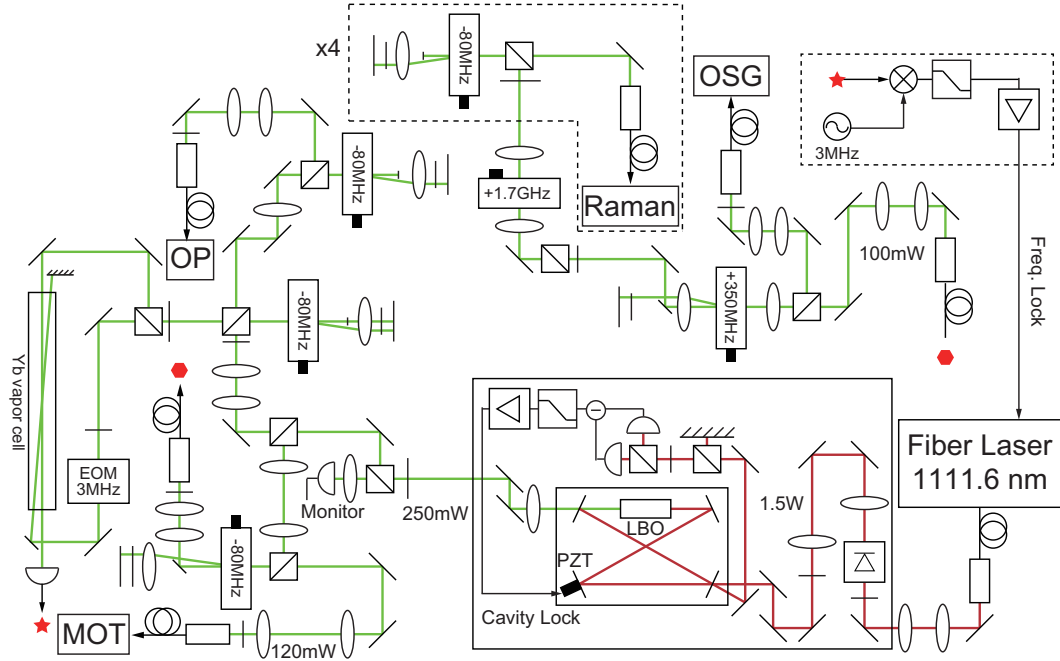


Figure 2.5: Schematic of the 555.8 nm green laser system. The fundamental laser produced by ytterbium-doped fiber laser at 1111.6 nm passes SHG bow-tie cavity for frequency doubling. Similar to the blue laser system, cavity length and frequency of seed laser are stabilized by Hänsch-Couillaud method and MTS respectively. We have used Yb vapor cell for atomic reference, because sufficient atomic flux had not been achieved by Yb HCL. Power of green lights are redistributed and frequency shifted for experiment.

line makes detection of spectroscopy signal difficult. To enhance the error signal, atomic cell with sufficient flux was built rather than using hollow cathode lamp. Also, photomultiplier tube (PMT H10492, *Hamamatsu*) was used for detecting modulation-transferred probe beam. Error signal is produced with homemade electronics, and frequency lock is achieved by delivering error signal directly into fundamental laser with PID (SIM960, *SRS*).

Optical dipole trap and optical lattice laser

High-power optical dipole trap (ODT) beams are produced by 100W ytterbium fiber laser with wavelength of 1070nm (YLR-100-1070-LP, *IPG photonics*). The IR laser had been controlled by AOM, but high power incident light (>30 W) has detrimental effect on AOM, results in beam shape deformation and beam pointing instability. Therefore, we have controlled laser power itself by computer with the aid of motorized rotating half wave plate. An overview of the IR laser setup is shown in Fig. 2.6. The polarization of laser is first purified, and reshaped with cylindrical lens pair. The beam power is monitored by two photodiodes with different gain, which regulate beam power in different range respectively. Laser power is manipulated and stabilized with single PID, so monitoring photodiode is switched by multiplexer (ADG5209, *Analog devices*) at the middle of experiment. Laser beam is then delivered to the chamber through the optical transport setup which is composed of movable lens and lens pair.

The source of auxiliary ODT and optical lattice is a single-frequency green fiber laser (GLR-20, *IPG photonics*), which is capable of producing 20 W output at 532 nm. The linewidth of laser is < 1 MHz, so it is sufficient to generate optical lattice. Laser output is divided and sent through AOMs for power control and stabilization. AOMs are driven with different rf frequency to

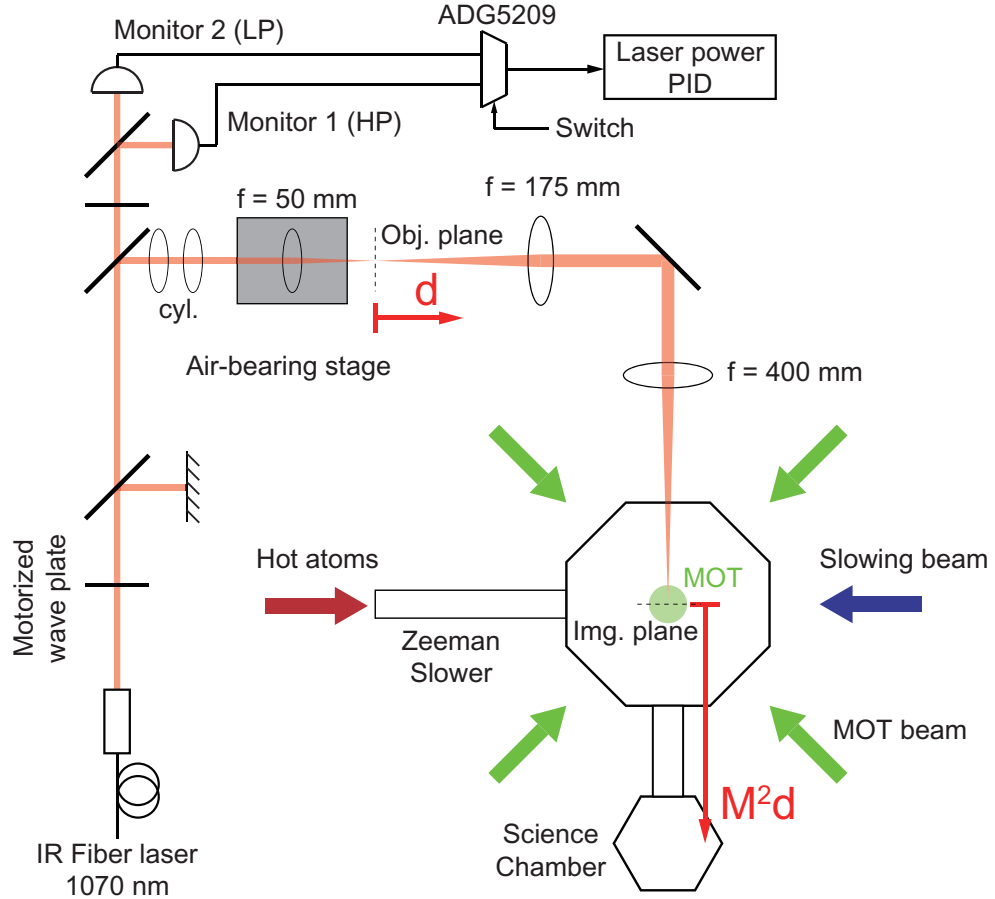


Figure 2.6: Schematic of the IR laser ODT and transport system. IR laser power is monitored by two photodiodes, which are switched by multiplexer. Power range of laser is coarsely tuned by motorized wave plate, and finely stabilized by PID servo. Then beam is injected to cylindrical lens pair to generate elliptical beam. Tight focus (object plane) generated by lens on air-bearing stage is projected to image plane via 4- f system with magnification of 2.3. When the focus is shifted by d in the object plane, focus in the imaging plane is shifted by M^2d .

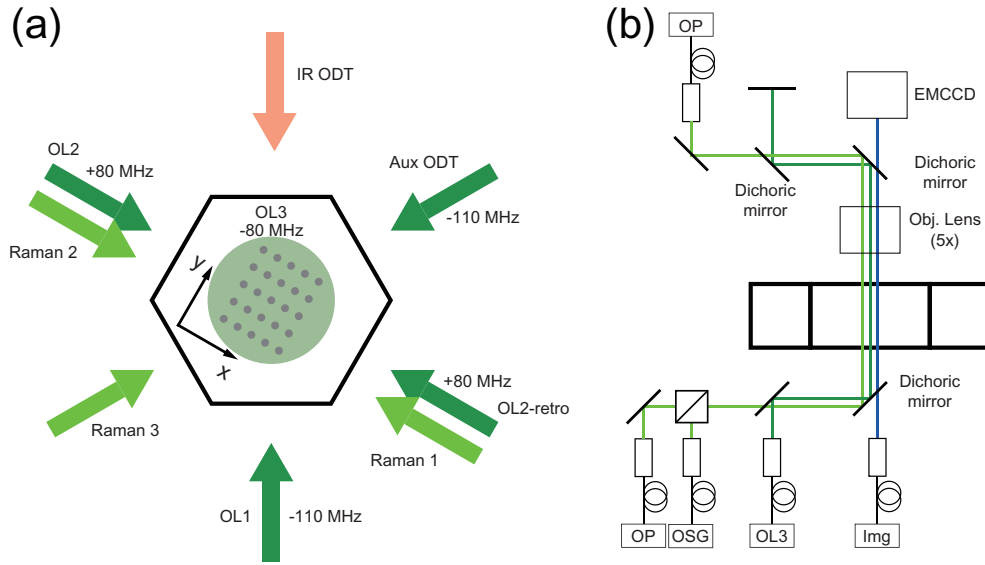


Figure 2.7: Schematic of the ODT and optical lattice setup at science chamber in (a) top view and (b) side view. Each laser line is denoted by its color. Shifted frequency is noted for auxiliary ODT and optical lattice at 532 nm. Because of shifted frequency, OL2 and OL3 are independent. Auxiliary ODT and OL1 beam are interfered to generate optical lattice in direction y . Optics for monitoring, polarization, focusing are omitted in these illustrations.

prevent interference between distinct beams. We note that two beams, which are labeled as auxiliary ODT and OL1 by its history, are diffracted by same rf source to create accordion type optical lattice. Laser beams are resized with spherical lens pair and coupled into single mode PM fibers, and then delivered to the atoms.

2.2 Producing degenerate Fermi gas

The cooling procedure of ytterbium atoms can be separated by two stages; at the main and the science chamber. Atoms are first cooled by Zeeman slowing and magneto-optical trap (MOT) at main chamber. After pre-cooling step at main chamber, atoms are transferred to the ODT, and then transported to the science chamber. Degeneracy is finally reached by evaporative cooling in crossed optical dipole trap at science chamber.

2.2.1 Cooling procedures

Zeeman slowing and magneto-optical trap (MOT)

The alkaline-earth atoms such as ytterbium generally have narrow intercombination line, which can achieve low Doppler temperature in MOT. However, atoms ejected from oven cannot be directly trapped in MOT, because the average velocity of the collimated atomic beam flux right after the nozzle exceeds the capture velocity of MOT. In our ytterbium machine, increasing field Zeeman slower is used to provide slow atoms, where red-detuned light from atomic transition is employed to compensate the Doppler shift. The slower beam is σ^- polarized 399 nm light, which corresponds to the $|^1S_0, F = 5/2, m_F = -5/2\rangle \rightarrow$

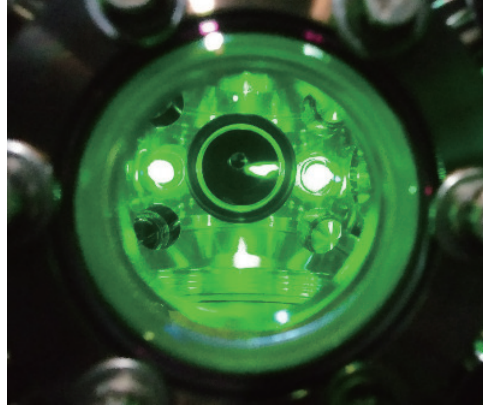


Figure 2.8: Photo of the fermionic ^{173}Yb magneto optical trap (MOT) during the loading at the main chamber.

$|^1P_1, F' = 7/2, m_{F'} = -7/2\rangle$ transition, and detuned by $\Delta = -1$ GHz. Successive resonant photon scattering efficiently slows down the atomic beam flux along the Zeeman slower, which can lower the average velocity of atoms under the capture velocity of MOT.

After deceleration by Zeeman slowing, atoms are further cooled and captured by 3D MOT. The MOT operates on the $|^1S_0, F = 5/2\rangle \rightarrow |^3P_1, F' = 7/2\rangle$ transition with narrow linewidth of $\Gamma = 182$ kHz. In 3D MOT, position dependent photon scattering occurs on atoms, trapping the atoms to the center. Detrimental effect from $|^1S_0, F = 5/2\rangle \rightarrow |^1P_1, F' = 5/2\rangle$ transition ($\Delta = -160\text{MHz}$) is reduced by introducing dark spot at the location of captured atoms in MOT. Phase space density is further increased by compressing the MOT at the final stage. After 15 s operation, about 10^8 atoms are collected with temperature about $20 \mu\text{K}$.

Transport and evaporative cooling

Atoms in compressed MOT are directly transferred to the optical dipole trap (ODT) by high-power, far red-detuned IR laser beam at 1070 nm. The trap depth of ODT $\approx 540\mu\text{K}$ is much higher than the temperature of MOT, and ODT beam has elliptical profile of $w_x : w_z = 3 : 1$ to make good spatial overlap with MOT, and compensate the effect of gravity. The atoms are transported to the science chamber to gain better optical access and imaging. In our setup, $4f$ system with magnification of $M \approx 2.3$ is employed to mechanically shift the focus of the ODT. As the first lens is moved by distance d from the initial position, the focus is shifted by M^2d with slight change of beam waist. About 34 cm travel within 1.6 s from main chamber to science chamber is in capability of our air-bearing stage (ABL1000-100, *Aerotech*). Smooth velocity profile of mechanical translation of lens was carefully chosen to minimize atom loss during the transport, resulting in transport efficiency about 85%.

The final stage of cooling is evaporative cooling in crossed dipole trap. The basic principle of evaporative cooling is to remove atoms with high kinetic energy and redistribute thermal energy between the remaining atoms, which increases the phase-space density. For efficient evaporation, density of atomic gas should be high enough to provide fast rethermalization between atoms via elastic collision. Therefore, focused green laser (532 nm), far red-detuned from 1P_1 transition, is aligned to intersect the focus of IR ODT, giving additional confinement on axial direction of IR ODT. The angle between two dipole trap is given by 60° due to the limited optical access of our science chamber. Compared to the single ODT configuration, increased density of atoms in crossed ODT makes evaporative cooling efficient. Although increase in density of atoms would suffer

inelastic three-body collision scales as $\propto n^2 a^2$, but our crossed ODT geometry, tight vertical confinement with loose transverse confinement, can avoid severe three-body loss by reducing atomic density in transverse direction.

Evaporative cooling starts by slowly decreasing the dipole trap potential. After 3.5 s of evaporative cooling step, we can get degenerate ytterbium Fermi gas. Typical trap frequencies at the final stage are determined by measuring harmonic oscillation of atomic cloud, which is estimated as $\{\omega_x, \omega_y, \omega_z\} \approx 2\pi \times \{30, 105, 146\}$ Hz.

Thermometry of degenerate Fermi gas

When the temperature of atoms are sufficiently cold, the thermal de Broglie wavelength is much larger than the distance between particles. In this regime, atoms can be described by wave function, and will obey quantum statistics. If atom follows Bose-Einstein statistics, bosonic atoms will be condensed into single state below the critical temperature. It is dramatic in momentum space, as the thermal bosons with wide Gaussian distribution disappears, while the condensed atoms appear at zero momentum with very narrow distribution.

In contrast to the Bose-Einstein condensate (BEC), where the sharp phase transition from thermal gas to condensate occurs, the onset of the degeneracy of fermions is subtle to be characterized. Following Pauli exclusion principle, same energy level cannot be filled with identical fermions. At zero temperature, the fermions fills every energy levels up to Fermi energy from the ground state. For homogeneous trap, it will show sharp momentum distribution. However, at finite temperature, higher energy levels are occupied by thermally excited fraction of fermions, and it is smoothly changed by temperature. Therefore, temperature should be carefully determined from the density distribution.

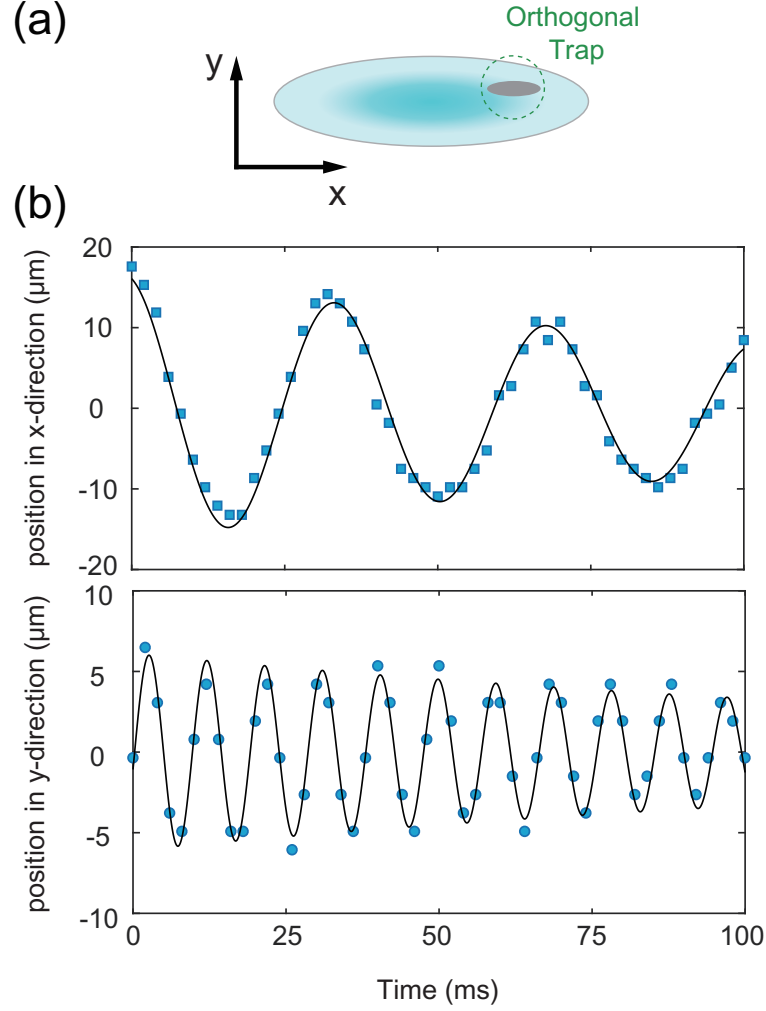


Figure 2.9: (a) Schematic of harmonic trap frequency measurement. Additional ODT in z direction is applied at the final stage of evaporative cooling to locate atomic clouds at off-center of harmonic trap. This additional ODT is then abruptly turned off, and position of atomic cloud is recorded after 15 ms time-of-flight (TOF), which magnifies the scale of movement. Because atoms deviated from the center of x, y direction, dipole mode in both directions are excited. (b) Temporal position of atomic cloud. Dipole oscillation frequency is determined by sinusoidal fitting, $\{\omega_x, \omega_y\} = 2\pi\{30, 105\}$ Hz. Trap frequency in z direction is approximately estimated from calculation of beam waists, beam power distribution and trap geometry.

In experiment, atoms are trapped in a 3D harmonic potential, which is described by the Hamiltonian

$$\hat{H} = \frac{\hat{\mathbf{p}}^2}{2m} + \frac{m}{2}(\omega_x^2 x^2 + \omega_y^2 y^2 + \omega_z^2 z^2), \quad (2.4)$$

where $\hat{\mathbf{p}} = (p_x, p_y, p_z)$ is momentum operator. The density of states is given by

$$g(\epsilon) = \frac{\epsilon^2}{2(\hbar\bar{\omega})^3}, \quad (2.5)$$

where ϵ is the energy of a particle, and $\bar{\omega} = (\omega_x \omega_y \omega_z)^{1/3}$ is geometric mean of the trap frequency. The Fermi-Dirac distribution is given by

$$f(\epsilon) = \frac{1}{e^{\beta(\epsilon-\mu)} + 1} = \frac{1}{e^{\beta\epsilon}/\xi + 1}, \quad (2.6)$$

where $\beta = 1/k_B T$, and $\xi = \exp(\beta\mu)$ is fugacity. The number of atoms in each spin state is then

$$N_\sigma = \int_0^\infty g(\epsilon) f(\epsilon) d\epsilon. \quad (2.7)$$

At $T = 0$, $f(\epsilon) = 1$ for energy under the Fermi energy $\epsilon < E_F$. Then Fermi temperature is

$$T_F = \frac{E_F}{k_B} = \frac{\hbar\omega}{k_B} (6N_\sigma)^{1/3}. \quad (2.8)$$

At finite temperature, the number of atoms in each spin is given by

$$N_\sigma = - \left(\frac{k_B T}{\hbar\omega} \right)^3 \text{Li}_3(-\xi), \quad (2.9)$$

where Li_n is n th order Polylog function. Combining two equations, T/T_F is related to the fugacity as

$$\text{Li}_3(-\xi) = - \frac{1}{6(T/T_F)^3}. \quad (2.10)$$

Then how can we obtain fugacity from the experiment? With Thomas-Fermi approximation, which assumes local density distribution proportional to the external potential, the number density in phase space is given by

$$f(r, p) = \frac{1}{(2\pi\hbar)^3} \frac{1}{e^{\beta\hat{H}(r,p)}/\xi + 1}. \quad (2.11)$$

Then the real space and momentum space distribution, integrated over p and r respectively, are

$$n(r) = -\left(\frac{mk_{\text{B}}T}{2\pi\hbar^2}\right)^{3/2} \text{Li}_{3/2}(-\xi e^{-\frac{V(r)}{k_{\text{B}}T}}), \quad (2.12)$$

$$\bar{n}(p) = -\frac{k_{\text{B}}T}{(2\pi\hbar^2m\omega^2)^{3/2}} \text{Li}_{3/2}(-\xi e^{\frac{p^2}{2mk_{\text{B}}T}}), \quad (2.13)$$

where $V(r) = \frac{m}{2}(\omega_x^2x^2 + \omega_y^2y^2 + \omega_z^2z^2)$.

In experiment, momentum distribution is measured by absorptive imaging method after TOF. Because 3D atomic density is projected on the 2D image, the measured optical density shows information about momentum distribution integrated over the z direction. The column density (optical density integrated over z) is then given by

$$OD(x, y) = OD_{\text{peak}} \frac{\text{Li}_2(e^{-\xi} e^{-\frac{x^2}{2\sigma_x^2} - \frac{y^2}{2\sigma_y^2}})}{\text{Li}_2(e^{-\xi})}, \quad (2.14)$$

where OD_{peak} is peak optical density and $\sigma_i^2 = \frac{k_{\text{B}}T}{m\omega_i^2}[1 + (\omega_i t)^2]$, and t is expansion time.

Typical absorption image of the ^{173}Yb Fermi gas after TOF is shown in Figure 2.10. After the long expansion time $\omega_i t \gg 1$ with collisionless expansion, the aspect ratio goes to unity regardless of the trap geometry. By fitting the TOF image with the equation (2.14), fugacity ξ can be determined. Then, T/T_{F} is obtained through the relation with fugacity. In our setup, $N \simeq 10^5$ atoms with temperature $T/T_{\text{F}} \simeq 0.15$ can be obtained after evaporative cooling.

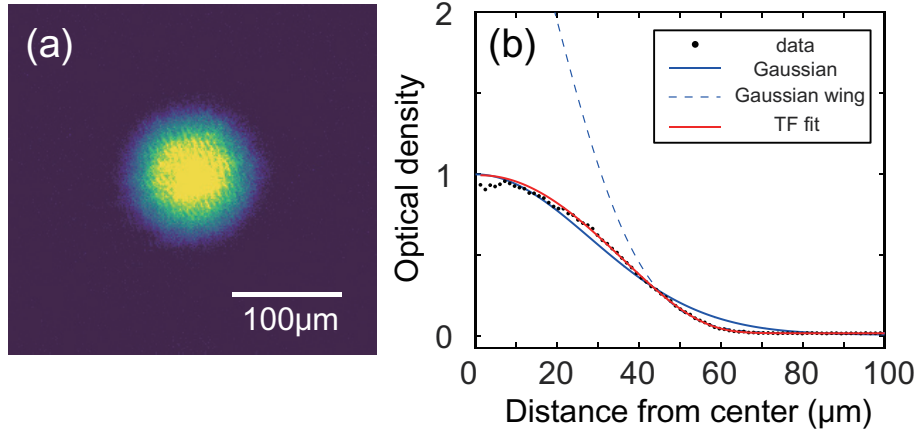


Figure 2.10: ^{173}Yb degenerate Fermi gas with six spin states. (a) Momentum distribution of fermi gas is detected with absorption imaging after 15 ms time of flight. (b) Averaged column density over azimuthal angle. Large deviation from the Gaussian distribution indicates the degenerate regime. From the Thomas-Fermi fit, the temperature is determined by $T/T_F \simeq 0.15$.

2.3 Manipulation of nuclear spin states

Optical Stern-Gerlach separation

Atoms in different spin states (or different magnetic spin number m_F) can be spatially separated by spin-dependent force induced by magnetic field gradient: the Stern-Gerlach effect. The technique can be well applied to separate spin states of alkali atoms, as they have sufficient state dependent magnetic moment of single electron. On the other hand, for alkaline-earth like atoms, the spin states of ground states 1S_0 cannot be separated practically due to lack of electronic angular momentum. As the nuclear magnetic moment is about three orders smaller than electron magnetic moment, required magnetic gradient for achieving sufficient separation is extremely large.

To overcome the limitation of applying enormous magnetic field gradient,

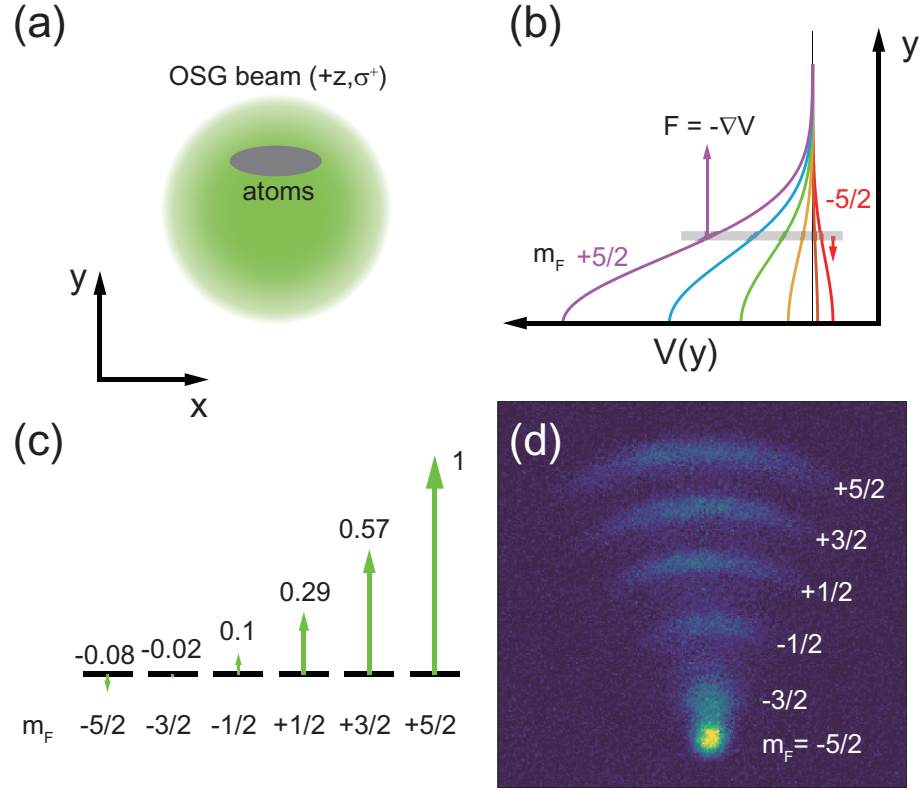


Figure 2.11: (a) Schematic of the optical Stern-Gerlach method. Blue-detuned σ^+ polarized light is aligned to the atomic gas, where the cloud center is placed at the intensity gradient of the Gaussian beam. (b) State-dependent force induced by beam intensity gradient. The grey strip indicates the relative position of the atomic cloud. (c) The ratio of resulting dipole force on different spin states, determined by detuning of light and polarization. (d) Typical absorption image taken after applying 4 ms OSG pulse followed by TOF expansion of 6 ms.

state dependent dipole force can be generated by optical means instead, which is referred to the optical Stern-Gerlach (OSG) effect [73, 74]. The transition strengths of $|^1S_0, F = 5/2\rangle \rightarrow |^3P_1, F' = 7/2\rangle$ vary with m_F and polarization of light. If the polarization of light is σ^\pm , every transition strengths are different to each other, resulting in m_F state dependent AC Stark shift. As a consequence, the m_F dependent force can be generated when optical intensity gradient is applied to the atoms.

In our experiment, a σ^+ polarized gaussian beam which is blue detuned by +860 MHz from $|^1S_0, F = 5/2\rangle \rightarrow |^3P_1, F' = 7/2\rangle$ transition line is used to provide state dependent force. During the OSG scheme, small magnetic field is applied to define quantization axis. OSG beam center is displaced from center of atomic cloud to induce state-dependent force. The main state-dependent repulsive force is produced by positively detuned $|^1S_0, F = 5/2\rangle \rightarrow |^3P_1, F' = 7/2\rangle$ transition, but attractive forces generated by negatively detuned hyperfine transitions $|^1S_0, F = 5/2\rangle \rightarrow |^3P_1, F' = 3/2, 5/2\rangle$ also participate. Including these contributions, $m_F = -5/2, -3/2$ are actually attractive to the OSG beam, while other states are pushed away.

In experimental sequence, atomic cloud is illuminated by OSG beam about 4 ms after all trapping potential is switched off, during the weak magnetic field is applied. Atoms start to fall by gravity, but state dependent force spatially separates m_F states in horizontal plane. After additional TOF time of 6 ms to enhance spatial separation, absorption image was taken. Due to the curvature of gaussian OSG beam, separated m_F states shows deformed distribution from initial atomic cloud. If one wants to keep information of initial atomic distribution, linear optical intensity gradient must be applied. For that purpose, such as digital micromirror devices (DMD) can be further employed to design

the OSG beam intensity profile.

Optical pumping

Since the intercombination transition is very narrow for Yb atoms, transition on individual m_F state can be selectively addressed under the sufficient magnetic field. In experiment, $|^1S_0, F = 5/2\rangle \rightarrow |^3P_1, F' = 7/2\rangle$ transition is employed. Sublevels of ground state $|^1S_0, F = 5/2\rangle$ shows small splitting under the external magnetic field, but $|^3P_1, F' = 7/2\rangle$ has sufficient Zeeman splitting $\Delta_Z/2\pi = 0.6\text{kHz/G} \times B$ under the magnetic field B . Therefore, each m_F state can be excited to $m'_F = m_F + \epsilon$ at specific polarization, where $\epsilon = \pm 1, 0$.

The ratio of spin states in mixture can be manipulated by optical pumping method based on spin-selective transition. As excited state spontaneously decays into ground states following selection rule, initial state can be pumped into other states after cycles of resonant excitation and spontaneous decay. In our experiment, optical pumping is implemented by applying σ^\pm polarized resonant light before the evaporative cooling sequence. Atoms can be kept inside the deep dipole trap, although subsequent momentum transfer from optical pumping heats the atoms. Using sequential optical pumping, various statistical spin mixture can be prepared. Collision rate is decreased for the mixture prepared with reduced number of spin states, because s -wave collision is only enabled between two different spin states. As a consequence, evaporative cooling is less efficient than six-component case, resulting in increased final temperature of the atomic gas.

If state selective transition is applied when the trap depth is lower than kinetic energy acquired from spontaneous decay, it selectively removes specific atomic states from the trap. This state selective removal can be used to prepare

spinless fermi gas, or to analyze each spin state after the experiment. The latter is useful for measuring information on momentum distribution of each spin state, because spin selective removal does not much distort the distribution than OSG scheme in our experiment. Although inelastic scattering can blur the overall momentum distribution, key features can be clearly distinguished by this technique.

2.4 Optical lattice

Loading atoms into the optical lattice

Optical lattice used in the experiments is generated by interference of 532 nm laser beams. Three dimensional cubic optical lattice is composed of two retro-reflected laser beams in \hat{x} , \hat{z} directions, and interfering two beams with angle of 120° in \hat{y} direction. Interference between each optical lattice axis were eliminated by separating the frequency of laser beams of each axis over tens of MHz using AOM. The atoms are usually loaded into the optical lattice by exponentially ramping to final lattice depth within 100 ms, while the ODT potential depth is decreased at the same time to loosen the trapping frequency. The adiabaticity of the lattice loading procedure can be characterized by measuring temperature of atoms, which are transferred back into the original ODT. We found there is negligible heating during the lattice loading, implying good adiabaticity.

Measurement of quasi-momentum distribution

In order to probe band structure of the optical lattice, useful observables are momentum distribution and population of atoms in each band. Both observables

can be measured by mapping quasi-momentum states of optical lattice into free particle momentum states, called band-mapping technique [75, 76]. When lattice potential is ramped down adiabatically, quasi-momentum of optical lattice q can be fully mapped into the free particle momentum state. Therefore, quasi-momentum distribution can be observed in TOF image after band mapping. However, for inhomogeneous system such as system including harmonic trap potential, Bloch states in different quasi-momentum states are not independent to each other. Therefore, ramp time must be shorter than the time scale of external potential. In our experiment, the lattice depth is linearly ramped down to zero within 0.5–1s, which is slow enough for band-mapping, but faster than the harmonic trap frequency.

Typical absorption image taken after band mapping followed by TOF is shown in Fig. 2.12. The population of atoms clearly shows the first Brillouin zone of 3D cubic lattice. Small population in higher bands implies that Fermi energy of initial atomic gas is below the recoil energy of optical lattice, and good adiabaticity of lattice loading and band mapping.

Calibration of the lattice depth

To calibrate the depth of the optical lattice potential, we typically use lattice modulation spectroscopy [77]. After adiabatic loading process, most of the atoms are in the lowest bands. When lattice depth is periodically modulated, atoms can be transferred to the higher band states. Following Fermi's golden rule, most of the atoms are transferred at the resonant condition, which is given by $E_n(q) - E_0(q) = h\nu$, where $E_n(q)$ is dispersion curve of n th band and ν is modulation frequency. Therefore, dispersion curve of optical lattice can be determined by measuring quasi-momentum and band index of excitations.

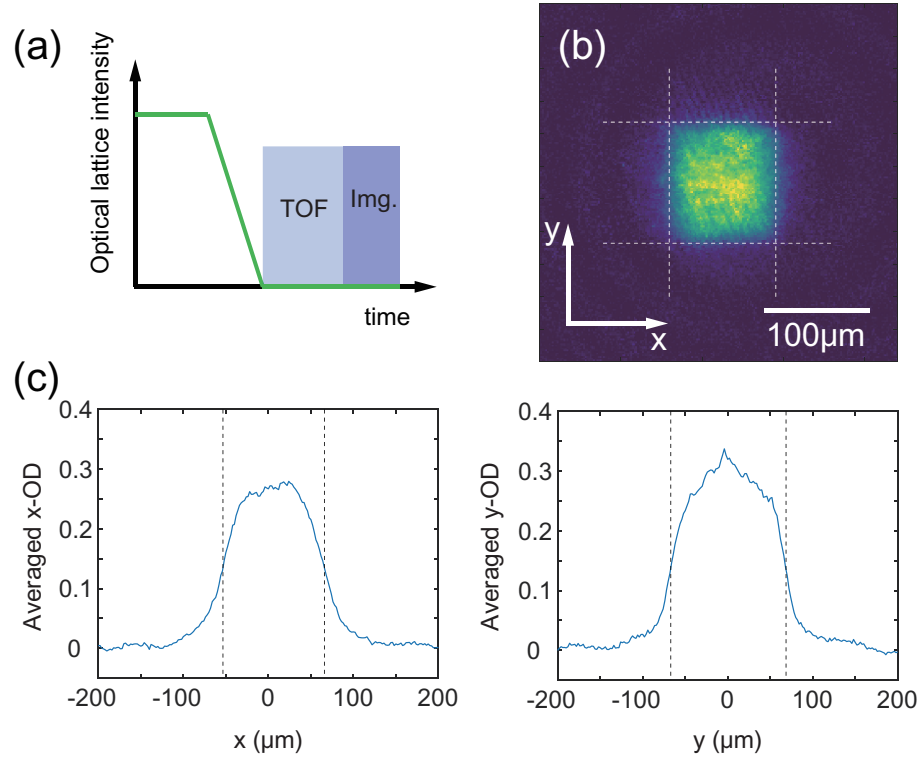


Figure 2.12: (a) Schematic sequence of band-mapping process. (b) Absorption image of band-mapped momentum distribution after 15 ms TOF. The depth of optical lattice in both direction was $V = 10E_r$. Dashed lines indicate first Brillouin zone. Because $k_x = \sqrt{3}\pi/\lambda$ and $k_y = 2\pi/\lambda$, length of Brillouin zone differs about 13%.

In experiment, modulation spectroscopy is applied after the optical lattice loading. Following short stabilization time of 10 ms, lattice depth is modulated for 2 ms with sinusoidal profile. Modulation amplitude is about 10% of optical lattice depth, and modulation frequency is varied over few tens of kHz. After lattice modulation, optical lattice potential is linearly ramped down to zero within 0.5 ms, followed by 15 ms TOF, to resolve quasimomentum and band states of excited atoms.

2.5 Two-photon Raman transition

When the matter is under the two optical fields, stimulated absorption and emission of photon can occur, leading momentum and energy transfer. In condensed matter, transferred momentum and energy typically excites specific vibrational modes. Similarly, stimulated two-photon Raman transition exerts momentum and energy to atoms. Figure 2.13 shows schematic view of two-photon transition. When atoms absorb photon with momentum \mathbf{k}_1 and emit photon with momentum \mathbf{k}_2 stimulated by optical field, atom acquires momentum $\mathbf{k}_1 - \mathbf{k}_2$ and energy $\hbar(\omega_1 - \omega_2)$. If dispersion of atom is given by free particle dispersion, the resonance condition is uniquely defined due to momentum and energy conservation. The two-photon transition can occur between momentum states, either with or without changing other states. In the view of atom optics, the situation is analogous to the Bragg diffraction, as matter wave is diffracted by optical lattice formed by two optical fields.

The stimulated two-photon Raman transition can be described by simple three states scheme. Suppose that an atom is illuminated by bichromatic optical

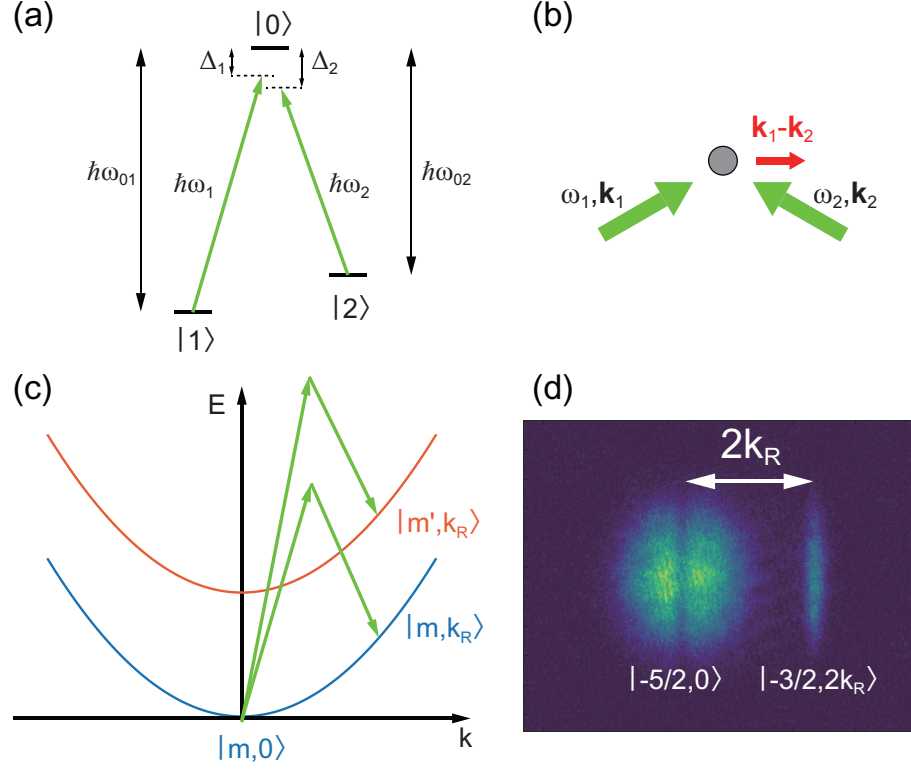


Figure 2.13: (a) Two states coupled by two optical fields, where $\Delta_i = \omega_i - \omega_{0i}$ is detuning of optical field to excited state. (b) Momentum transfer on atoms from the light field. (c) Stimulated Raman transition in atoms. Atomic states are described by spin state m and momentum q . Different spin states m, m' can be energetically shifted by Zeeman shift, and momentum states follow free-particle dispersion. When the energy and momentum conservation condition is satisfied, two states are coupled by stimulated two-photon Raman transition. When the spin state is preserved ($m \rightarrow m$), it is often called as *Bragg transition* because it is equivalent to the situation, where the atoms are scattered by moving optical lattice. (d) The absorption image of momentum distribution after Raman transition followed by 15 ms TOF. Atoms are initially prepared in $m = -5/2$ state by optical pumping. Only specific momentum class of atoms that satisfy resonant condition, $|-5/2, 0\rangle$, are transferred to the $|-3/2, 2k_R\rangle$.

fields with frequency ω_1 and ω_2 ,

$$\mathbf{E}(\mathbf{r}, t) = \hat{e}_1 E_1 \cos(\mathbf{k}_1 \cdot \mathbf{r} - \omega_1 t) + \hat{e}_2 E_2 \cos(\mathbf{k}_2 \cdot \mathbf{r} - \omega_2 t), \quad (2.15)$$

where \hat{e}_i is polarization vector of the field. For simple three-states configuration of atom, the atomic Hamiltonian can be described as

$$H_A = \frac{p^2}{2m} - \hbar\omega_{01}|1\rangle\langle 1| - \hbar\omega_{02}|2\rangle\langle 2|, \quad (2.16)$$

where the energy of excited state $|0\rangle$ is taken to be zero. In the rotating wave approximation and dipole approximation, the atom-field interaction Hamiltonian $H_{AF} = -\mathbf{d} \cdot \mathbf{E}$ is given by

$$H_{AF} = \sum_i \frac{\hbar\Omega_i}{2} (|i\rangle\langle 0| e^{i\mathbf{k}_i \cdot \mathbf{r}} + \text{H.c.}), \quad (2.17)$$

where $\Omega_i \equiv -\langle i|\hat{e}_i \cdot \mathbf{d}|0\rangle E_i/\hbar$ is Rabi frequency which describes coupling strength between $|i\rangle$ and $|0\rangle$ through optical field \mathbf{E}_i . The effective Hamiltonian of the system under the adiabatic elimination of excited states, assuming sufficient detuning to excited state, is given by

$$H_e = \frac{p^2}{2m} + \hbar \sum_i (\Delta_i + \xi_i) |i\rangle\langle i| + \frac{\hbar\Omega_R}{2} (|1\rangle\langle 2| e^{i(\mathbf{k}_2 - \mathbf{k}_1) \cdot \mathbf{r}} + \text{H.c.}), \quad (2.18)$$

where $\Delta_i = \omega_i - \omega_{0i}$ is detuning of optical field to excited state, and $\xi_i = \Omega_i^2/4\Delta$ is AC Stark shift with $\Delta = (\Delta_1 + \Delta_2)/2$. The Raman Rabi frequency $\Omega_R = \Omega_1\Omega_2/2\Delta$ describes coupling strength between two states $|1\rangle$ and $|2\rangle$ through two-photon Raman transition.

In real atomic system, the excited state is not given by a single state in general. To properly calculate the strength of Raman transition, every possible transitions must be counted. For example, considering $|^1S_0, F = 5/2\rangle \rightarrow |^3P_1, F'\rangle$ transition, there are three excited states $F' = 7/2, 5/2, 3/2$ due to

hyperfine splitting. Then, the Rabi frequency of Raman transition between $m_F \leftrightarrow m'_F$ using these excited states is given by

$$\begin{aligned}\Omega_R &= \sum_{F'} \frac{\Omega\Omega'}{2\Delta_{F'}} \\ &= \frac{3\pi c^2}{2\omega_0^3} 3\Gamma \left(\sum_{F'} \frac{C_{F',m_F}(e)C_{F',m'_F}(e')}{\Delta_{F'}} \right) \sqrt{I_e I_{e'}},\end{aligned}\quad (2.19)$$

where ω_0 is frequency of light and Γ is natural linewidth. $C_{F',m_F}(e)$ is Clebsch-Gordan coefficient for $m_F \rightarrow m'_F = m_F + e$ transition with polarization e . The expression can be expressed in terms of one excited state by noting the symmetry of the electron wave function [78], which leads to $\Omega_R \sim \Delta_{\text{HFS}}/\Delta_{F'}^2$ for specific F' , where Δ_{HFS} is hyperfine splitting [79]. The useful parameter for experiment is ratio of Raman transition strength to inelastic scattering rate Ω_R/Γ_{in} , and it scales as $\sim \Delta_{\text{HFS}}/\Gamma$ [78].

In our setup, laser blue-detuned by 1.97 GHz from $|^1S_0, F = 5/2\rangle \rightarrow |^3P_1, F' = 7/2\rangle$ transition is employed to induce Raman transition. The laser light detuned by 1.81 GHz is divided, and pass another 80 MHz AOM in double pass scheme respectively. Each Raman beam is delivered by an optical fiber and focused into the atomic cloud with beam diameter of $\approx 300 \mu\text{m}$. It is sufficiently larger than the trapped sample $\approx 30 \mu\text{m}$, which can reduce inhomogeneity of beam intensity over the whole sample.

2.6 Periodic shaking of optical lattice

The position of optical lattice can be manipulated by two approaches.

Frequency modulation

Frequency difference $\Delta\nu$ between two optical lattice beams leads moving optical lattice with velocity $v = a_L \Delta\nu$, where a_L is lattice spacing. If frequency difference has time-dependence, inertial force $F = -ma = -ma_L \Delta\dot{\nu}(t)$ is exerted on the atoms in co-moving frame. In our setup, the position of optical lattice is periodically driven by modulating the frequency of one of optical lattice beams. By controlling the RF of AOM, frequency of the 1st order beam can be modulated by $\nu_L + \Delta\nu(t)$, where ν_L is frequency of 0th order beam, while the other lattice beam is maintained at frequency ν_L .

Mechanical modulation

Optical lattice can be spatially modulated by mechanically shifting the optical path length. For retro-reflected configuration of optical lattice, it can be easily achieved by shifting the position of the mirror. In our experiment, position of mirror is precisely controlled by high bandwidth piezo chip. The piezo driven mirror is composed of three piezo chips (PA4CE, *Thorlabs*), low mass mirror (BB03-E02, *Thorlabs*), and a base plate for commercial optomechanical mirror mount. The nominal free stroke of piezo chip is $2.0 \mu\text{m}$, which can cover shift about 7 lattice sites. A low capacitance of piezo chip (22 nF) is suitable for the high frequency modulation up to few hundreds of kHz. Piezo chips are glued to the brass base plate with epoxy in tripod configuration to cover the area of mirror. The alumina end plates (PKCEP4, *Thorlabs*) are glued in between the base plate and piezo chips to provide insulation. Then low mass mirror (≈ 0.17 g) is glued above the piezo tripod. By using low mass of mirror relative to base plate, resonant frequency of the system would be formed at higher values,

providing sufficient bandwidth.

The piezo mirror was driven by high voltage driver (PX200, *PiezoDrive*) that covers frequency up to 100 kHz, which is externally controlled by arbitrary function generator (AFG1022, *Tektronics*). Frequency response of the piezo-driven mirror is measured with Michelson interferometer. Collimated laser beam ($\lambda = 532$ nm) consists interferometer, whose optical path length of one arm is modulated by piezo chip, and the intensity of interfered signal is monitored by photodiode.

In measurement, mirror position was modulated with sinusoidal function. In the limit of small modulation length $\Delta x \ll \lambda/2$ at the middle of interference maximum and minimum, intensity of interference signal linearly depends on the path length difference of interferometer. Figure 2.14 shows intensity and phase of interference signal. The observed intensity shows flat response, and the phase is linearly decreasing up to 80 kHz. The resonance position seems around 100 kHz as phase is clearly deviated from the linear fit. Linear slope of interference phase corresponds to constant time delay, and we found that piezo mirror has 2.4 μs delay after trigger signal. It can be easily compensated by tuning the trigger timing.

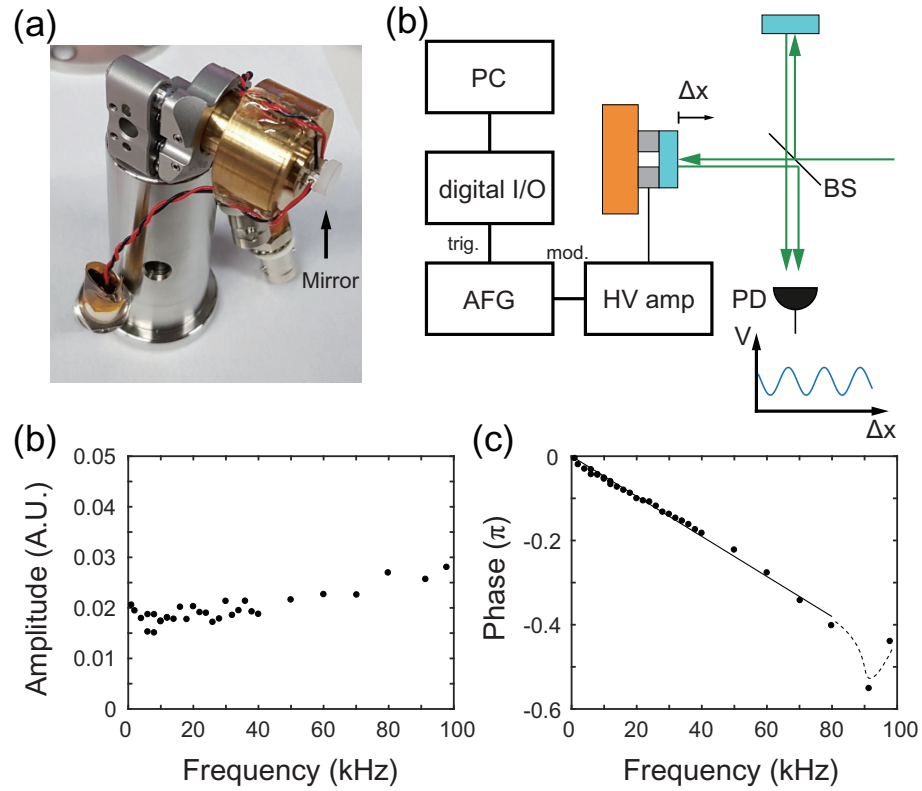


Figure 2.14: Piezo mirror system. (a) Picture of piezo mirror. Mirror is glued onto three piezo actuators with epoxy. (b) Schematics of piezo mirror and Michelson interferometry. (c) Amplitude and (d) phase of interferometry signal with the sinusoidal driving of piezo mirror.

Chapter 3

Floquet theory and stroboscopic dynamics

The dynamics of the system governed by time-dependent Hamiltonian is generally difficult to predict, because instantaneous eigenstates and eigenvalues are changing at every time step. However, if the perturbation is periodic in time, the situation can be simplified. Long time dynamics of the system can be effectively described by time-independent Hamiltonian, which is derived by the Floquet theorem. A well known example of Floquet system is Kapitza pendulum, where the pivot point of pendulum is periodically modulated in the direction of gravity. As the frequency increases, pendulum can oscillate upside down as if gravity acts in opposite direction. Thus, periodically driven system can show unique dynamics compared to the static system. In this regard, the concept of *Floquet engineering* has gained interests in recent years. This section describes basic Floquet theory, and perturbative expansion methods which approximate the effective Hamiltonian.

3.1 Floquet formalism

We consider a time-dependent periodic Hamiltonian with period of T ,

$$\hat{H}(t) = \hat{H}(t + T). \quad (3.1)$$

The eigenstates of the Hamiltonian are solutions of time-dependent Schrödinger equation

$$i\hbar \frac{\partial}{\partial t} |\psi(t)\rangle = \hat{H}(t) |\psi(t)\rangle \quad (3.2)$$

According to Floquet theory, the eigenstates $|\psi(t)\rangle$ called Floquet states can be written in

$$|\psi_n(t)\rangle = \exp(-i\epsilon_n t/\hbar) |u_n(t)\rangle, \quad (3.3)$$

where $|u_n(t)\rangle = |u_n(t + T)\rangle$ is Floquet mode, and ϵ_n is quasienergy [80].

Due to the periodicity of Floquet mode, the Floquet states are also eigenstates of time-evolution operator over one period,

$$\hat{U}(t_0 + T, t_0) |\psi_n(t_0)\rangle = \exp(-i\epsilon_n T/\hbar) |\psi_n(t_0)\rangle, \quad (3.4)$$

where $\hat{U}(t, t_0)$ is time evolution operator from t_0 to t , which is generally given by

$$\hat{U}(t, t_0) = \mathcal{T} \exp \left[-\frac{i}{\hbar} \int_{t_0}^t \hat{H}(\tau) d\tau \right]. \quad (3.5)$$

Here \mathcal{T} is time-ordering operator. From the relation, quasienergy spectrum can be obtained by diagonalizing $\hat{U}(t_0 + T, t_0)$, and it does not depend on the choice of arbitrary time t_0 .

The stroboscopic dynamics of each time frame $t = t_0 + nT$ can be described *stroboscopic Floquet Hamiltonian* [81], which is given by

$$\hat{H}_F^{t_0} = i\frac{\hbar}{T} \log[\hat{U}(t_0 + T, t_0)]. \quad (3.6)$$

The stroboscopic Floquet Hamiltonian depends on the choice of initial time t_0 , while it does not change the quasienergy spectrum. Therefore, Floquet Hamiltonians in other time frame are related by gauge transformation. From the relation of time evolution operator,

$$\begin{aligned}\hat{U}(t'_0 + T, t'_0) &= \hat{U}(t'_0 + T, t_0 + T)\hat{U}(t_0 + T, t_0)\hat{U}(t_0, t'_0) \\ &= \hat{U}(t_0, t'_0)^\dagger \hat{U}(t_0 + T, t_0)\hat{U}(t_0, t'_0),\end{aligned}\quad (3.7)$$

we can derive unitary transformation between Floquet Hamiltonian in different time frame,

$$\hat{H}_F^{t'_0} = \hat{U}(t_0, t'_0)^\dagger H_F^{t_0} \hat{U}(t_0, t'_0). \quad (3.8)$$

Time evolution operator for arbitrary times can be written as

$$\begin{aligned}\hat{U}(t_2, t_1) &= \hat{U}(t_2, t_0 + nT) \exp[-i\hat{H}_F^{t_0} nT] \hat{U}(t_0, t_1) \\ &= \exp[i\hat{K}_F^{t_0}(t_2)] \exp[-i\hat{H}_F^{t_0}(t_2 - t_1)] \exp[i\hat{K}_F^{t_0}(t_1)],\end{aligned}\quad (3.9)$$

where $\exp[i\hat{K}_F^{t_0}(t)] \equiv \hat{U}(t, t_0) \exp[i\hat{H}_F^{t_0}(t - t_0)]$, and $\hat{K}_F^{t_0}(t)$ is *stroboscopic micromotion operator*. This description depends on the initial time t_0 , but one can find more general description under the proper gauge transformation.

There exists Hermitian operator such that

$$\hat{H}_{\text{eff}} = e^{i\hat{K}(t_0)} H_F^{t_0} e^{-i\hat{K}(t_0)}, \quad (3.10)$$

where $\hat{K}(t_0)$ is referred as *kick operator* which is periodic in time, $\hat{K}(t_0 + nT) = \hat{K}(t_0)$, and \hat{H}_{eff} is *effective Hamiltonian*. The time-independed effective Hamiltonian can be found by transforming the time-dependent Hamiltonian with unitary gauge transformation. Assuming

$$|\phi(t)\rangle = \hat{\mathcal{U}}(t)|\psi(t)\rangle = e^{i\hat{K}(t)}|\psi(t)\rangle, \quad (3.11)$$

then by plugging the equation to the time-dependent Schrödinger equation,

$$i\hbar \frac{\partial}{\partial t} |\phi(t)\rangle = \hat{G} |\phi(t)\rangle, \quad (3.12)$$

where

$$\hat{G} = e^{i\hat{K}(t)} \hat{H}(t) e^{-i\hat{K}(t)} + i\hbar \frac{\partial e^{i\hat{K}(t)}}{\partial t} e^{-i\hat{K}(t)}. \quad (3.13)$$

One can assume that unitary transformation $e^{i\hat{K}(t)}$ maps $\hat{H}(t)$ into time-independent Hamiltonian $\hat{G} \equiv \hat{H}_{\text{eff}}$. Then the time evolution operator can be written as [82]

$$\hat{U}(t_2, t_1) = e^{-i\hat{K}(t_2)} e^{-\frac{i}{\hbar} \hat{H}_{\text{eff}}(t_2 - t_1)} e^{i\hat{K}(t_1)}. \quad (3.14)$$

In this form of expression, the Floquet gauge dependence is all carried by the kick operator, so effective Hamiltonian is independent of initial time. The time evolution is composed of time-dependent micromotion at initial/final step and evolution by time-independent effective Hamiltonian \hat{H}_{eff} . Also, we can find relation between stroboscopic micromotion operator and kick operator, such that

$$e^{-i\hat{K}_F^{t_0}(t)} = e^{-i\hat{K}(t)} e^{-i\hat{K}(t_0)}. \quad (3.15)$$

3.2 Perturbative inverse frequency expansion

Floquet Hamiltonian can be directly computed from the intergration of time-dependent Hamiltonian, but the simple form of time-independent Hamiltonian is difficult to be derived from this equation. Rather than integration of time-dependent operators, Floquet Hamiltonian can be perturbatively expanded when the driving frequency is much larger than the energy scale of the system. In this section, we present two useful expansion methods.

Magnus expansion

Magnus expansion is useful approach to compute the stroboscopic Floquet Hamiltonian. In the high frequency limit, where the driving frequency is higher than any energy scale in the system, the stroboscopic Floquet Hamiltonian and micromotion operator can be expanded in a perturbative series as [83]

$$\hat{H}_F^{t_0} = \sum_{n=0}^{\infty} \hat{H}_F^{t_0(n)}, \hat{K}_F^{t_0}(t) = \sum_{n=0}^{\infty} \hat{K}_F^{t_0(n)}(t). \quad (3.16)$$

The terms of expansion can be obtained by

$$\begin{aligned} \hat{H}_F^{t_0} &= \frac{i}{T} \log \left\{ \mathcal{T} \exp \left[-\frac{i}{\hbar} \int_{t_0}^t \hat{H}(\tau) d\tau \right] \right\}, \\ \hat{K}_F^{t_0}(t) &= i \log \left\{ \mathcal{T} \exp \left[-\frac{i}{\hbar} \int_{t_0}^t \hat{H}(\tau) d\tau \right] e^{i\hat{H}_F^{t_0}(t-t_0)} \right\}. \end{aligned} \quad (3.17)$$

Then leading terms are given by Magnus expansion [84],

$$\begin{aligned} \hat{H}_F^{t_0(0)} &= \frac{1}{T} \int_{t_0}^{t_0+T} d\tau \hat{H}(\tau) = \hat{H}_0, \\ \hat{H}_F^{t_0(1)} &= \frac{1}{2!T i \hbar} \int_{t_0}^{t_0+T} d\tau_1 \int_{\tau_1}^{t_0} d\tau_2 [\hat{H}(\tau_1), \hat{H}(\tau_2)] \\ &= \frac{1}{\hbar \omega} \sum_{m=1} \frac{1}{m} \left([\hat{H}_m, \hat{H}_{-m}] - e^{im\omega t_0} [\hat{H}_m, \hat{H}_0] + e^{-im\omega t_0} [\hat{H}_{-m}, \hat{H}_0] \right), \\ \hat{H}_F^{t_0(2)} &= \frac{1}{3!T (i\hbar)^2} \int_{t_0}^{t_0+T} d\tau_1 \int_{\tau_1}^{t_0} d\tau_2 \int_{\tau_2}^{t_0} d\tau_3 ([\hat{H}(\tau_1), [\hat{H}(\tau_2), \hat{H}(\tau_3)]] + [\hat{H}(\tau_3), [\hat{H}(\tau_2), \hat{H}(\tau_1)]]), \end{aligned} \quad (3.18)$$

$$\hat{K}_F^{t_0(0)}(t) = 0,$$

$$\begin{aligned} \hat{K}_F^{t_0(1)}(t) &= \frac{1}{\hbar} \int_{t_0}^t d\tau (\hat{H}(\tau) - \hat{H}_F^{t_0(1)}) \\ &= -\frac{1}{2\hbar} \left[\int_{t_0+T}^t d\tau \hat{H}(\tau) \left(1 + 2\frac{t-\tau}{T} \right) - \int_{t_0+T}^{t_0} d\tau \hat{H}(\tau) \left(1 + 2\frac{t_0-\tau}{T} \right) \right] \\ &= \frac{1}{i\hbar\omega} \sum_{m \neq 0} \hat{H}_m \frac{e^{im\omega t} - e^{im\omega t_0}}{m}, \end{aligned} \quad (3.19)$$

where we have expanded time-dependent Hamiltonian in Fourier series as

$$\hat{H}(t) = \sum_m \hat{H}_m e^{im\omega t}. \quad (3.20)$$

The zeroth order term of the Floquet Hamiltonian is the time-averaged Hamiltonian, and the zeroth-order micromotion operator is zero, so both terms are Floquet gauge invariant: no dependence on initial time t_0 . Floquet gauge dependence exists on the correction terms of both stroboscopic Floquet Hamiltonian and micromotion operator, and these vanish in the high frequency limit $\omega \rightarrow \infty$.

High frequency expansion

By changing basis, time-evolution can be described by Floquet gauge independent effective Hamiltonian \hat{H}_{eff} and kick operator $\hat{K}(t)$. In this description, kick operator all carries the Floquet gauge dependence. In the high-frequency limit, \hat{H}_{eff} and $\hat{K}(t)$ can be perturbatively expanded [79, 82, 85],

$$\hat{H}_{\text{eff}} = \sum_{n=0}^{\infty} \hat{H}_{\text{eff}}^{(n)}, \quad \hat{K}(t) = \sum_{n=0}^{\infty} \hat{K}^{(n)}(t). \quad (3.21)$$

Following operator expansion,

$$e^{i\hat{K}(t)} \hat{H} e^{-i\hat{K}(t)} = \hat{H} + i[\hat{K}, \hat{H}] - \frac{1}{2!}[\hat{K}, [\hat{K}, \hat{H}]] - \frac{1}{3!}[\hat{K}, [\hat{K}, [\hat{K}, \hat{H}]]] + \dots, \quad (3.22)$$

$$\frac{\partial e^{i\hat{K}(t)}}{\partial t} e^{-i\hat{K}(t)} = i \frac{\partial \hat{K}}{\partial t} - \frac{1}{2!} \left[\hat{K}, \frac{\partial \hat{K}}{\partial t} \right] - \frac{i}{3!} \left[\hat{K}(t), \left[\hat{K}, \frac{\partial \hat{K}}{\partial t} \right] \right] + \dots, \quad (3.23)$$

effective Hamiltonian \hat{H}_{eff} and the kick operator $\hat{K}(t)$ can be approximately obtained. With Fourier expansion of time-dependent Hamiltonian, the effective

Hamiltonian and kick operator are given by

$$\begin{aligned}
\hat{H}_{\text{eff}}^{(0)} &= \hat{H}_0, \\
\hat{H}_{\text{eff}}^{(1)} &= \sum_{m \neq 0} \frac{[\hat{H}_m, \hat{H}_{-m}]}{m\hbar\omega}, \\
\hat{H}_{\text{eff}}^{(2)} &= \sum_{m \neq 0} \left[\frac{[\hat{H}_{-m}[\hat{H}_0, \hat{H}_m]]}{2(m\hbar\omega)^2} + \sum_{m' \neq 0, m} \frac{[\hat{H}_{-m'}[\hat{H}_{m'-m}, \hat{H}_m]]}{3mm'(\hbar\omega)^2} \right], \tag{3.24}
\end{aligned}$$

$$\begin{aligned}
\hat{K}^{(0)}(t) &= 0, \\
\hat{K}^{(1)}(t) &= \sum_{m \neq 0} \frac{e^{im\omega t}}{im\hbar\omega} \hat{H}_m, \\
\hat{K}^{(2)}(t) &= \sum_{m \neq 0} \left[\frac{e^{im\omega t}[\hat{H}_0, \hat{H}_m]}{(m\hbar\omega)^2} + \frac{1}{2} \sum_{m' \neq 0, m} \frac{e^{i(m-m')\omega t}[\hat{H}_{-m'}, \hat{H}_m]}{m(m-m')(\hbar\omega)^2} \right]. \tag{3.25}
\end{aligned}$$

The zeroth order term is simply the time-average of Hamiltonian, and higher order terms is composed of combinations of different harmonic terms, which do not commute with each other. For example, the first order term in effective Hamiltonian describes the effect driven by combination of opposite harmonic terms, resulting in time-independence.

Two-level system

We consider two-level system with energy gap Δ driven by time-dependent coupling. We choose simple sinusoidal modulation $V(t) = A \cos(\omega t)$. The time-dependent Hamiltonian is given by

$$\hat{H}(t) = \frac{\Delta}{2} \sigma_z + V(t) \sigma_x, \tag{3.26}$$

where $\{\sigma_x, \sigma_y, \sigma_z\}$ are the 2×2 Pauli matrices. Under the rotating frame $\hat{R}(t) = \exp(-i\omega t \sigma_z/2)$,

$$\begin{aligned}\hat{H}'(t) &= \hat{R}^\dagger(t) \hat{H}(t) \hat{R}(t) - i\hbar \hat{R}^\dagger(t) \frac{\partial \hat{R}(t)}{\partial t} \\ &= \frac{1}{2}(\Delta - \hbar\omega)\sigma_z + \frac{A}{2}(1 + e^{2i\omega t \sigma_z})\sigma_x.\end{aligned}\quad (3.27)$$

Then we consider resonant driving case $\hbar\omega = \Delta$.

Using Magnus expansion method, the stroboscopic Floquet Hamiltonian up to first order is given by

$$\hat{H}_F^{t_0} = \frac{A}{2}\sigma_x + \frac{1}{2\hbar\omega} \left(\frac{A}{2}\right)^2 [1 - 2\cos(2\omega t_0)]\sigma_z + O(1/\omega^2) \quad (3.28)$$

The leading terms of the stroboscopic micromotion are given by

$$\hat{K}_F^{t_0}(t) = \frac{A}{4\hbar\omega} [(\sin 2\omega t - \sin 2\omega t_0)\sigma_x + (\cos 2\omega t - \cos 2\omega t_0)\sigma_y] + O(1/\omega^2) \quad (3.29)$$

Using high-frequency expansion method, the effective Hamiltonian up to first order is given by

$$\hat{H}_{\text{eff}} = \hat{H}_0 = \frac{A}{2}\sigma_x + \frac{1}{2\hbar\omega} \left(\frac{A}{2}\right)^2 \sigma_z + O(1/\omega^2) \quad (3.30)$$

The leading terms of the kick operator are given by

$$\hat{K}(t) = \frac{A}{4\hbar\omega} [\sigma_x \sin 2\omega t + \sigma_y \cos 2\omega t] + O(1/\omega^2) \quad (3.31)$$

Both expansion methods agree with each other, but show distinctive features. Stroboscopic Hamiltonian approximated from Magnus expansion contains Floquet gauge dependent term, while the effective Hamiltonian approximated from high-frequency expansion does not have any Floquet gauge dependence. In the latter case, Floquet gauge dependence is migrated to the kick operator

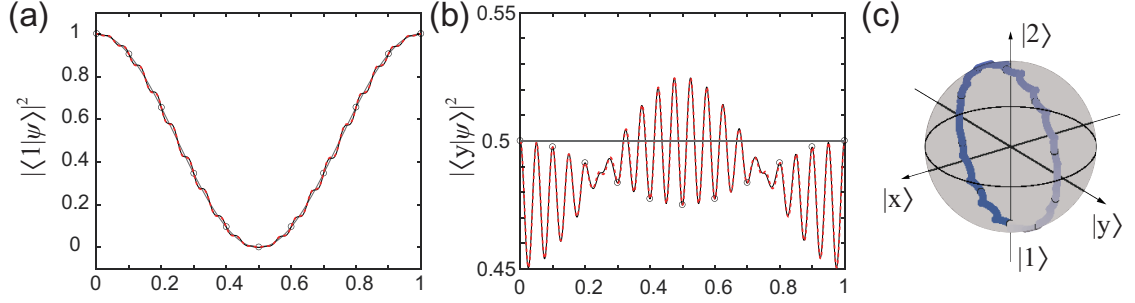


Figure 3.1: Dynamics of two-level system under the resonant modulation. The state is initially prepared in the $|1\rangle = (0, 1)^T$ state, and driven by driving frequency $\omega = 2\pi \times 10 = \Delta/\hbar$ and amplitude $A = 1$. (a) Dynamics of the driven two-level system projected on $|1\rangle$ and (b) projected on $|y\rangle = (1, i)^T/\sqrt{2}$. The exact dynamics by solving time-dependent Schrödinger equation is given by black line. Blue line indicates the dynamics in the limit of $\omega \rightarrow \infty$. The stroboscopic dynamics and non-stroboscopic dynamics calculated from Magnus expansion (hollow circles) and high-frequency expansion (red dashed line) well agree with exact dynamics. (c) Bloch sphere representation of the dynamics.

$\hat{K}(t)$. If we are interested in stroboscopic dynamics, we can either use $\hat{H}_F^{t_0}$ or \hat{H}_{eff} with $\hat{K}(t)$. If one is interested in stroboscopic dynamics, Magnus expansion would be preferable option, because it does not need to compute micromotion operator $K_F^{t_0}$. In contrast, high-frequency expansion has advantage on studying non-stroboscopic dynamics and Floquet quasienergy, because \hat{H}_{eff} is free from the Floquet gauge.

Let us compare exact dynamics governed by time-dependent Hamiltonian in rotating frame. The dynamics can be described by time-averaged Hamiltonian \hat{H}_0 and micromotion vanishes in the high-frequency limit $\omega \rightarrow \infty$. When the dynamics starts with initial state $|1\rangle = (0, 1)^T$, states will oscillate between $|1\rangle$ and $|2\rangle = (1, 0)^T$ with frequency of A/\hbar . However, for finite driving frequency, dynamics deviates from the \hat{H}_0 and shows micromotion at the frequency of the

driving. The Bloch-sphere representation can give further insight. While the states are slowly driven from $|1\rangle$ to $|2\rangle$, additional oscillation at the driving frequency also appears. Both the stroboscopic dynamics obtained from Magnus expansion, and non-stroboscopic dynamics calculated by high-frequency expansion well agree with the exact dynamics.

3.3 Driven optical lattices

In this thesis, we investigate the periodically modulated optical lattice. Periodic modulation can be achieved by applying external magnetic field gradient to the atoms, or modulating the optical lattice potential. The former is appropriate for alkali atoms and dipolar atoms, but for alkaline-earth like atoms such as ytterbium, the only option is the latter due to the extremely small magnetic moment. Therefore, we mainly modulate the optical lattice to engineer the effective Hamiltonian. The common methods to driving the optical lattice are using running wave to modulate the on-site energy of the optical lattice, or periodically modulate the position of the optical lattice to generate inertial force in comoving frame. For any modulation methods, it can be categorized by the range of driving frequency: off-resonant or resonant driving. Some intriguing examples of effective Hamiltonian generated by periodic modulation are discussed in this section.

Driven lattice with off-resonant shaking

When the driving frequency is not resonant with any energy gap in the static system, it is classified as off-resonant driving. We consider one-dimensional optical lattice, whose position is periodically modulated. The dynamics of the atoms

are described by the Hamiltonian

$$\hat{H}_{\text{Lab}}(t) = \frac{\hat{p}_x^2}{2m} + \frac{V_0}{2} \cos \left[\frac{2\pi}{a} (\hat{x} - x_0(t)) \right], \quad (3.32)$$

where $x_0(t) = d \sin(\omega t)$ is trajectory of lattice and V_0 is the lattice potential. By gauge transformation, the Hamiltonian in co-moving frame is given by

$$\begin{aligned} \hat{H}_{\text{cm}}(t) &= \hat{H}_{\text{stat}} - F(t)\hat{x} \\ &= \frac{\hat{p}_x^2}{2m} + \frac{V_0}{2} \cos \left[\frac{2\pi}{a} \hat{x} \right] - F(t)\hat{x}, \end{aligned} \quad (3.33)$$

where $F(t) = -m\ddot{x}_0(t) = F_0 \sin(\omega t)$. In the co-moving frame with moving lattice, the Hamiltonian is given by atoms in static optical lattice with additional time-dependent force term. It is expected that periodic force results in periodic change of momentum, and effective dynamics would be governed by the average of time-dependent momentum shift. To clearly visualize the effect of periodic driving, we will discuss the situation with tight-binding approximation. With tight-binding approximation, the Hamiltonian can be expressed as

$$\hat{H}_{\text{TB}}(t) = \sum_j \left\{ [\epsilon - F(t)aj] c_j^\dagger c_j - t_x (c_j^\dagger c_{j+1} + \text{H.c.}) \right\}, \quad (3.34)$$

where c_j is the annihilation operator for the atom in site j of lattice, $\epsilon = \int dx w^*(x - x_j) \hat{H}_{\text{stat}} w(x - x_j)$ and $t_x = - \int dx w^*(x - x_j) \hat{H}_{\text{stat}} w(x - x_{j+1})$ are on-site energy and nearest-neighbor hopping amplitude, and $w(x - x_j)$ is Wannier function localized at site j . Here, we assume that coupling to higher bands does not occur, because the driving frequency is not resonant to any band gap energy. In this form of Hamiltonian, site-dependent energy offset is periodically modulated. However, the Bloch theorem cannot be applied because of broken translational symmetry. To recover the translational symmetry, unitary operator

$$\hat{U}(t) = \exp \left[\frac{i}{\hbar} \sum_j \int_0^t d\tau F(\tau) a j c_j^\dagger c_j \right] \quad (3.35)$$

is introduced. Under the gauge transformation, the Hamiltonian is given by

$$\hat{H}'_{\text{TB}}(t) = \sum_j \left\{ \epsilon c_j^\dagger c_j - t_x [e^{-i\theta(t)} c_j^\dagger c_{j+1} + \text{H.c.}] \right\}, \quad (3.36)$$

where $\theta(t) = -\frac{a}{\hbar} \int_0^t d\tau F(\tau) = K \cos(\omega t)$, and $K = F_0 a / \hbar \omega$. Now the Hamiltonian describes nearest-neighbor hopping with time-periodic phase called Peierls phase. Fourier components of the Hamiltonian $\hat{H}'_{\text{TB}}(t) = \hat{H}_0 + \sum_{m \neq 0} e^{im\omega t} \hat{H}_m$ are then given by

$$\begin{aligned} \hat{H}_0 &= \sum_j \epsilon c_j^\dagger c_j - t_x \mathcal{J}_0(K) [c_j^\dagger c_{j+1} + \text{H.c.}], \\ \hat{H}_{m \neq 0} &= -t_x \sum_j i^m \mathcal{J}_m(K) [(-1)^m c_j^\dagger c_{j+1} + c_{j+1}^\dagger c_j], \end{aligned} \quad (3.37)$$

and $\hat{H}_{-m} = \hat{H}_m^\dagger$, where \mathcal{J}_m is m th order Bessel function of the first kind. Applying the high-frequency expansion method, the effective Hamiltonian is given by

$$\hat{H}_{\text{eff}} = \hat{H}_0 + \mathcal{O}(1/\omega^2) \approx \sum_j \left\{ \epsilon c_j^\dagger c_j - t_x \mathcal{J}_0(K) [c_j^\dagger c_{j+1} + \text{H.c.}] \right\}, \quad (3.38)$$

as $[\hat{H}_m, \hat{H}_{-m}] = 0$. As a result, periodic off-resonant driving renormalizes the hopping amplitude by zeroth order Bessel function. As K increases, the effective hopping amplitude decreases and its sign can even become negative. The bandwidth and position of band minimum can be adjusted by the dimensionless forcing parameter K [86, 87].

Driven lattice with resonant moving optical lattice

When the driving frequency is resonant to some energy gap in static system, the effective band structure can show intriguing effect. We consider tight-binding

model with site-dependent energy offset,

$$\hat{H}_{\text{stat}} = -t_x \sum_j (c_j^\dagger c_{j+1} + \text{H.c.}) + \sum_j \Delta_j c_j^\dagger c_j. \quad (3.39)$$

Hopping to neighbor sites is inhibited when $|\Delta_{j+1} - \Delta_j| \gg |t|$ as wavefunctions are localized at each site. The hopping between neighbor sites can be restored by periodic modulation. Let the periodic modulation is driven by additional moving optical lattice of potential depth V_m with propagation velocity of $v_m = \omega/2k_m$, where $k_m = \pi/a_m$ is lattice momentum of moving lattice. In tight-binding approximation, the effect of moving lattice potential can lead site-dependent on-site energy modulation and hopping, which can be derived by

$$\begin{aligned} \langle j | \hat{H}_{\text{mod}}(t) | j \rangle &= \frac{V_m}{2} \langle j | \sin(2k_m x + \omega t) | j \rangle \\ &= \frac{V_m}{2} \langle 0 | \sin[2k_m(x + aj) + \omega t] | 0 \rangle \\ &= \frac{V_m}{2} \langle 0 | \sin \left[2k_m x + 2\pi \left(\frac{a}{a_m} \right) j + \omega t \right] | 0 \rangle \\ &= \Phi_0 \sin(\varphi j + \omega t) \end{aligned} \quad (3.40)$$

$$\langle j | \hat{H}_{\text{mod}}(t) | j + 1 \rangle = \Phi_1^c \sin(\varphi j + \omega t) + \Phi_1^s \cos(\varphi j + \omega t), \quad (3.41)$$

where $\varphi = 2\pi(a/a_m)$ and

$$\Phi_0 = \frac{V_m}{2} \langle 0 | \cos(2k_m x) | 0 \rangle, \quad (3.42)$$

$$\Phi_1^c = \frac{V_m}{2} \langle 0 | \cos(2k_m x) | 1 \rangle, \quad (3.43)$$

$$\Phi_1^s = \frac{V_m}{2} \langle 0 | \sin(2k_m x) | 1 \rangle. \quad (3.44)$$

$$(3.45)$$

If the static optical lattice depth is sufficiently large, Φ_1 terms are negligible. Then the Hamiltonian with moving optical lattice can be written as

$$\begin{aligned}\hat{H}(t) &= \hat{H}_{\text{stat}} + \hat{H}_{\text{mod}}(t) \\ &= -t_x \sum_j (c_j^\dagger c_{j+1} + \text{H.c.}) + \sum_j [\Delta_j + \Phi_0 \sin(\varphi j + \omega t)] c_j^\dagger c_j.\end{aligned}\quad (3.46)$$

We can introduce unitary transformation

$$\hat{U}(t) = \exp \left[-\frac{i}{\hbar} \sum_j \left(-\frac{\Phi_0}{\omega} \cos(\varphi j + \omega t) + \Delta_j t \right) c_j^\dagger c_j \right], \quad (3.47)$$

then the transformed Hamiltonian is given by

$$\begin{aligned}\hat{H}'(t) &= \hat{U}^\dagger \hat{H}(t) \hat{U} - i\hbar \hat{U}^\dagger \frac{\partial \hat{U}}{\partial t} \\ &= -t_x \sum_j (e^{-i\theta_j(t)} c_j^\dagger c_{j+1} + \text{H.c.}),\end{aligned}\quad (3.48)$$

where

$$\begin{aligned}\theta_j(t) &= \frac{2\Phi_0}{\hbar\omega} \sin \left[\frac{\varphi(2j+1)}{2} + \omega t \right] \sin \left(\frac{\varphi}{2} \right) + \frac{\delta\Delta_j}{\hbar} t \\ &= K' \sin(\bar{\varphi}_j + \omega t) + \frac{\delta\Delta_j}{\hbar} t\end{aligned}\quad (3.49)$$

is time-dependent hopping phase, and $\delta\Delta_j = \Delta_{j+1} - \Delta_j$. The Hamiltonian can be expanded as

$$\hat{H}'(t) = -t_x \sum_{j,m} \mathcal{J}_m(K') \left[(-1)^m e^{i(m\omega - \frac{\delta\Delta_j}{\hbar})t} e^{im\bar{\varphi}_j} c_j^\dagger c_{j+1} + \text{H.c.} \right]. \quad (3.50)$$

Therefore, the effective Hamiltonian is determined by the time-dependent phase factor $m\omega - \delta\Delta_j/\hbar$, as it decides Fourier components. For example, if the modulation frequency is resonant to the energy separation between neighbor sites, namely $\delta\Delta_j = \nu\hbar\omega$, the effective Hamiltonian is given by

$$\hat{H}_{\text{eff}} \approx \hat{H}_0 = -t_x \sum_j \mathcal{J}_\nu(K') \left[(-1)^m e^{i\nu\bar{\varphi}_j} c_j^\dagger c_{j+1} + \text{H.c.} \right] \quad (3.51)$$

Therefore, non-zero complex hopping phase called Peierl's phase can be engineered by resonant modulation. The site dependent complex phase is given by $\bar{\varphi}_j = \varphi j + \varphi/2$, so it is tunable by adjusting the ratio between lattice constant of static lattice a and moving lattice a_m .

Chapter 4

Topological insulator

Discovery and understanding the phases of matter are important goals in condensed matter physics to reveal microscopic and macroscopic states of the system. The phases of matter can be often explained by Landau theory, which describes that the phase transition can be characterized by spontaneous symmetry breaking of the system. Liquid-solid phase transition can be explained by broken continuous translational symmetry, and ferromagnetism can be described by the result of spin rotational symmetry breaking under the critical temperature. In these phase transition, the long-range order is formed by symmetry breaking. Although Landau's approach can explain the phases of matter and its critical behaviors beautifully, necessity of new paradigm have been claimed after the discovery of quantum Hall effect [27, 88]. Physical properties of quantum Hall states are insensitive to smooth changes in material parameters and details, such as impurity and electron concentration, and it only changes when the system undergoes quantum phase transition without symmetry breaking. It was revealed that topology is closely related to the quantization of Hall conductance, which can be understood in terms of topological invariant.

Topological insulators are gapped insulating phase, but it has gapless states at the edges of system protected by some symmetry. The surface states are robust to the external perturbations, as long as the topology of system is maintained. Due to its intriguing transport property, it has been one of frontiers in modern condensed matter physics. In this chapter, we will review topological insulators. We first start with the Harper-Hofstadter model, which is a representative model of 2D topological states. Then we also review the 1D topological model, the Su-Schrieffer-Heeger (SSH) model and Creutz model.

4.1 Harper-Hofstadter model

Harper-Hofstadter model illustrates the dynamics of the particles in the lattice in the presence of a external magnetic field, so it is discretized version of interger QHE [63–65]. The lattice Hamiltonian can be written as

$$\hat{H} = -t \sum_{n,m} (e^{i\phi_{n,m}^x} \hat{c}_{n+1,m}^\dagger \hat{c}_{n,m} + e^{i\phi_{n,m}^y} \hat{c}_{n,m+1}^\dagger \hat{c}_{n,m} + \text{h.c.}), \quad (4.1)$$

where the $\hat{c}_{n,m}$ is the fermionic annihilation operator at site (n, m) , t is the hopping amplitude between the nearest-neighbor sites, and $\phi_{n,m}^k$ is Peierls phase factor along direction \hat{k} . The Peierls phase is related to the Aharonov-Bohm phase accumulated on moving charged particle in magnetic field. In the absence of magnetic field, lattice system has discrete translational symmetry. If magnetic field $\mathbf{B} = \nabla \times \mathbf{A}$ is applied, the electronic wave function acquires Peierls phase $\phi_{n,m}^k = eA_{n,m}^k/\hbar$ along the hopping between two sites. Then magnetic flux per unit cell of square lattice is given by

$$\Phi_{m,n} = \phi_{m,n}^x + \phi_{m+1,n}^y - \phi_{m,n+1}^x - \phi_{m,n}^y. \quad (4.2)$$

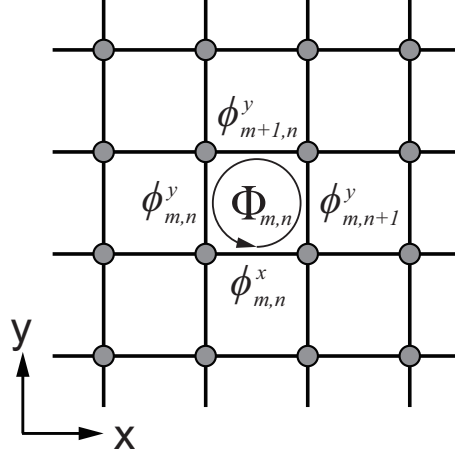


Figure 4.1: Schematic drawing of Harper-Hofstadter model. The amplitude of hopping is given by t , and the hopping phase is given by $\phi_{m,n}^k$. The artificial gauge flux is determined by the difference of Peierls phase in the lattice system, $\Phi_{m,n} = \phi_{m,n}^x + \phi_{m+1,n}^y - \phi_{m,n+1}^x - \phi_{m,n}^y$.

Because of $U(1)$ gauge symmetry, Hamiltonian can be simplified under the proper gauge transformation on \mathbf{A} . The lattice Hamiltonian can be rewritten as

$$\hat{H} = -t \sum_{n,m} (\hat{c}_{n+1,m}^\dagger \hat{c}_{n,m} + e^{i\Phi_{n,m}} \hat{c}_{n,m+1}^\dagger \hat{c}_{n,m} + \text{H.c.}), \quad (4.3)$$

with Landau gauge $\phi_{n,m} = (0, \Phi_{n,m}m)$. Then the hopping phase along \hat{x} becomes real, while the hopping phase along \hat{y} becomes the magnetic flux per each plaquette. This is known as the Harper-Hofstadter Hamiltonian.

Berry phase

When the parameter of the system is slowly altered, a quantum state adiabatically evolves: the eigenstate will remain in eigenstate of instantaneous Hamiltonian. According to the quantum adiabatic theorem, initial eigenstate $|n(\mathbf{R}(0))\rangle$ of Hamiltonian $H(\mathbf{R}(0))$ will stay as eigenstate of the Hamiltonian $H(\mathbf{R}(t))$,

but with some phase factors. Then the instantaneous state can be written as

$$|\psi_n(t)\rangle = e^{i\gamma_n(t)} \exp\left\{-\frac{i}{\hbar} \int_0^t d\tau \epsilon_n(\mathbf{R}(\tau))\right\} |n(\mathbf{R}(t))\rangle. \quad (4.4)$$

The second exponential is known as the dynamical phase factor, and the first exponential is geometric phase factor. The geometric phase can be canceled by proper choice of gauge. From the time-dependent Schrödinger equation $i\hbar\partial_t|\psi_n(t)\rangle = H(\mathbf{R}(t))|\psi_n(t)\rangle$,

$$\partial_t\gamma_n(t) = i\langle n(\mathbf{R}(t))|\nabla_{\mathbf{R}}|n(\mathbf{R}(t))\rangle\partial_t\mathbf{R}(t). \quad (4.5)$$

The total change around the cycle, the geometric phase can be expressed as a path integral

$$\gamma_n = \int_C i\langle n(\mathbf{R})|\nabla_{\mathbf{R}}|n(\mathbf{R})\rangle \cdot d\mathbf{R} = \int_C d\mathbf{R} \cdot \mathcal{A}_n(\mathbf{R}). \quad (4.6)$$

If we make gauge transformation with arbitrary smooth function $\varphi(\mathbf{R})$, as $|n(\mathbf{R})\rangle \rightarrow e^{i\varphi(\mathbf{R})}|n(\mathbf{R})\rangle$, the $\mathcal{A}_n(\mathbf{R})$ also transforms as

$$\mathcal{A}_n(\mathbf{R}) \rightarrow \mathcal{A}_n(\mathbf{R}) - \nabla_{\mathbf{R}}\varphi(\mathbf{R}), \quad (4.7)$$

so $\mathcal{A}_n(\mathbf{R})$ is gauge dependent. As a consequence, geometric phase can be canceled out by suitable gauge transformation. However, it can't be removed if the adiabatic evolution is cyclic, i.e. $\mathbf{R}(0) = \mathbf{R}(T)$, as Berry had found [30]. Because $|n(\mathbf{R}(0))\rangle = |n(\mathbf{R}(T))\rangle$, the gauge transformed states also meet the condition $e^{i\varphi(\mathbf{R}(0))}|n(\mathbf{R}(0))\rangle = e^{i\varphi(\mathbf{R}(T))}|n(\mathbf{R}(T))\rangle$, requiring $\varphi(\mathbf{R}(T)) - \varphi(\mathbf{R}(0)) = 2\pi K$, where $K \in \mathbb{Z}$. Therefore, the geometric phase under cyclic evolution

$$\gamma_n = \oint_C d\mathbf{R} \cdot \mathcal{A}_n(\mathbf{R}), \quad (4.8)$$

is called Berry phase, which is invariant under the gauge choice.

Berry curvature and Chern number

By applying the Stokes theorem,

$$\begin{aligned}\gamma_n &= \int_S d\mathbf{S} \cdot i \left[\left\langle \frac{\partial n(\mathbf{R})}{\partial R^\mu} \middle| \frac{\partial n(\mathbf{R})}{\partial R^\nu} \right\rangle - \left\langle \frac{\partial n(\mathbf{R})}{\partial R^\nu} \middle| \frac{\partial n(\mathbf{R})}{\partial R^\mu} \right\rangle \right] \\ &= \int_S d\mathbf{S} \cdot \Omega_n^{\mu\nu}(\mathbf{R}),\end{aligned}\tag{4.9}$$

where S is closed surface by the path C and $\Omega_n^{\mu\nu}(\mathbf{R})$ is defined as a Berry curvature. $\Omega_n^{\mu\nu}(\mathbf{R})$ can be also written as

$$\Omega_n^{\mu\nu}(\mathbf{R}) = i \sum_{m \neq n} \frac{\langle n | \nabla_{\mathbf{R}} \hat{H} | m \rangle \times \langle m | \nabla_{\mathbf{R}} \hat{H} | n \rangle}{(\epsilon_m - \epsilon_n)^2}.\tag{4.10}$$

In this form of formula, the total Berry curvature vanishes for certain \mathbf{R} , $\sum_n \Omega_n^{\mu\nu}(\mathbf{R}) = 0$, so Berry curvature satisfy local conservation law. In contrast to $\mathcal{A}(\mathbf{R})$, the Berry curvature is gauge invariant local quantity, providing local geometric properties.

Chern theorem is a generalization of Gauss-Bonnet theorem in closed even-dimensional Riemannian manifold [89]. In original Gauss-Bonnet theorem, the total Gaussian curvature of closed surface is given by Euler characteristics of the surface with factor of 2π . The Berry curvature is local curvature that is given by the form of Levi-Civita connection, and its surface is typically in 2D, so it follows the Chern theorem. Therefore, integral of Berry curvature in closed surface divided by 2π is given by integer number, the Chern number $\mathcal{C}_n = \gamma_n/2\pi$. The total Chern number of the system would vanish: $\sum_n \mathcal{C}_n = 0$. The Chern number is *topological invariant*, which is preseved until the gap closing occurs.

Particle-hole symmetry

We use ansatz for wave function

$$\Psi_{m,n} = e^{ik_x ma} e^{ik_y na} \psi_m, \quad (4.11)$$

where $\psi_{m+q} = \psi_q$, $-\pi/(qa) < k_x < \pi/(qa)$ and $-\pi/a < k_y < \pi/a$. Here, q is denominator of rational values of flux, $\Phi/2\pi = p/q$ ($p, q \in \mathbb{Z}$). Then, The Schrödinger equation of Harper-Hofstadter Hamiltonian is given by

$$E\psi_m = -t[e^{ik_x a}\psi_{m+1} + e^{-ik_x a}\psi_{m-1} + 2\cos(k_y a - \Phi m)\psi_m]. \quad (4.12)$$

Let us consider transformation $\Psi_{m,n} \rightarrow \bar{\Psi}_{m,n} = (-1)^{m+n}\Psi_{m,n}$. Then the transformed wave function under same ansatz $\bar{\Psi}_{m,n} = e^{ik_x ma} e^{ik_y na} \bar{\psi}_m$ and $\bar{\psi}_{m+q} = \bar{\psi}_m$ satisfies Schrödinger equation

$$-E\psi_m = -t[e^{ik_x a}\psi_{m+1} + e^{-ik_x a}\psi_{m-1} + 2\cos(k_y a - \Phi m)\psi_m], \quad (4.13)$$

which results in same form of equation but $E \rightarrow -E$. This indicates that if eigenstate $\Psi_{m,n}$ with energy E exist, $\bar{\Psi}_{m,n}$ with energy $-E$ should exist simultaneously. This type of symmetry is referred as *particle-hole symmetry*. The direct relation between two wave function is given by

$$\psi_m(k_x, k_y) = \bar{\psi}(k_x + \pi/a, k_y + \pi/a), \quad (4.14)$$

$$E_l(k_x, k_y) = E_{\bar{l}}(k_x + \pi/a, k_y + \pi/a), \quad (4.15)$$

where $l(\bar{l})$ is l th subband at $E > 0$ ($E < 0$), starting from $E = 0$. As a consequence of particle-hole symmetry, the Berry curvature of l th band has relation of

$$\Omega_l(k_x, k_y) = \Omega_{\bar{l}}(k_x + \pi/a, k_y + \pi/a). \quad (4.16)$$

Then the Chern number of two bands (l, \bar{l}) will be equivalent: $\mathcal{C}_l = \mathcal{C}_{\bar{l}}$.

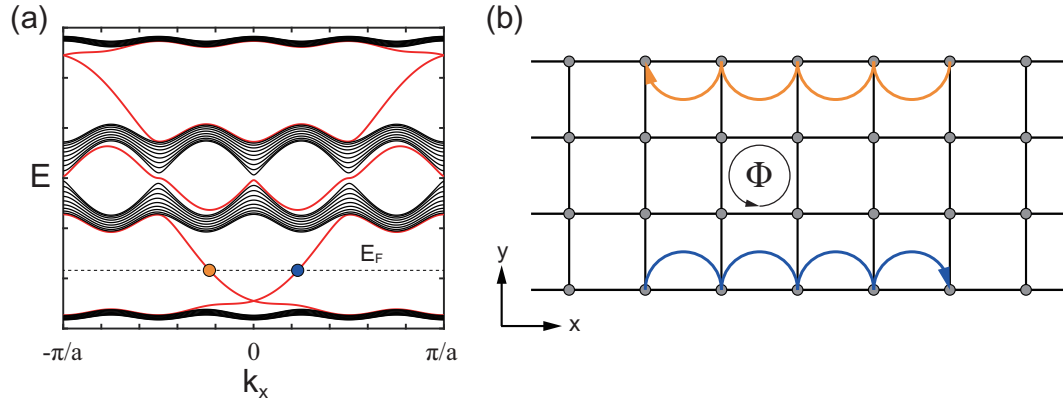


Figure 4.2: Energy spectrum of Harper-Hofstadter model at $\Phi = \pi/2$. The number of sites along y is 41. The edge states (red lines) exist between the bulk spectrum (black lines). When the Fermi energy E_F locates between the bulk gap, currents at two edges flow in opposite direction. (b) Schematic drawing of skipping orbit.

Chiral Edge states

The topological invariant cannot be changed unless the band gap is closed. When the two insulators with different topological invariant are merged with each other, the band gap must be closed and reopened at the interface. Therefore, while the bulk is insulating at some Fermi energy, conducting states exist at the interface.

If one of the insulators is vacuum, then the *edge states* are conducting while the bulk is insulating. For the Harper-Hofstadter model with finite lattice sites in one direction, the energy spectrum shows gapless conducting states at the edges, and the direction of current is opposite [Fig. 4.2]. Therefore, the edge state is *chiral*, because it propagates in only one direction. In the classical point of view, these edge modes can be understood in terms of *skipping orbit* motion, which is a natural consequence of cyclotron motion of a charged particle at the boundary.

of the system.

4.2 1D topological system

4.2.1 Su-Schrieffer-Heeger model

The Su-Schrieffer-Heeger (SSH) model was originally developed to explain soliton formation in polyacetylene [90]. It is linear polymer, and the electron distribution is preferred to have alternate bond strength. Intriguing point is that distinctive two ground states are degenerated. The electronic property of the polyacetylene can be described by 1D tight-binding model with sublattice basis. By neglecting the interactions between electron, the dynamics of single electron in the chain consist of N unit cell can be described by Hamiltonian

$$\hat{H} = J_1 \sum_j (|j, B\rangle\langle j, A| + \text{H.c.}) + J_2 \sum_j^{N-1} (|j+1, A\rangle\langle j, B| + \text{H.c.}), \quad (4.17)$$

where $|j, \alpha\rangle$ with $j \in \{1, \dots, N\}$ and $\alpha \in \{A, B\}$ denotes the state of the electron in j th unit cell and sublattice α . J_1 and J_2 describe intra and inter unit cell hopping (figure 4.3). Corresponding Bloch Hamiltonian is given by

$$\mathcal{H}(k) = [J_1 + J_2 \cos(k)]\sigma_x + J_2 \sin(k)\sigma_y = \mathbf{h}(k) \cdot \boldsymbol{\sigma}, \quad (4.18)$$

where $\boldsymbol{\sigma} = \{\sigma_x, \sigma_y, \sigma_z\}$ are 2×2 Pauli matrices. The dispersion relation is given by $E(k) = \pm \sqrt{J_1^2 + J_2^2 + 2J_1J_2 \cos(k)}$. The energy dispersion clearly shows that SSH model has gapped phase when $J_1 \neq J_2$. At half-filling, the energy of occupied states can be decreased when the hopping amplitudes are staggered, so alternate bond configuration is energetically favorable. This staggered hopping (or dimerization) due to the coupling with phonon modes is called Peierls instability.

From the momentum space representation, the Bloch Hamiltonian, bulk property can be well described. Then, we are going to look through the property of finite size chain in the fully dimerized limit. When $|J_1| > 0$, $J_2 = 0$, every unit cells are dimerized. The eigenstates are given by

$$\hat{H}(|j, A\rangle \pm |j, B\rangle) = \pm J_1(|j, A\rangle \pm |j, B\rangle), \quad (4.19)$$

showing gapped bulk energy. In another limit, the chain shows intriguing property. When $J_1 = 0$ and $|J_2| > 0$, the bulk eigenstates are given by

$$\hat{H}(|j, B\rangle \pm |j + 1, A\rangle) = \pm J_2(|j, B\rangle \pm |j + 1, A\rangle), \quad (4.20)$$

so bulk eigenenergy is gapped again. However, at the end of chain, there exist degenerated zero-energy modes,

$$\hat{H}|1, A\rangle = \hat{H}|N, B\rangle = 0. \quad (4.21)$$

Chiral symmetry and winding number

The SSH model has two sublattice sites in one unit cell. The projector of sublattices are given by

$$\hat{P}_\alpha = \sum_{j=1}^N |j, \alpha\rangle \langle j, \alpha|, \quad (4.22)$$

where $\alpha \in \{A, B\}$. We can define operator

$$\hat{\Gamma} = \hat{P}_A - \hat{P}_B. \quad (4.23)$$

This operator is hermitian ($\hat{\Gamma}^\dagger = \hat{\Gamma}$) and unitary $\hat{\Gamma}^\dagger \hat{\Gamma} = 1$. Then the SSH Hamiltonian satisfies the following relation.

$$\hat{\Gamma} \hat{H} \hat{\Gamma} = -\hat{H}. \quad (4.24)$$

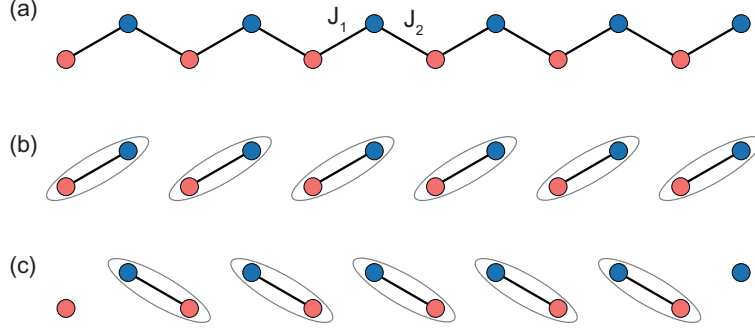


Figure 4.3: Schematic diagram of Su-Schrieffer-Heeger model. (a) It is bipartite 1D chain with intracell hopping J_1 and intercell hopping J_2 . (b) In the limit of zero intercell hopping $J_2 = 0$, all the lattice sites are dimerized. (c) In the limit of intracell hopping $J_1 = 0$, the lattice sites also dimerized again, but the end sites are remained uncoupled.

This relation indicates that the spectrum of Hamiltonian is symmetric, because if there exists state $|\psi\rangle$ with energy E , there is symmetric state $\hat{\Gamma}|\psi\rangle$ with energy $-E$. This type of symmetry is called *chiral symmetry*.

The bulk Hamiltonian satisfies following relation,

$$\sigma_z \mathcal{H}(k) \sigma_z = -\mathcal{H}(k). \quad (4.25)$$

Because of the chiral symmetry, the hamiltonian vector $\mathbf{h}(k)$ is confined in the $\sigma_x - \sigma_y$ plane. Then we can define *winding number* of the system to describe topological property of the system [34]

$$\nu = \frac{1}{2\pi i} \int_{\text{BZ}} dk \frac{d}{dk} \log[\mathbf{h}(k)]. \quad (4.26)$$

The winding number counts the number of times that $\mathbf{h}(k)$ wraps the origin through the Brillouin zone $k = 0 \rightarrow 2\pi$. Therefore, it is global property. Following this definition, winding number $\nu = 0$ when $|J_2| < |J_1|$, while $\nu = 1$ when $|J_2| > |J_1|$. Then we can classify the phase at $|J_2| > |J_1|$ is *topologically*

non-trivial, which has edgestates, while $|J_2| < |J_1|$ is topologically trivial. Winding number defined in bulk can predict the number of edge states, so it follows *bulk-edge correspondence*. Alternatively, The topological invariant can be also characterized by the 1D Berry phase, which is called *Zak phase* [91]

$$\gamma_n = i \int_{BZ} dk \langle u_n(k) | \partial_k | u_n(k) \rangle, \quad (4.27)$$

where n is band index and $|u_n(k)\rangle$ is eigenstates of $\mathcal{H}(k)$. It is given by $\gamma = \pi$ for non-trivial phase, and $\gamma = 0$ for trivial phase.

The winding number, or the number of edgestates are topological invariant. During the continuous change (or, deformation) of parameters, these numbers are invariant unless the bulk gap is closed. If the parameters cross the gapless point $J_1 = J_2$, topological invariants are suddenly changed, showing topological phase transition.

4.2.2 Creutz ladder

Creutz ladder was first introduced to study end states in the context of lattice gauge theory [92]. Creutz ladder describes cross-linked ladder under the magnetic field. The tight-binding Hamiltonian is given by

$$\hat{H} = - \sum_j \left[K(e^{i\theta} a_j^\dagger a_{j+1} + e^{-i\theta} b_j^\dagger b_{j+1}) + Kr(a_j^\dagger b_{j+1} + b_j^\dagger a_{j+1}) + M(a_j^\dagger b_j) + \text{H.c.} \right], \quad (4.28)$$

where a_j and b_j are fermionic annihilation operators at the n th site of the upper/lower legs. The first term describes the hopping in each leg, and complex phase θ is due to the magnetic field. Second term and third terms describe cross-link and vertical hopping between two legs, respectively. The Bloch Hamiltonian

is given by

$$\begin{aligned}\mathcal{H}(k) &= 2K \cos(k) \cos(\theta) I + [M + 2Kr \cos(k)] \sigma_x + 2K \sin(k) \sin(\theta) \sigma_z \\ &= 2K \cos(k) \cos(\theta) I + \mathbf{h}(k) \cdot \boldsymbol{\sigma}\end{aligned}\quad (4.29)$$

where I is 2×2 identity matrix. In the case of $\theta = \pi/2$ and no vertical hopping $M = 0$, the topological features can be easily captured. In the limit of $r = 1$, the eigenenergy $\epsilon_{\pm} = \pm 2K$. Considering hopping paths, particles cannot hop two sites apart due to destructive interference between paths. Corresponding eigenstates can be found as

$$|\pm\rangle_j = \frac{1}{2} \{i|j, a\rangle + |j, b\rangle \mp (|j+1, a\rangle + i|j+1, b\rangle)\}, \quad (4.30)$$

where $|j, \alpha\rangle$ is state at j th site and leg α . Accordingly, fermions are confined to the square plaquette and cannot diffuse through the lattice. At the edges of the lattice, we can find another type of eigenstates,

$$\begin{aligned}|0\rangle_1 &= \frac{1}{\sqrt{2}}(|1, a\rangle + i|1, b\rangle) \\ |0\rangle_N &= \frac{1}{\sqrt{2}}(|N, a\rangle - i|N, b\rangle).\end{aligned}\quad (4.31)$$

These zero-energy two states are confined to the edge sites $j = 1, N$, resulting in the system topologically non-trivial. It is reminiscent of previous fully dimerized SSH model, but the edge states in Creutz ladder occurs due to quantum interference. The winding number $\nu = 1$ clearly shows bulk-edge correspondence. In another limit of Creutz ladder such as $M \neq 0$ and $r = 0$, fermions can be diffuse throughout the whole lattice without such a zero energy edge modes.

For $\theta = \pi/2$, the Hamiltonian has chiral symmetry as $\sigma_y \mathcal{H}(k) \sigma_y = -\mathcal{H}(k)$. Accordingly, $\mathbf{h}(k)$ is confined in $\sigma_x - \sigma_z$ plane, and winding number and Zak phase are quantized. In general case, chiral symmetry no longer holds

due to non-zero identity term. Although chiral symmetry is broken, the Hamiltonian has another type of symmetry $\sigma_x \mathcal{H}(k) \sigma_x = \mathcal{H}(-k)$, and it also confines the $\mathbf{h}(k)$ in the $\sigma_x - \sigma_z$ plane. Therefore, the winding number and Zak phase can be properly defined.

4.3 Synthetic dimension and topological ladders

We reviewed three simple topological models. In practical point of view, topological Hamiltonians can be realized by implementing gauge field (Harper-Hofstadter model), or manipulate different tunneling terms (intra- and inter-cell hopping in SSH model / vertical and diagonal hopping in Creutz ladder). The ultracold atoms in optical lattices easily provides the lattice Hamiltonian, but gauge field is difficult to be produced by external magnetic field due to its charge neutrality. Also, quantum tunneling longer than the nearest-neighbor hopping cannot be independently controlled with monochromatic laser.

Up to now, some techniques have been developed to engineer topological Hamiltonian in optical lattice. The artificial gauge field in 2D optical lattice system can be implemented by laser-assisted tunneling [60–62]. By adding linear energy offset in 2D optical lattice to suppress the next-nearest tunneling, and applying resonant moving optical lattice, the next-nearest tunneling is restored with complex phase. Then the effective Hamiltonian of this system can be engineered to the Harper-Hofstadter Hamiltonian [61,62]. SSH model can be realized by bichromatic lasers with harmonic wavelength λ and 2λ . The double-well optical lattice, which is formed by overlapping two optical lattice potential,

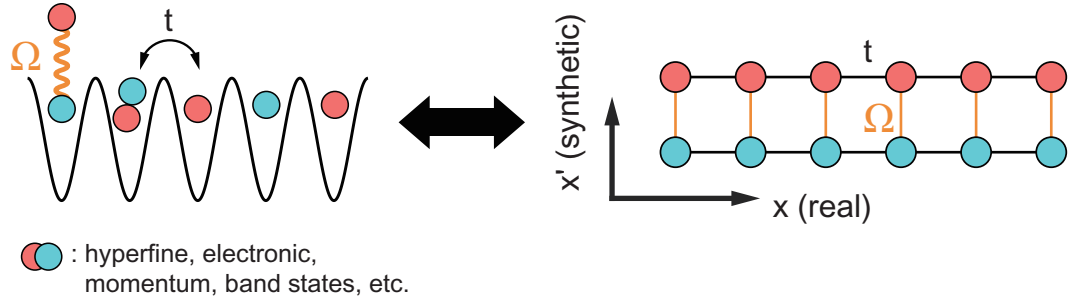


Figure 4.4: Concept of synthetic dimension. The internal degrees of freedom, such as hyperfine, electronic, momentum, or band states, can be regarded as extra dimension. If different internal states are resonantly coupled, the resonant coupling between these states are regarded as hopping constant along that direction. Then the dynamics in 1D optical lattice with internal states can be directly mapped to the ladder Hamiltonian.

then exactly describes the SSH Hamiltonian [93].

We demonstrated topological ladders under the concept of *synthetic dimension*. The typical lattice sites are physically identified by the spatial location. In our world, the spatial dimension is restricted to 3D. Synthetic dimension is a direct mapping of some degrees of freedom to the extra dimensions [94,95]. For example, if the spin states are regarded as lattice sites, spin degrees of freedom is directly mapped to extra dimension. Then the resonant coupling between spin states is mapped to hopping along that dimension. Applying synthetic dimension on ultracold atoms in 1D optical lattice, the ladder system is naturally obtained.

This concept has advantages on the topological band engineering with optical lattice. First, the edges along the synthetic dimension is sharply defined. In conventional 2D optical lattice, the boundary of the system cannot be sharply defined by lattice lasers only. The boundary of the system should be defined by another repulsive potentials. In contrast, 2D lattice system composed of

1D optical lattice and synthetic dimension naturally has sharp boundary, so physics at the edges can be easily observed. Second, the sites along synthetic dimension can be individually addressable. Therefore, the atoms indexed with specific lattice site can be observed separately, and hopping constant can be selectively engineered.

For example, atomic hyperfine states splitted by Zeeman effect can be resonantly coupled by Raman transition. Because the Raman transition is moving optical lattice, the resonant coupling between two hyperfine states accompanies with lattice position dependent complex phase, as we discussed in Chapter 3. Therefore, the dynamics described by effective Hamiltonian contains the artificial gauge field. This approach allows to explore the chiral current at the edge of the system via state-selective measurement [96, 97].

After this chapter, we will present the experimental results on the realization of topological ladders in two different ways: via moving optical lattice (Raman coupling) and periodic shaking. First method has advantage on tunable gauge flux, while the latter has possibility on the independent control of vertical/diagonal hopping. Therefore, these methods can allow to explore the chiral edge physics under the artificial gauge field, and the 1D topological phase in Creutz model, respectively.

Chapter 5

Cross-linked chiral Hall ladder with band states

This chapter describes realization of synthetic Hall ladder consists of band states. In the ladder, the legs are formed by the orbital states of the optical lattice and the complex inter-leg links are generated by the orbital-changing Raman transitions that are driven by a moving lattice potential superimposed onto the optical lattice. The effective magnetic flux per ladder plaquette is tuned by the spatial periodicity of the moving lattice, and the chiral currents are observed from the asymmetric momentum distributions of the orbitals. The effect of the complex cross links is demonstrated in quench dynamics by measuring the momentum dependence of the inter-orbital coupling strength. The experimental results are published in the following paper.

- J. H. Kang, J. H. Han, and Y. Shin, “*Realization of a Cross-Linked Chiral Ladder with Neutral Fermions in a 1D Optical Lattice by Orbital-Momentum Coupling,*” Physical Review Letters **121**, 150403 (2018).

5.1 Introduction

Topological states of matter represent one of the frontiers of modern condensed matter physics [88, 98]. Featuring tunable artificial gauge fields and spin-orbit coupling [79], ultracold atoms in optical lattices provide a versatile platform to realize topological states and study their phase transitions in a clean and well-controlled manner [43, 47]. The Hofstadter-Harper model, which is the paradigmatic example of a topological Chern insulator, was realized in two-dimensional (2D) optical lattices using laser-assisted tunneling effects [61, 62]; the Haldane model was demonstrated in a hexagonal optical lattice by activating complex next-nearest-neighbor (NNN) hopping with lattice shaking [66]. The high tunability of the experimental parameters may enable one to explore a broad range of topological states even beyond the conventional Altland-Zirnbauer classification [32, 99].

In recent optical-lattice experiments, an interesting framework was introduced to realize chiral ladder systems with one-dimensional (1D) optical lattices, where the internal atomic degrees of freedom, such as hyperfine spin, are taken as a finite synthetic dimension and an artificial gauge field is engineered by laser-induced couplings between the internal states [94, 95]. The synthetic ladder systems are highlighted by their edges, which are intrinsically sharp and can be detected by internal-state-selective imaging, thus allowing direct observation of the chiral edge currents in the systems [96, 97, 100]. Ladders with complex hopping amplitudes have been discussed as a minimal model for 1D topological matter [92] and also as a quasi-1D version of the Hofstadter problem for studying the edge-mode states in 2D topological insulators [101]. In particular, it is well recognized that NNN hopping, i.e., diagonal cross links between the legs,

are responsible for the emergence of topologically non-trivial phases in the ladder system subject to a magnetic field [101–103]. Therefore, extensive control of the complex inter-leg links is highly desirable in synthetic ladder experiments.

In this paper, we report the experimental demonstration of a synthetic ladder scheme using the orbital degree of freedom of the optical lattice system. The legs of the ladder are formed by the orbital states, and the inter-leg hoppings are generated by orbital-changing two-photon Raman transitions that are resonantly driven by a moving lattice potential. The complex hopping amplitude is spatially modulated, giving rise to an effective magnetic flux Φ per ladder plaquette, which we demonstrate by observing the corresponding chiral currents of the orbital states. The key feature of our orbital-based ladder system is that the cross inter-leg links are significantly strong due to the favorable condition for the spatial overlap of the orbital wave functions. The complex cross link effect is manifested in the momentum dependence of the inter-orbital coupling strength, which we directly demonstrate via momentum-resolving analysis of the quench dynamics of the ladder system. Finally, we discuss the topological phase transition, which can occur in the system by further controlling the cross link, possibly via tailoring the orbital wave functions. Our results present a new perspective for studies of topological phases with optical lattice systems using the orbital degree of freedom [104–106].

5.2 Experimental setup

The experimental setup for optical lattice and Raman coupling is sketched in Fig. 5.1. A two-dimensional rectangular optical lattice is generated by using Gaussian laser beams with a wavelength of $\lambda_L = 532$ nm, where a single laser

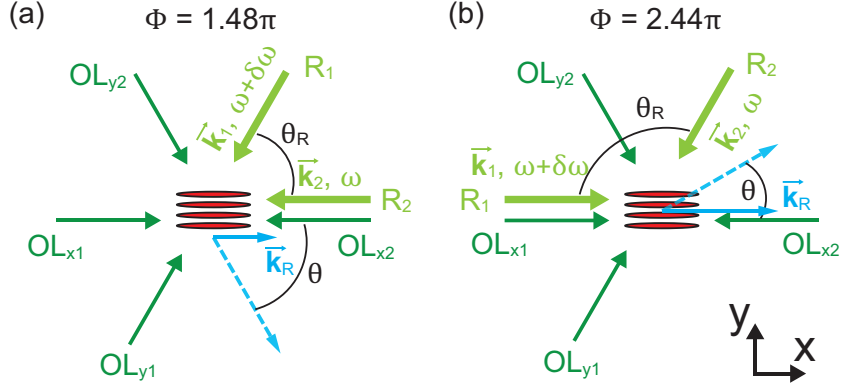


Figure 5.1: Experimental setup for optical lattice and Raman coupling. A rectangular optical lattice is formed by two pairs of 532 nm laser beams ($\{OL_{x1}, OL_{x2}\}$ and $\{OL_{y1}, OL_{y2}\}$) and the inter-orbital Raman coupling is generated by two 556 nm laser beams (R_1 and R_2). Raman beam configurations for (a) $\Phi = 2\pi(k_R/k_L) + \pi = 1.48\pi$ and (b) 2.44π .

beam is propagating and retro-reflected along x -axis, and two laser beams are placed in the xy plane symmetrically with respect to the x -axis to intersect with each other at the angle of $2\pi/3$. The lattice constants for x and y directions are given by $a_x = \lambda_L/2 = \pi/k_L$ and $a_y = \lambda_L/\sqrt{3}$, respectively. The waists of the lattice beams are $\approx 80 \mu\text{m}$ and the laser beam frequency for the y -axis lattice is shifted by 200 MHz from that of the x -axis beam. In our experiment, the depth of the lattice potential is set to be $V_{L,x} = 5E_{L,x}$ ($V_{L,y} = 20E_{L,y}$) along the x (y) direction, where $E_{L,x(y)} = \frac{\hbar^2 \pi^2}{2ma_{x(y)}^2} = h \times 4.1(3.1) \text{ kHz}$ and m is the atomic mass. The lattice depths were calibrated by lattice amplitude modulation spectroscopy [77].

The moving lattice potential for inter-orbital Raman coupling is generated by using two Gaussian laser beams with a wavelength of $\lambda_R = 556 \text{ nm}$, which is blue-detuned by 1.94 GHz from the 1S_0 - 3P_1 narrow intercombination transition line of ^{173}Yb . The beam waists are $150 \mu\text{m}$, much larger than the

sample radius of $16\text{ }\mu\text{m}$, and the intensity variations of the laser beams over the sample are negligible. This is important to suppress the mechanical perturbations to the sample caused by the inhomogeneous AC Stark shift at a sudden turn-on of the Raman beams. In our experiment, the frequency difference ω for the two laser beams is much smaller than the band gap energy associated with the y -axis lattice potential and the y -directional Raman coupling is energetically prohibited. The wave number k_R of the x -directional Raman coupling is given by $k_R = (\vec{k}_1 - \vec{k}_2) \cdot \hat{x} = \frac{2\pi}{\lambda_R} \sin \theta_R \cos \theta$, where $\vec{k}_{1,2}$ are the wave vectors of the two Raman beams, $2\theta_R$ is the angle between \vec{k}_1 and \vec{k}_2 , and θ is the angle of $\vec{k}_1 - \vec{k}_2$ to the x -axis. In Fig. 5.1, the two Raman-coupling configurations used in the experiment are shown, which correspond to $\Phi = k_R/k_L + \pi = 1.48\pi$ and 2.44π , respectively. The magnitude t_0^s of the coupling between the s and p bands was experimentally determined by measuring the momentum-averaged Rabi frequency of band population oscillations, where the oscillations were induced by suddenly turning on the Raman beams to a sample prepared in the s band. For our experimental condition, the d -band population was less than 8% during the oscillations.

5.3 Effective Hamiltonian

We consider a system of non-interacting spinless fermions in an 1D lattice potential $V(x) = V_L \cos^2(k_L x)$, where the fermions are perturbed by a moving lattice potential, $\delta V(x, t) = V_R \cos^2(k_R x - \frac{\omega t}{2})$ [Fig. 5.2(a)]. The Hilbert space of the system is spanned by the Wannier states $\{|j, \alpha\rangle\}$ of the stationary lattice potential, where j and α are the indices for the lattice site and orbital, respectively. Regarding the orbital degree of freedom as a virtual dimension orthogonal to

the real lattice dimension, the system can be viewed as a synthetic 2D lattice system that has a sharp edge formed by the s orbital, as depicted in Fig. 5.2(b). When the modulation frequency ω of the moving lattice potential is close to a band gap, orbital-changing Raman transitions are resonantly driven, realizing hoppings for the synthetic dimension.

In the multi-band tight-binding approximation [107], the Hamiltonian of a particle in an one-dimensional (1D) lattice potential $V(x) = V_L \cos^2(k_L x)$ is given by

$$H_0 = \sum_{j,\alpha} \left[\epsilon_\alpha c_{j,\alpha}^\dagger c_{j,\alpha} + \left((-1)^{\alpha+1} t_\alpha^r c_{j,\alpha}^\dagger c_{j+1,\alpha} + \text{h.c.} \right) \right], \quad (5.1)$$

where $c_{j,\alpha}$ ($c_{j,\alpha}^\dagger$) is the annihilation (creation) operator of the particle in the Wannier state $|j, \alpha\rangle$ localized at lattice site j in α band ($\alpha = 0, 1, 2, \dots$ for s, p, d, \dots). The on-site energy ϵ_α and the tunneling amplitude t_α^r are given by

$$\epsilon_\alpha = \langle j, \alpha | \left[\frac{p^2}{2m} + V(x) \right] | j, \alpha \rangle \quad (5.2)$$

$$t_\alpha^r = (-1)^{\alpha+1} \langle j, \alpha | \left[\frac{p^2}{2m} + V(x) \right] | j+1, \alpha \rangle. \quad (5.3)$$

Now we consider a situation where the particle is perturbed by a moving lattice potential, $\delta V(x, t) = V_R \cos^2(k_R x - \frac{\omega t}{2})$. At the same level of approximation, the perturbations can be described by

$$H' = \sum_{j,l} \sum_{\alpha,\beta} \langle j, \alpha | \delta V(x, t) | j+l, \beta \rangle c_{j,\alpha}^\dagger c_{j+l,\beta}, \quad (5.4)$$

where $l \in \{-1, 0, 1\}$. In the case that the moving lattice frequency ω is close to the band gap energy, the couplings between adjacent orbitals, i.e., $|\alpha - \beta| = 1$ are most relevant and the perturbation Hamiltonian H' can be further approximated as

$$H' = \sum_{j,\alpha} \sum_{l=0,\pm 1} \left(\langle j, \alpha | \delta V(x, t) | j+l, \alpha+1 \rangle c_{j,\alpha}^\dagger c_{j+l,\alpha+1} + \text{h.c.} \right). \quad (5.5)$$

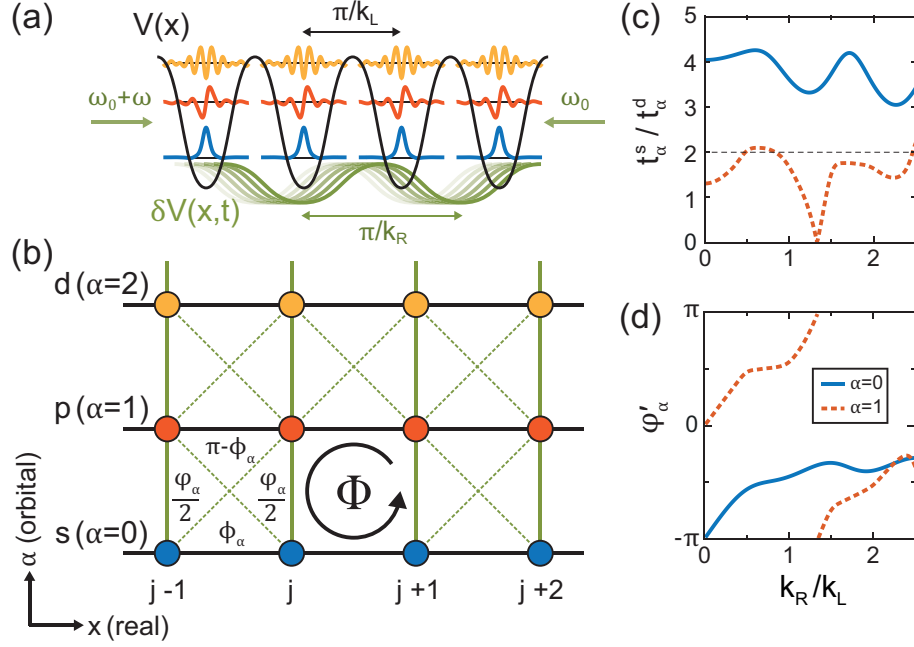


Figure 5.2: Orbital-momentum coupling in an optical lattice. (a) Schematic of the experimental setup. Atoms are in a stationary 1D optical lattice potential $V(x)$, with lattice constant π/k_L , and driven by a moving lattice potential $\delta V(x,t)$, with lattice constant π/k_R . The moving lattice induces two-photon Raman transitions between the orbital states of the stationary lattice. (b) Ladder description of the system. The orbitals constitute the ladder legs along the real x dimension and the Raman coupling provides the inter-leg links. The complex coupling amplitude is spatially modulated, resulting in an effective magnetic flux per plaquette, $\Phi = 2\pi(k_R/k_L) + \pi$. The subplaquette flux distribution is assigned in accordance with the cross-links indicated by the diagonal dashed green lines. (c) Amplitude ratio for the direct to diagonal hopping, t_α^s/t_α^d and (d) their phase difference ϕ'_α as functions of k_R/k_L .

Using $\langle j, \alpha | k, \beta \rangle = 0$ for $\alpha \neq \beta$, the coupling amplitude can be expressed as

$$\begin{aligned}
& \langle j, \alpha | V_R \cos^2 \left(k_R x - \frac{\omega t}{2} \right) | j + l, \alpha + 1 \rangle \\
&= \frac{V_R}{2} \langle 0, \alpha | \cos \left(2k_R(x + a_x j) - \omega t \right) | l, \alpha + 1 \rangle \\
&= \frac{V_R}{2} \left[C_\alpha^l \cos(\varphi j - \omega t) - S_\alpha^l \sin(\varphi j - \omega t) \right]
\end{aligned} \tag{5.6}$$

where $a_x = \pi/k_L$ is the lattice spacing, $\varphi = 2\pi(k_R/k_L)$, $C_\alpha^l = \langle 0, \alpha | \cos(2k_R x) | l, \alpha + 1 \rangle$, and $S_\alpha^l = \langle 0, \alpha | \sin(2k_R x) | l, \alpha + 1 \rangle$.

In the rotating-wave approximation under unitary transformation

$$U_R(t) = \sum_{j,\alpha} e^{i\alpha(\omega t + \frac{\pi}{2})} c_{j,\alpha}^\dagger c_{j,\alpha}, \tag{5.7}$$

the total Hamiltonian of the system is given by

$$\begin{aligned}
H &= H_0 + H' \\
&= \sum_{j,\alpha} \left[\epsilon'_\alpha c_{j,\alpha}^\dagger c_{j,\alpha} + ((-1)^{\alpha+1} t_\alpha^r c_{j,\alpha}^\dagger c_{j+1,\alpha} + \text{h.c.}) \right. \\
&\quad + \frac{1}{2} (t_\alpha^s e^{-i\varphi j} c_{j,\alpha}^\dagger c_{j,\alpha+1} + \text{h.c.}) \\
&\quad \left. + \frac{1}{2} \sum_{l=\pm 1} (t_\alpha^d e^{-i(\varphi j + \varphi'_\alpha l)} c_{j,\alpha}^\dagger c_{j+l,\alpha+1} + \text{h.c.}) \right],
\end{aligned} \tag{5.8}$$

where $\epsilon'_\alpha = \epsilon_\alpha - \alpha \hbar \omega$, $t_\alpha^s = \frac{V_R}{2} S_\alpha^0$, $t_\alpha^d = \frac{V_R}{2} |S_\alpha^1 - iC_\alpha^1|$, and $\varphi'_\alpha = \arg(S_\alpha^1 - iC_\alpha^1)$. In the derivation, we used the relations of $C_\alpha^0 = 0$, $C_\alpha^{-1} = -C_\alpha^1$, and $S_\alpha^{-1} = S_\alpha^1$, which are easily inferred from the parity property of the Wannier states. The coefficients are determined by the distribution of Wannier states and the ratio k_R/k_L , as shown in Fig. 5.3. Therefore, the ratio between t_α^s , t_α^d , and phase term φ'_α are mainly determined by k_R/k_L at fixed optical lattice depth.

In effective Hamiltonian, the first term is the on-site energy in the rotating frame; the second and third terms describe the nearest neighbor hopping along

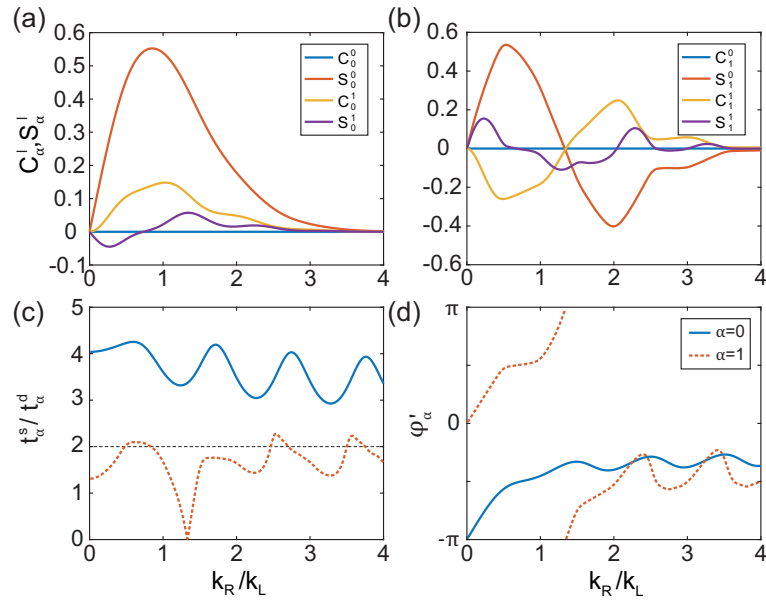


Figure 5.3: Raman coupling coefficients C_α^l and S_α^l ($l = 0, 1$) as functions of k_R/k_L for (a) s - p orbital coupling ($\alpha = 0$) and (b) p - d orbital coupling ($\alpha = 1$). (c, d) Corresponding t_α^s/t_α^d and φ'_α .

the real and synthetic directions, respectively; and the fourth term represents the NNN, diagonal hopping in the 2D rectangular lattice. The position dependent complex phase factor $e^{i\varphi j}$ for orbital-changing hopping results from the spatial variation of the phase of the moving lattice potential and $\varphi = 2\pi(k_R/k_L)$. When a fermion hops around a unit cell, it acquires a net phase of $\Phi = \varphi + \pi$, which can be interpreted as a magnetic flux piercing through the lattice plaquette [61,62]. Here the phase of π in Φ is due to parity inversion between two intermediate orbitals. Taking into account the additional complex phase factor $e^{i\varphi'_\alpha l}$ for diagonal hopping, a subplaquette flux distribution can be assigned, as shown in Fig. 5.2(b), where $\phi_\alpha = \varphi/2 - \varphi'_\alpha$. For given orbital wave functions, t_α^s/t_α^d and φ'_α are determined to be functions of k_R/k_L [Figure 5.3].

The momentum-space representation of the system can be obtained by the gauge and Fourier transformation

$$c_{j,\alpha} = (2N)^{-1/2} \sum_q e^{i[(\alpha-1)\varphi+\pi]j} e^{iqj} c_{q,\alpha}, \quad (5.9)$$

where $2N$ is the number of lattice site and $q = n\frac{\pi}{N}$ ($n = -(N-1), \dots, N$) is the quasi-momentum of the lattice. The Hamiltonian in momentum space is

$$\begin{aligned} H = & \sum_{q,\alpha} \left[\epsilon'_\alpha + (-1)^\alpha 2t_\alpha^r \cos[q + (\alpha-1)\varphi] \right] c_{q,\alpha}^\dagger c_{q,\alpha} \\ & + \frac{1}{2} \sum_{q,\alpha} \left[\hbar\Omega_\alpha(q) c_{q,\alpha}^\dagger c_{q,\alpha+1} + \text{h.c.} \right], \end{aligned} \quad (5.10)$$

where $\hbar\Omega_\alpha(q) = t_\alpha^s - 2t_\alpha^d \cos(q + \alpha\varphi - \varphi'_\alpha)$, which shows that the momentum dependence of the inter-orbital coupling strength results from the orbital-changing hopping process with $t_\alpha^d \neq 0$.

5.4 Ground state and chiral current

Our experiment starts with the preparation of a spin-polarized degenerate Fermi gas of ^{173}Yb atoms in the $|F, m_F\rangle = |5/2, -5/2\rangle$ hyperfine spin state, as described in Ref. [70]. The total atom number is $N \approx 1.0 \times 10^5$ and the temperature is $T/T_F \approx 0.3$, where T_F is the Fermi temperature of the trapped sample. The atoms are adiabatically loaded in a 2D optical lattice, which is formed by laser light with a wavelength of $\lambda_L = 532$ nm in the xy horizontal plane. The lattice spacing and depth are $a_x = \lambda_L/2$ ($a_y = \lambda_L/\sqrt{3}$) and $V_{L,x} = 5E_{L,x}$ ($V_{L,y} = 20E_{L,y}$) along the x (y) direction, respectively, where $E_{L,x(y)} = \frac{\hbar^2 \pi^2}{2ma_{x(y)}^2} = h \times 4.1(3.1)$ kHz and m is the atomic mass. Since the y -axis motion is frozen by the high lattice depth $V_{L,y}$ and the z -axis motion is irrelevant in the following experiment, our system realizes an effective 1D lattice system. Here, $k_L = \pi/a_x$ and the tunneling amplitudes are $\{t_0^r, t_1^r, t_2^r\} = h \times \{0.27, 1.72, 3.90\}$ kHz [77]. The trapping frequencies of the overall harmonic potential are estimated to be $\{\omega_x, \omega_y, \omega_z\} \approx 2\pi \times \{64, 49, 135\}$ Hz. After loading the atoms in the lattice, the fractional population of the p orbital is less than 6%.

The frequency difference ω for the two Raman beams is set to $\omega_c = [(\epsilon_1 - 2t_1^r) - (\epsilon_0 - 2t_0^r)]/\hbar$, matching the energy difference between the dispersion minima of the s and p bands. Under this condition, the coupling to orbitals higher than the d orbital is off resonance and the system can be approximated as a three-leg ladder consisting of s , p , and d orbitals. Then, the Bloch Hamiltonian

of the three-leg ladder in momentum space is given by

$$H(q; \Phi) = \begin{pmatrix} \epsilon_0(q - \Phi) & \hbar\Omega_0(q)/2 & 0 \\ \hbar\Omega_0(q)/2 & \epsilon_1(q) - \hbar\omega & \hbar\Omega_1(q)/2 \\ 0 & \hbar\Omega_1(q)/2 & \epsilon_2(q + \Phi) - 2\hbar\omega \end{pmatrix}, \quad (5.11)$$

where the α -orbital energy dispersion is $\epsilon_\alpha(q) = \epsilon_\alpha - 2t_\alpha^r \cos(q)$ and the α -($\alpha+1$) orbital coupling is $\hbar\Omega_\alpha(q) = t_\alpha^s - 2t_\alpha^d \cos(q + \alpha\varphi - \varphi'_\alpha)$. Here, q is Bloch quasi-momentum normalized by a_x^{-1} . Figs. 5.4(a) and (b) show the energy structures of the ladder system for our experimental conditions. The orbital-mixed ground band has a chiral region with only one pair of Fermi points, which is analogous to the chiral edge states in the integer quantum Hall effect [101, 108]. We note that the cross links of the ladder are manifested in the momentum dependence of $\Omega_\alpha(q)$. In particular, when $2t_\alpha^d > t_\alpha^s$, $\Omega_\alpha(q)$ changes its sign over a certain momentum range, implying that the topological character of the bands can change for a strong t_α^d . For the two cases of $\Phi = 1.48\pi$ and 2.44π , $\{t_0^s/t_0^d, t_1^s/t_1^d\}$ are estimated to be $\{4.2, 1.5\}$ and $\{4.2, 2.1\}$, respectively.

In equilibrium, the relative motion between pseudospin states can be captured by momentum distribution. If chiral current exists in the system, motion of atoms in different legs show non-zero relative velocity. For ground bands in Figs. 5.4(a) and (b), the momentum distribution $n(k)$ of orbital states show asymmetry. Here, the atoms in α band are transferred to the α -th Brillouin zone in the momentum space of free fermions, i.e., $\alpha < |k| < \alpha + 1$ (k is expressed in units of k_L). The asymmetry can be quantified by function $h(k) = n(k) - n(-k)$, which is directly related to the chiral current. We note that our orbital-based synthetic ladder shows an explicit broken leg symmetry $t_\alpha^r \neq t_\beta^r$. In addition, on-site energy in rotating frame ϵ'_α is also varied at experimentally probed ω_c . Therefore, chiral currents at the edges of our three-leg ladder (s, d orbitals) show

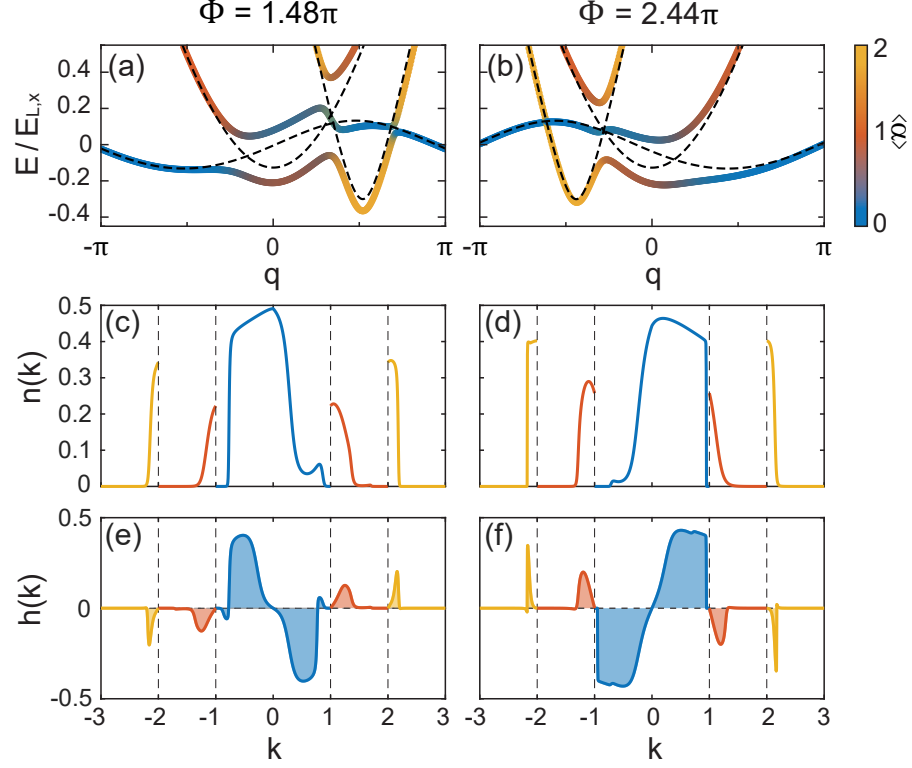


Figure 5.4: Energy structures of the ladder system calculated from Eq. 5.11 for (a) $\Phi = 1.48\pi$ and $t_0^s/t_0^r = 3.4$, and (b) $\Phi = 2.44\pi$ and $t_0^s/t_0^r = 2.6$. The color indicates the mean orbital value, $\langle\alpha\rangle$. The dashed lines show the bare band structures for zero inter-leg coupling. (c, d) Momentum distribution $n(k)$ and asymmetry function $h(k) = n(k) - n(-k)$ calculated for the orbital-mixed ground bands in (a) and (b). The signs of the J_α 's are consistent with the experimental data. In the calculation of $n(k)$, the initial momentum distribution of the s band is set to be the same as the averaged lattice momentum distribution of the sample prepared in the optical lattice without the Raman coupling beams in the experiment.

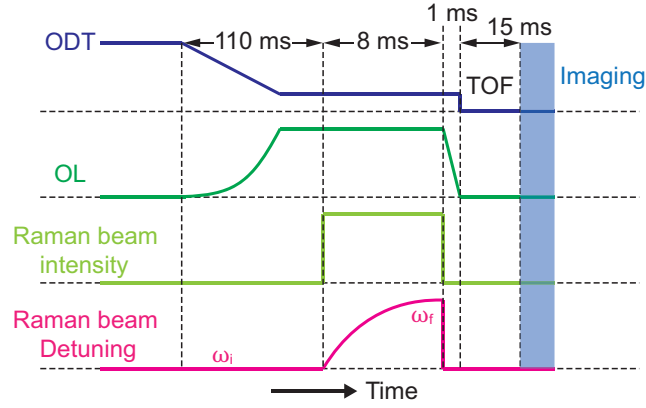


Figure 5.5: Experimental sequence for adiabatic loading and imaging of the synthetic ladder system. The temporal control of the optical dipole trap (ODT), the optical lattice (OL), and the Raman beam intensity and detuning are displayed. The time is not shown in absolute scale.

asymmetric amplitude, and bulk states (p orbital) show non-vanishing current, in contrast to the symmetric Hall ladder system.

To probe the chirality of the ladder system, we load fermions in the orbital-mixed ground band and measure the momentum distributions of the orbitals. Fig. 5.5 shows schematic of experimental sequence for adiabatic loading. First, we turn on the Raman beams at the off-resonant frequency $\omega = \omega_c - 2\pi \times 6$ kHz and ramp ω to the target value ω_c over 8 ms. The ramp time is limited by the scattering atom loss from the Raman beams, and in our loading process, the total atom number is reduced by 40%. The momentum distributions of the orbitals are measured using an adiabatic band-mapping technique [76]. After suddenly turning off the Raman beams, we linearly ramp down the lattice potential to zero within 1 ms and subsequently, take an absorption image of the atoms after a time-of-flight of 15 ms.

Figure 5.6 shows typical absorption image after band mapping and TOF.

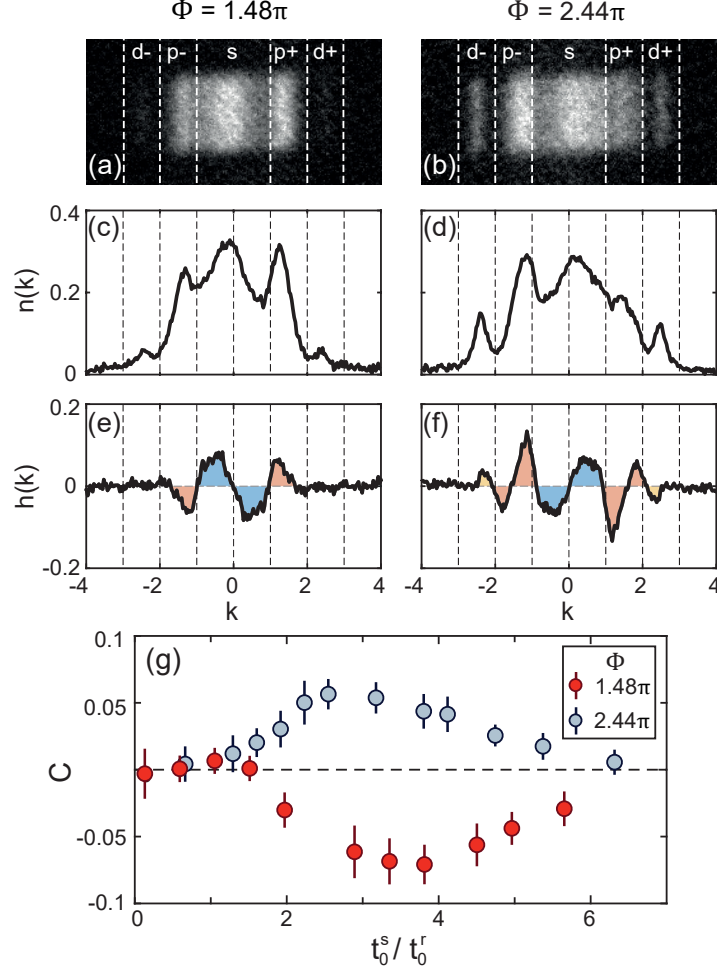


Figure 5.6: Chiral currents in the fermionic three-leg ladder. Band-mapped images of the samples adiabatically loaded into the ground band for (a) $\Phi = 1.48\pi$ and $t_0^s/t_0^r = 3.4$, and (b) 2.44π and $t_0^s/t_0^r = 3.4$, respectively. (c, d) Corresponding 1D momentum distributions $n(k)$ obtained by integrating the images along the y direction. k is normalized by k_L . (e, f) Asymmetry function $h(k) = n(k) - n(-k)$, demonstrating the chiral currents of the orbitals. (g) Evolution of $\mathcal{C} = J_0 - J_1$, where $J_\alpha = \int_{-\alpha}^{\alpha+1} h(k) dk$, as a function of t_0^s/t_0^r for $\Phi = 1.48\pi$ (red) and 2.44π (blue). Each data point was obtained by averaging twenty measurements from the same experiment, with the error bar indicating the standard deviation of the measurements.

Integrating the measured 2D momentum distribution along the y direction, we obtain the 1D distribution $n(k)$ normalized as $\int n(k)dk = 1$ [Figs. 5.6(c) and (d)]. The chiral currents of the system are clearly observed from the asymmetric momentum distributions of the orbitals. The momentum asymmetry of the α band is quantified with $J_\alpha = \int_\alpha^{\alpha+1} h(k)dk$ [Figs. 5.6(e) and (f)] [96, 100]. Our measurements show $\{J_0, J_1, J_2\} = \{-0.049, 0.020, 0.002\}$ for $\Phi = 1.48\pi$ and $t_0^s = 3.3t_0^r$, and $\{J_0, J_1, J_2\} = \{0.037, -0.019, -0.008\}$ for $\Phi = 2.44\pi$ and $t_0^s = 3.5t_0^r$. The signs of the J_α 's are consistent with the theoretical expectations shown in Figs. 5.4 (c) and (d). It is noticeable that the d -band populations are quite different in the two cases although the band structures are almost mirror-symmetric to each other. This difference originates from the different adiabaticity of the loading process due to the q dependence of the inter-orbital coupling strengths. In Fig. 5.6(g), we display the evolution of $\mathcal{C} = J_0 - J_1$ as a function of the relative inter-leg coupling, t_0^s/t_0^r . $|\mathcal{C}|$ initially increases as t_0^s/t_0^r increases, which is attributed to the gap opening, and reaches a maximum at $t_0^s/t_0^r \sim 4$ before decreasing to zero for large t_0^s/t_0^r . In the limit of $t_0^s/t_0^r \rightarrow \infty$, the orbital states become fully mixed to suppress the chirality of the system [101, 109]. A similar behavior was observed in a previous experiment with a symmetric three-leg ladder system [96].

5.5 Quench dynamics in cross-linked chiral ladder

Next, we investigate the quench dynamics of the ladder system to demonstrate the effect of the cross links, wherein fermions are initially prepared in the s -

orbital leg and the Raman beams are suddenly turned on at $\omega = \omega_c$. The sudden change of Ω_α will lead to a so-called skipping cyclotron motion along the ladder edge [96], which provides direct evidence of quantum Hall effect. The time evolution of the total momentum asymmetry $J_{\text{tot}} = \sum_\alpha J_\alpha$ and the p -band population n_p are shown in Figs. 5.7(c) and (d). The in-phase oscillations for J_{tot} and n_p are consistent with the skipping motion expected under a magnetic flux in the synthetic ladder.

Recalling that the inter-orbital coupling strength is modulated as $\hbar\Omega_\alpha(q) = t_\alpha^s - 2t_\alpha^d \cos(q + \alpha\varphi - \varphi'_\alpha)$, we expect that the cross-link effect can be directly revealed by a momentum-resolving analysis of the quench dynamics. We examine two cases, $\Phi = 2.44\pi$ and 0.52π , which show almost the same effective magnetic flux $\sim \pi/2$ in a modulus of 2π but different modulation phases of $\Omega_0(q)$ with $\varphi'_0 = -0.5\pi$ and 0.75π , respectively [Figs. 5.7(a) and (b)]. In the case of $\Phi = 2.44\pi$ (0.52π), the average coupling strength for $q > 0$, $\langle\Omega_0\rangle_+$, is stronger (weaker) than that for $q < 0$, $\langle\Omega_0\rangle_-$, so the p band population with positive momentum will show faster (slower) oscillations than that with negative momentum. Here, the case of $\Phi = 0.52\pi$ is generated by reversing the Raman beam directions from those for $\Phi = 1.48\pi$, i.e., $k_R \rightarrow -k_R$.

The corresponding time evolution of the p band populations with positive and negative momenta, $n_{p\pm}(t) = \int_{\pm 1}^{\pm 2} n(k, t) dk$ are shown in figure 5.7(e) and (f). We observe that n_{p+} oscillates faster (slower) than n_{p-} for $\Phi = 2.44\pi$ ($\Phi = 0.52\pi$), which is in agreement with that expected from the momentum dependence of $\Omega_0(q)$. The oscillation time difference is characterized by $\eta = \tau_{p-}/\tau_{p+}$, where $\tau_{p\pm}$ is the time at which the first oscillation minimum occurs in $n_{p\pm}(t)$, with our measurements giving $\eta = 1.92$ and 0.81 for $\Phi = 2.44\pi$ and 0.52π , respectively. We find that our results are quantitatively well accounted for

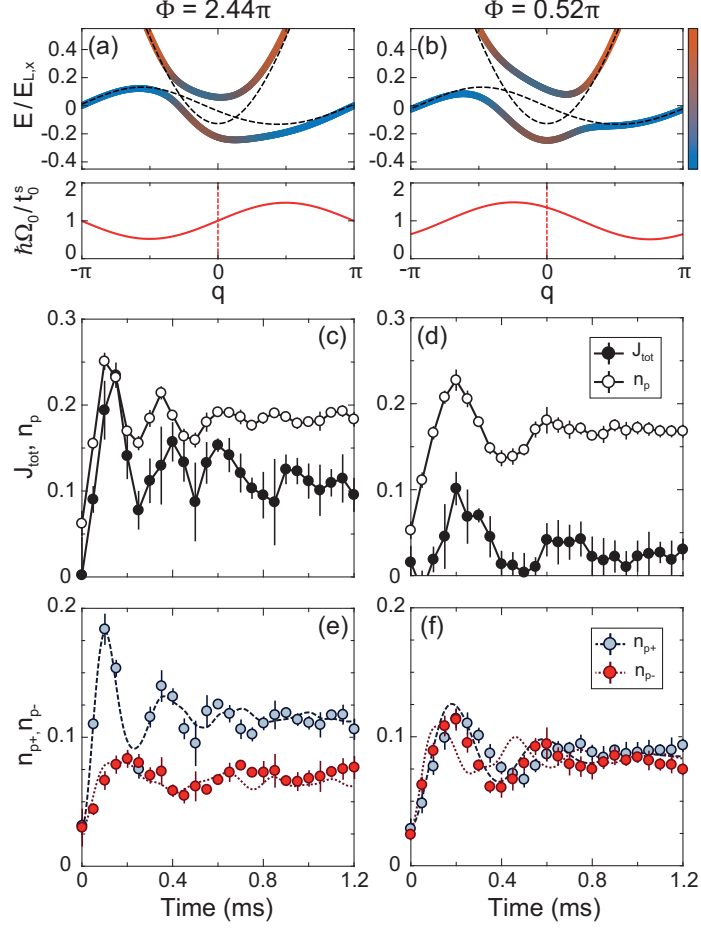


Figure 5.7: Quench dynamics of the ladder system and effects of the complex cross links. Energy band structures of the s - p , two-leg ladder and the inter-leg coupling strength $\hbar\Omega_0(q)/t_0^s$ (red solid) for (a) $\Phi = 2.44\pi$ and (b) $\Phi = 0.52\pi$. Here, $t_0^s/t_0^r = 4$ for both cases to clearly show the effect of the momentum dependence of $\Omega_0(q)$. Quench dynamics is initiated by suddenly turning on the inter-leg coupling to the systems where atoms are initially prepared in the s band. Time evolutions of the total momentum asymmetry $J_{\text{tot}} = J_0 + J_1 + J_2$ and the p -band fractional population n_p for (c) $\Phi = 2.44\pi$ and $t_0^s/t_0^r = 11.3$, and (d) $\Phi = 0.52\pi$ and $t_0^s/t_0^r = 8.5$. (e, f) Corresponding time evolutions of $n_{p\pm} = \int_{\pm 1}^{\pm 2} n(k, t) dk$. The different oscillation periods for $n_{p\pm}$ reflect the modulations of $\Omega_0(q)$, which originate from the complex cross links of the ladder. Each data point is the average of seven measurements, with the error bar showing the standard deviation of the measurements. Dashed lines plotted in (e),(f) are the numerical results with (e) $t_0^s/t_0^r = 11.3$, and (f) $t_0^s/t_0^r = 8.5$.

by the average coupling strength ratio $\langle\Omega_0\rangle_+/\langle\Omega_0\rangle_- = (\pi t_0^s - 4t_0^d \sin \varphi'_0)/(\pi t_0^s + 4t_0^d \sin \varphi'_0) = 1.9$ and 0.7 for $\Phi = 2.44\pi$ and 0.52π , respectively. We also observe that the numerical simulations based on equation 5.11 show reasonable agreement with the experimental data.

5.6 Topological phase transition

In this section, we discuss the topological phase transition of the cross-linked chiral ladder system, which is anticipated to occur with an increasing cross-link strength. The three-leg ladder model described by $H(q; \Phi)$ in Eq. 5.11 constitutes an 1D three-band system and its topological property can be characterized by the Zak phases of the bands [91]. The Zak phase is defined by

$$\gamma_Z = i \int_{BZ} \langle u_q^n | \partial_q | u_q^n \rangle dq, \quad (5.12)$$

where u_q^n is the cell-periodic Bloch function of the n -th band and by numerically calculating γ_Z of, e.g., the orbital-mixed ground band, we may investigate on the condition for the three-leg ladder system to have a topologically non-trivial phase. In a two-band model such as the Creutz ladder model [92], it can be easily understood that a topologically non-trivial band with $\gamma_Z \neq 0$ will appear when the inter-band coupling amplitude changes its sign at the two distinct band crossing points because it means that the spin texture of the mixed band has a full winding in the pseudo-spin space composed by the two band states. In a similar manner, we expect that the topological property of the three-leg ladder system would be determined by the sign changes of two coupling amplitudes $\Omega_0(q)$ and $\Omega_1(q)$, and their relative positions to the band crossing points which are determined by φ and φ'_α .

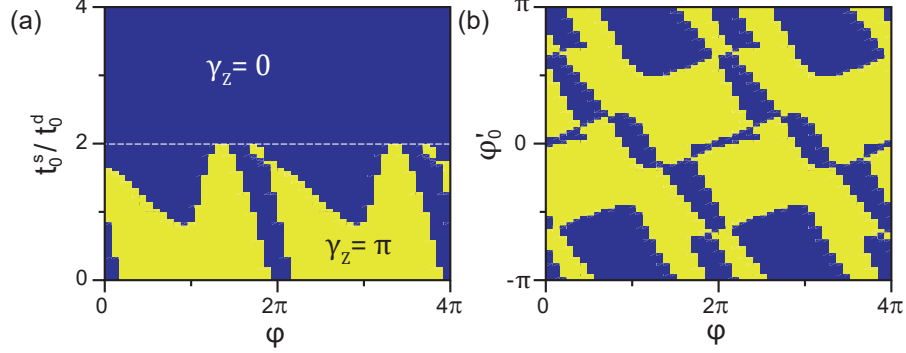


Figure 5.8: Zak phase γ_Z of the ground band of the three-leg ladder system (a) in the plane of φ and t_0^s/t_0^d for $\{t_1^s/t_1^d, \varphi'_0, \varphi'_1\} = \{1.7, -\pi/2, \pi/2\}$, and (b) in the plane of φ and φ'_0 for $\{t_0^s/t_0^d, t_1^s/t_1^d, \varphi'_1\} = \{1, 1.7, \pi/2\}$. The yellow regions indicate the topological regimes with $\gamma_Z = \pi$. The white dashed line in (a) indicates the line with $t_0^s/t_0^d = 2$. In the experimental condition for $\Phi = 1.44\pi$ ($\varphi = 0.44\pi$), $\{t_0^s/t_0^d, t_1^s/t_1^d, \varphi'_0, \varphi'_1\} = \{4.2, 1.5, -0.75\pi, 0.24\pi\}$.

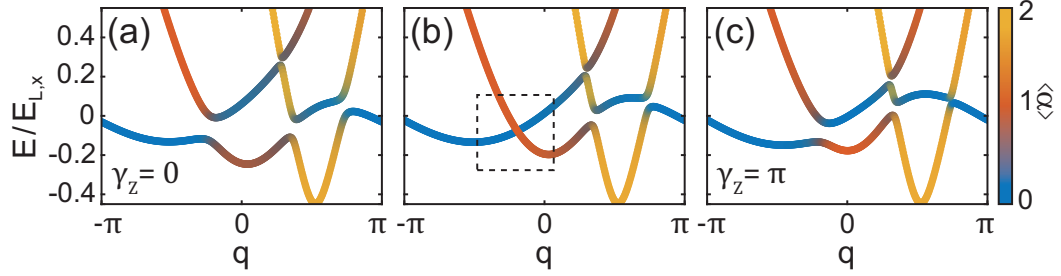


Figure 5.9: Topological phase transition of the three-leg ladder system. Band dispersion of the system for (a) $t_0^s/t_0^d = 2.5$, (b) 1.15, and (c) 0 with $\{k_R/k_L, t_0^d/t_0^r, t_1^s/t_0^r, t_1^d/t_0^r, \varphi'_0, \varphi'_1\} = \{0.24, 1.5, 6.1, 3.6, -\pi/2, \pi/2\}$. The Zak phase of the ground band changes from $\gamma_Z = 0$ in (a) to $\gamma_Z = \pi$ in (c). The topological phase transition is featured with a gap closing in the boxed region in (b).

We calculated the Zak phase γ_Z of the orbital-mixed ground band over the parameter space of our ladder system and identify multiple regions of topologically nontrivial phases with $\gamma_Z \neq 0$ for $t_0^s/t_0^d < 2$. Some of the calculation results for a parameter region close to our experimental condition are displayed in figure 5.8. We find that a topological phase with $\gamma_Z \neq 0$ can emerge in the system for the variations of the complex cross-link amplitudes. In particular, we observe that the topologically non-trivial phase exists only in the regions with $t_\alpha^s/t_\alpha^d < 2$. This is consistent with our anticipation from the relation of $\hbar\Omega_\alpha(q) = t_\alpha^s - 2t_\alpha^d \cos(q + \alpha\varphi - \varphi'_\alpha)$, where the inter-band coupling amplitude changes its sign in a certain range of q for $t_\alpha^s/t_\alpha^d < 2$. Band gap closing occurs at the boundary of Zak phase, which is direct property of topological phase transition as shown in figure 5.9. One additional observation is that the Zak phase also depends on φ and φ'_0 even for fixed $t_\alpha^s/t_\alpha^d < 2$. It would be interesting to clarify the geometric meaning of having nonzero γ_z in terms of the sign change of Ω_α and the band crossing points in the pseudo-spin-1 system.

5.7 Conclusion

In conclusion, we realized a cross-linked chiral fermionic ladder based on the orbital states of a 1D optical lattice. The chiral edge currents were observed and the cross-link effect was demonstrated by the momentum dependence of the inter-orbital coupling strengths. The orbital-based synthetic ladder system shows an explicitly broken leg symmetry with $t_\alpha^r \neq t_\beta^r$, providing an interesting opportunity for studying topological phases that are protected by unconventional symmetries [99, 110]. As a means of controlling the strength and phase of the complex cross link, tailoring the orbital wave functions by engineering lattice

potential is conceivable [111]. Our orbital-momentum coupling scheme can be extended to multiple hyperfine spin states, which would allow for interactions between fermions [112].

Chapter 6

Topological ladder in resonantly driven optical lattice

This chapter describes experimental realization of a Creutz ladder for ultracold fermionic atoms in a resonantly driven 1D optical lattice. The two-leg ladder consists of the two lowest orbital states of the optical lattice and the cross inter-leg links are generated via two-photon resonant coupling between the orbitals by periodic lattice shaking. The characteristic pseudo-spin winding structure in the energy bands of the ladder system is demonstrated using momentum-resolved Ramsey-type interferometric measurements. The experimental results are published in the following paper.

- J. H. Kang, J. H. Han, and Y. Shin, “*Creutz ladder in a resonantly shaken 1D optical lattice,*” New Journal of Physics **22**, 013023 (2020).

6.1 Introduction

Topological phases such as quantum Hall states and topological insulators represent intriguing physics beyond the conventional Landau paradigm of phase transition [98, 113]. Motivated further by their novel transport properties, the study of topological phases constitutes one of the frontiers in modern condensed matter physics. Ultracold atoms in optical lattices, featuring tunneling amplitude engineering and tunable interaction strength, provide a unique platform for realizing and exploring such exotic topological states [48, 114]. Along with the steady development of experimental techniques, many topological model systems have been recently realized, which include the Harper–Hofstadter Hamiltonian in 2D rectangular lattices [61, 62], the Haldane model in a 2D hexagonal lattice [66], and various Hall and topological ladder systems based on additional synthetic dimensions such as internal atomic states [96, 97, 99, 100, 115, 116] and lattice orbital states [117].

Periodic lattice shaking is one of the successful tools for exploring exotic phases in optical lattices. Under periodic modulations of the lattice potential, the system parameters such as tunneling magnitude [23, 86] and phase [87] can be coherently manipulated, giving rise to a hopping configuration that is difficult to realize with static schemes. An outstanding example is the Haldane model realized by circularly shaking a 2D hexagonal optical lattice potential to achieve complex next-nearest-neighbor hopping [66, 68]. From the perspective of Floquet band engineering, the lattice shaking method has been extensively discussed even in the resonant regime where the driving frequency is high enough to match the energy gap between two bands [118]. Such strong orbital hybridization may enable access to a broader range of effective Hamiltonians [119, 120]. In

particular, it was anticipated that multi-photon inter-orbital resonant coupling could yield a special route to engineer topological states [105, 121]. Thus, it is highly desirable to examine the multifarious scope of Floquet band engineering for the study of topological phases.

In this paper, we experimentally investigate the effects of two-photon inter-orbital resonant coupling in a periodically driven 1D optical lattice, and demonstrate the realization of a generalized Creutz ladder for ultracold fermionic atoms in the shaken lattice system. The Creutz ladder is a cross-linked two-leg ladder system under a magnetic field, which has been discussed as a minimal model for 1D topological insulators [92, 122, 123]. Recently, it was extended to an interacting case, referred to as the Creutz-Hubbard model, for the study of correlated topological phases [102, 104, 124–126]. In our experiment, the two-leg ladder is formed by the two lowest orbital states in optical lattice, and the cross inter-leg links are generated via the two-photon resonant coupling between the orbitals by lattice shaking. Using momentum-resolved Ramsey-type interferometric measurements, we demonstrate the characteristic pseudo-spin winding structure in the energy bands of the Creutz ladder. We also discuss the extension of the inter-leg link control with two-frequency driving, where the direct links are additionally controlled by the one-photon resonant coupling between the orbitals. Finally, based on the extended inter-leg link control, we propose an experimental scheme for topological charge pumping in the generalized Creutz ladder system.

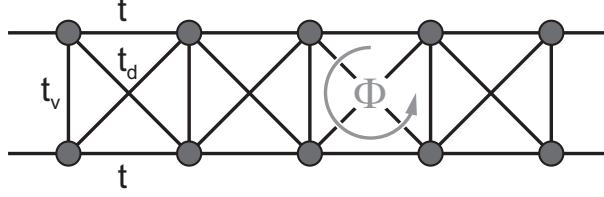


Figure 6.1: Creutz ladder model. A two-leg ladder system under a magnetic field. t denotes the intra-leg hopping amplitude and Φ is the gauge flux per plaquette. t_v and t_d indicate the inter-leg hopping amplitudes in the ladder along the vertical rungs and the diagonal links, respectively.

6.2 Creutz ladder

The Creutz model describes a spinless fermion system in a two-leg ladder under a magnetic field [92]. The two-leg ladder system is sketched in figure 6.1, where t denotes the hopping amplitude along the legs, t_v along the rungs of the ladder, t_d along the diagonal links, and Φ is the gauge flux penetrating each ladder plaquette. The system's Hamiltonian is given by

$$H_{\text{CL}} = \sum_j \left[\left\{ \Psi_j^\dagger (t e^{-i(\Phi/2)\sigma_z} + t_d \sigma_x) \Psi_{j+1} + \text{H.c.} \right\} + \Psi_j^\dagger (t_v \sigma_x) \Psi_j \right], \quad (6.1)$$

where $\Psi_j = (c_{j,1}, c_{j,2})^T$ with $c_{j,l}$ being the annihilation operator of the fermion at site j and leg $l \in \{1, 2\}$, and $\boldsymbol{\sigma} = \{\sigma_x, \sigma_y, \sigma_z\}$ are the Pauli matrices. The corresponding Bloch Hamiltonian is expressed as

$$\begin{aligned} H_{\text{CL},q} &= 2t \cos(\Phi/2) \cos(q) \mathbb{I} + [t_v + 2t_d \cos(q)] \sigma_x + 2t \sin(\Phi/2) \sin(q) \sigma_z \\ &= 2t \cos(\Phi/2) \cos(q) \mathbb{I} + \mathbf{h}_{\text{CL}}(q) \cdot \boldsymbol{\sigma}, \end{aligned} \quad (6.2)$$

where q is the quasimomentum, \mathbb{I} is the identity matrix, and $\mathbf{h}_{\text{CL}}(q) = \{t_v + 2t_d \cos(q), 0, 2t \sin(\Phi/2) \sin(q)\}$. Because the vector \mathbf{h}_{CL} is confined in the xz plane, its winding around the origin for the whole Brillouin zone (BZ), $-\pi <$

$q \leq \pi$, characterizes the topology of the ladder system. A topologically non-trivial state occurs when $|t_v/t_d| < 2$, where $\mathbf{h}_{\text{CL}}(q)$ fully encircles the origin, giving a non-zero integer winding number representing the topological character of the system. The band dispersion of the system is given by $E_{\pm}(q) = 2t \cos(\Phi/2) \cos(q) \pm |\mathbf{h}_{\text{CL}}(q)|$. It is remarkable that with $\Phi = \pi$, $t_v = 0$ and $t_d = t$, the ladder system has $E_{\pm}(q) = \pm 2|t|$, constituting a 1D topological system with two flat bands.

The original Creutz model was proposed for a special case of $\Phi = \pm\pi$, where the ladder system holds chiral symmetry for $\sigma_y H_{\text{CL},q} \sigma_y = -H_{\text{CL},q}$ [92], and it is equivalent to the Su-Schrieffer-Heeger model, which belongs to the BDI class of the Altland-Zirnbauer classification [101, 102]. In an extended case of $\Phi \neq \pm\pi$, the chiral symmetry is broken, but since \mathbf{h}_{CL} remains in the xz plane, the topological character of the system is still unambiguously represented by the winding number of \mathbf{h}_{CL} . It was discussed that the topological phase of the extended Creutz model is protected by a hidden inversion symmetry [127, 128].

6.3 Atom in a resonantly shaken optical lattice

We consider an atom in a 1D optical lattice potential $V(x) = \frac{V_L}{2} \cos[\frac{2\pi}{a}(x - x_0)]$, where the position x_0 of the lattice potential is periodically driven as $x_0(t) = -d \cos(\omega t + \varphi)$ [figure 6.2(a)]. Here, V_L is the lattice depth and a is the lattice spacing. In the comoving reference frame with the vibrating optical lattice, the Hamiltonian of the system is given by $H = H_{\text{stat}} + \delta H$ with

$$\begin{aligned} H_{\text{stat}} &= \frac{p_x^2}{2m} + \frac{V_L}{2} \cos\left(\frac{2\pi}{a}x\right), \\ \delta H &= -d\omega \sin(\omega t + \varphi) p_x, \end{aligned} \tag{6.3}$$

where H_{stat} is the Hamiltonian of the stationary optical lattice system with p_x being the atom's momentum and m being the atomic mass, and δH represents the perturbation from the inertial force induced by the lattice shaking, which can make mixing between the energy bands of the stationary lattice system. In this work, we are interested in the situation where the lattice shaking frequency ω is close to the resonance frequency for the coupling between the two lowest, s and p bands of the lattice potential [figure 6.2(b)]. From a synthetic dimension perspective [95], the 1D shaken lattice system can be regarded as a two-leg ladder system constituted by the s and p orbitals, where the inter-orbital coupling by lattice shaking is depicted as the inter-leg links between the two legs.

In a two-band tight-binding approximation, the Hamiltonian of the driven lattice system is expressed as

$$H = \sum_j \Psi_j^\dagger K(t) \Psi_j - \sum_j [\Psi_j^\dagger J(t) \Psi_{j+1} + \text{H.c.}], \quad (6.4)$$

where $\Psi_j = (c_{j,p}, c_{j,s})^T$, $c_{j,\alpha}$ is the annihilation operator for the atom in the Wannier state $|j, \alpha\rangle$ on lattice site j in orbital $\alpha \in \{s, p\}$. The matrices $K(t)$ and $J(t)$ are given by

$$\begin{aligned} K(t) &= \begin{pmatrix} \epsilon_p & -ih_0^{sp} \sin(\omega t + \varphi) \\ ih_0^{sp} \sin(\omega t + \varphi) & \epsilon_s \end{pmatrix} \\ J(t) &= \begin{pmatrix} t_p - ih_1^{pp} \sin(\omega t + \varphi) & ih_1^{sp} \sin(\omega t + \varphi) \\ -ih_1^{sp} \sin(\omega t + \varphi) & t_s - ih_1^{ss} \sin(\omega t + \varphi) \end{pmatrix}, \end{aligned} \quad (6.5)$$

where $\epsilon_\alpha = \langle j, \alpha | H_{\text{stat}} | j, \alpha \rangle$ and $t_\alpha = -\langle j, \alpha | H_{\text{stat}} | j + 1, \alpha \rangle$ are the on-site energy and nearest-neighbor hopping amplitude of the α orbital, respectively, and $h_\ell^{\alpha\beta} = \hbar\omega d \langle j, \alpha | (\partial/\partial x) | j + \ell, \beta \rangle$ is the transition element between the α and β orbitals separated by ℓ lattice sites.

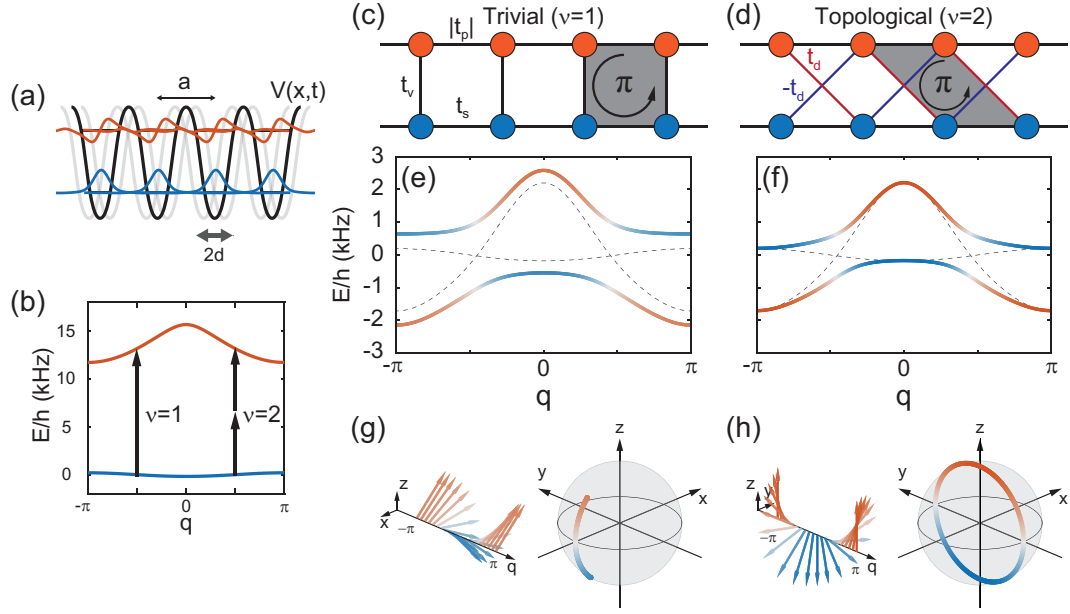


Figure 6.2: Creutz ladder in a resonantly shaken optical lattice. (a) Schematic of the periodically driven 1D lattice system. The position of the lattice potential is sinusoidally modulated with frequency ω and amplitude d . The lattice spacing is denoted by a . (b) The s and p orbitals can be resonantly coupled via one-photon ($\nu=1$) or two-photon ($\nu=2$) processes. Two-leg ladder diagrams for the systems with (c) the $\nu=1$ and (d) $\nu=2$ resonant couplings. Band structures of the ladder systems for our experimental conditions with (e) $\{\omega/2\pi, d/a\} = \{13.4 \text{ kHz}, 0.05\}$ and (f) $\{6.7 \text{ kHz}, 0.2\}$, giving $t_v/\hbar = 1.0 \text{ kHz}$ ($\nu = 1$) and $t_d/\hbar = 0.4 \text{ kHz}$ ($\nu = 2$), respectively. The blue and red colors indicate the orbital composition of the energy band, corresponding to s and p , respectively. The dashed lines show the bare dispersion curves of the s and p bands for $\{t_s, t_p\}/\hbar = \{0.1, -1.0\} \text{ kHz}$. (g), (h) Corresponding pseudo-spin distributions of the ground bands and their trajectories on the Bloch sphere.

When the shaking frequency ω is close to ω_{sp}^0/ν with integer ν , where $\omega_{sp}^0 = \epsilon_{sp}/\hbar$ and $\epsilon_{sp} = \epsilon_p - \epsilon_s$, a resonant inter-orbital coupling would be generated via ν -photon transition process. To explicate the properties of the inter-orbital couplings generated by the one-photon ($\nu = 1$) and two-photon ($\nu = 2$) resonant processes, we calculate the effective Hamiltonian $H_{\text{eff}}^{(\nu)}$ of the system in a rotating frame with frequency $\nu\omega$, using a high-frequency expansion method [79,81,85]. The effective Hamiltonian is obtained as $H_{\text{eff}}^{(\nu)} = H_0^{(\nu)} + H_C^{(\nu)}$ with

$$\begin{aligned} H_0^{(\nu)} &= \sum_j \left\{ \Psi_j^\dagger (\Delta_\nu \sigma_z) \Psi_j - \left[\Psi_j^\dagger (\bar{t}_r \mathbb{I} + t_r \sigma_z) \Psi_{j+1} + \text{H.c.} \right] \right\} \\ H_C^{(1)} &= \sum_j \Psi_j^\dagger \left(\frac{h_0^{sp}}{2} R_{\hat{\mathbf{z}}}(\varphi) \sigma_x \right) \Psi_j \\ H_C^{(2)} &= \sum_j \left[\Psi_j^\dagger \left(\frac{h_0^{sp} h_1}{2\hbar\omega} R_{\hat{\mathbf{z}}}(2\varphi) i\sigma_y \right) \Psi_{j+1} + \text{H.c.} \right]. \end{aligned} \quad (6.6)$$

where $\Delta_\nu = \hbar(\omega_{sp}^0 - \nu\omega)/2$, $\bar{t}_r = \frac{t_p + t_s}{2}$, $t_r = \frac{t_p - t_s}{2}$, $R_{\hat{\mathbf{n}}}(\eta) = \exp(-i\eta\hat{\mathbf{n}} \cdot \boldsymbol{\sigma})$ with $\hat{\mathbf{n}} = \mathbf{n}/|\mathbf{n}|$, and $h_1 = h_1^{pp} - h_1^{ss}$. $H_0^{(\nu)}$ represents an uncoupled two-leg ladder with energy imbalance Δ_ν and intra-leg hopping, and $H_C^{(\nu)}$ describes the dominant inter-leg coupling generated by the ν -photon resonant process.

The character of the inter-leg coupling given by $H_C^{(\nu)}$ is different for the two cases, $\nu = 1$ and $\nu = 2$. $H_C^{(1)}$ describes the on-site orbital-changing transitions, corresponding to the direct inter-leg links with amplitude $t_v = h_0^{sp}/2$ in the ladder system. On the other hand, $H_C^{(2)}$ describes the second-order processes consisting of on-site orbital changing and nearest-neighbor hopping along the leg direction, giving the diagonal inter-leg links with amplitude $t_d = h_0^{sp} h_1 / 2\hbar\omega$. The difference of $H_C^{(1)}$ and $H_C^{(2)}$ can be understood from parity conservation; since the lattice shaking is an odd-parity operation, the two-photon on-site

transition is forbidden between the s and p orbitals, which have opposite parities [105]. In figures 6.2(c) and (d), we present the schematic diagrams of the resulting ladder systems for $\nu = 1$ and 2, respectively. Note that the sign of t_p is opposite to that of t_s , and under a proper transformation, the ladder systems can be viewed as having a π gauge flux piercing each ladder plaquette.

The Bloch Hamiltonian of the two-leg ladder system is expressed as $H_q^{(\nu)} = -2\bar{t}_r \cos(q)\mathbb{I} + \mathbf{h}_\nu(q) \cdot \boldsymbol{\sigma}$, where q is expressed in units of a^{-1} and the $\mathbf{h}_\nu(q)$ is given by

$$\begin{aligned}\mathbf{h}_1(q) &= t_v \hat{\boldsymbol{\rho}}_1 + [\Delta_1 - 2t_r \cos(q)] \hat{\mathbf{z}} \\ \mathbf{h}_2(q) &= 2t_d \sin(q) \hat{\boldsymbol{\rho}}_2 + [\Delta_2 - 2t_r \cos(q)] \hat{\mathbf{z}}\end{aligned}\tag{6.7}$$

with $\hat{\boldsymbol{\rho}}_1 = \cos(\varphi)\hat{\mathbf{x}} + \sin(\varphi)\hat{\mathbf{y}}$ and $\hat{\boldsymbol{\rho}}_2 = -\sin(2\varphi)\hat{\mathbf{x}} + \cos(2\varphi)\hat{\mathbf{y}}$. Under a transformation of $\hat{\boldsymbol{\rho}}_\nu \rightarrow \hat{\mathbf{x}}$ and $q \rightarrow q - \frac{\pi}{2}$, the functional form of $H_q^{(\nu)}$ on q becomes same as that of $H_{\text{CL},q}$ except the term of $\Delta_\nu \hat{\mathbf{z}}$ in \mathbf{h}_ν . Regardless of having the additional term, \mathbf{h}_ν is confined in the plane defined by $\hat{\boldsymbol{\rho}}_\nu$ and $\hat{\mathbf{z}}$, and thus, its winding number determines the topological characteristic of the ladder system. From equation 6.6, it is obvious that $\mathbf{h}_1(q)$ cannot encircle the origin, whereas $\mathbf{h}_2(q)$ can give winding number of ± 1 when $|\Delta_2| < 2|t_r|$. This means that a topologically non-trivial phase would emerge in the shaken lattice system with two-photon resonant coupling ($\Delta_2 \approx 0$). The chiral symmetry is generally broken in $H_q^{(2)}$ due to $\bar{t}_r \neq 0$, and it was argued that the topologically non-trivial phase is protected by symmetry composed of time-reversal and mirror symmetries [99]. It is interesting to note that one of the topological bands becomes dispersionless when $|\Delta_2| = 2|\bar{t}_r|$ and $t_d^2 = |t_s t_p|$.

In figures 6.2(e) and (f), we display the band structures of the two-leg ladder system with one-photon resonant coupling ($\Delta_1 = 0$) and two-photon

resonant coupling ($\Delta_2 = 0$), respectively. The pseudo-spin distributions of the ground bands over the BZ and their corresponding trajectories on the Bloch sphere are also shown in figures 6.2(g) and (h). In the $\nu = 2$ case, the pseudo-spin trajectory make a great circle on the Bloch sphere, which is the key topological feature of the constructed Creutz ladder system. In the following section, we present our experimental investigation, where the focus is to demonstrate the winding structure of $\mathbf{h}_2(q)$ in the resonantly shaken lattice system.

6.4 Experiment and result

6.4.1 Experimental setup

Our experiment starts with preparing a spin-balanced degenerate Fermi gas of ^{173}Yb atoms in the $F = 5/2$ hyperfine ground state, which has all the six spin components equally, in an optical dipole trap [70]. The total atom number is $\approx 1.5 \times 10^5$, and the temperature is $\approx 0.35T_F$, where T_F is the Fermi temperature of the trapped sample. The atoms are adiabatically loaded in a 1D optical lattice potential, which is formed along the x -direction by interfering two laser beams with a wavelength of $\lambda_L = 532$ nm. The lattice spacing and depth are $a = \sqrt{3}\lambda_L/2$ and $V_L = 8E_r$, respectively, where $E_r = \hbar^2/8ma^2 = h \times 3.1$ kHz (h is the Planck constant). The trapping frequencies of the overall harmonic potential were estimated to be $(\omega_x, \omega_y, \omega_z) \approx 2\pi \times (41, 61, 130)$ Hz. After loading the atoms in the lattice potential, the fractional population of the p orbital was about 3%. Shaking of the lattice potential is implemented by sinusoidally modulating the frequency difference $\delta\omega_L$ between the two lattice laser beams as $\delta\omega_L(t) = A \sin(\omega t + \varphi)$, which results in lattice site vibrations with amplitude

$$d = \frac{A}{2\pi\omega} a \text{ [figure 2(a)]}.$$

6.4.2 Shaking spectroscopy

We first investigate the resonance condition for inter-orbital coupling by measuring the momentum distribution $n(k)$ of the atoms as a function of the driving frequency ω . After preparing the atoms in the s band of the static lattice, we suddenly apply the periodic driving over 20 cycles, which is longer than the dephasing time of the system, and we measure $n(k)$ by taking an absorption image of the atoms after a band mapping protocol [75] and a subsequent time of flight. In the band mapping, quasimomentum states are transformed onto the corresponding real momentum states in free space by slowly ramping down the lattice potential, and $n(k)$ shows the quasimomentum distribution of the atoms in the s band for $|k| < \pi$ with $k = q$ and that in the p band for $\pi < |k| < 2\pi$ with $k = q - \text{sgn}(q) \times (2\pi)$, where k is expressed in units of a^{-1} .

In figure 6.3, we display the measurement result of the momentum distribution change, $\Delta n(k)$, from that of the non-driven sample as a function of ω . Here $n(k)$ is normalized as $\int n(k)dk = 1$. A strong spectral signal is observed in the range $\omega/2\pi = 11 \sim 17$ kHz [figure 6.3(a)]. The spectral peak position follows the one-photon resonance condition $\omega = \omega_{sp}(q) \approx [\epsilon_{sp} - 4t_r \cos(q)]/\hbar$, where $\{\epsilon_{sp}, t_r\}/\hbar = \{13.4, -0.54\}$ kHz for our lattice parameters. The two-photon s - p coupling is observed in the corresponding half-frequency range $\omega/2\pi = 5.5 \sim 8$ kHz [figure 6.3(b)], where the spectral structure appears consistent with the resonance condition of $2\omega = \omega_{sp}(q)$. In comparison with the one-photon resonance case in figure 6.3(c), it is noticeable that the signal strength is suppressed at $2\omega \sim \omega_{sp}(0)$ and $2\omega \sim \omega_{sp}(\pm\pi)$, much weaker than that at $2\omega \sim \omega_{sp}(\pm\pi/2)$ [fig-

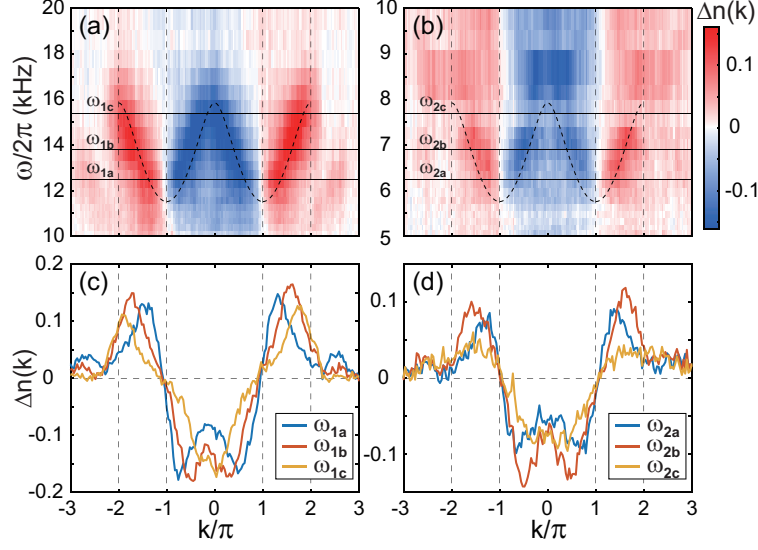


Figure 6.3: Shaking spectroscopy of fermionic atoms in an optical lattice. (a), (b) Spectra of the momentum distribution change $\Delta n(k)$ as a function of the driving frequency ω . The driving amplitude $A/2\pi = 2$ kHz in (a) and 4 kHz in (b). The dashed lines in (a) and (b) indicate the one-photon and two-photon resonance conditions, i.e., $\omega = \omega_{sp}(q)$ and $2\omega = \omega_{sp}(q)$, respectively. (c), (d) Spectral profiles of $\Delta n(k)$ at various ω , indicated by the horizontal lines in (a) and (b).

ure 6.3(d)]. The suppression is consistent with the q -dependence of the transverse field amplitude of \mathbf{h}_2 , $h_{2,\rho}(q) \propto \sin(q)$, which determines the coupling strength between the two orbital-momentum states, $|q, s\rangle$ and $|q, p\rangle$.

In the frequency range of $\omega/2\pi = 11\sim 14$ kHz and $\omega/2\pi \approx 8.5$ kHz, we observe substantial population transfer to the high-momentum region of $|k| > 2\pi$, which result from the two-photon and three-photon couplings between the s and d orbitals, respectively. In the effort to realize an effective two-leg ladder system, coupling to higher orbitals from the s and p orbitals could be detrimental, if its magnitude is not negligible to that of the s - p inter-orbital coupling. In the two-photon resonance condition with $\Delta_2 = 0$, which is of our main interest in this work, the atom loss rate out of the s - p ladder system

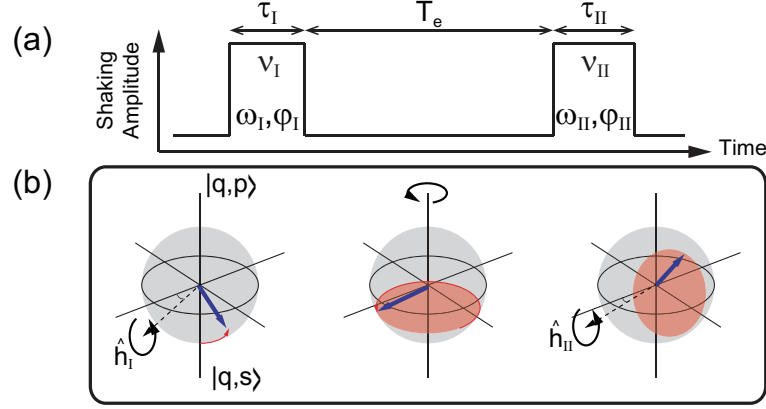


Figure 6.4: Schematic of Ramsey interferometry using two separate pulses of lattice shaking. (a) Schematic of the lattice shaking sequence and (b) the pseudo-spin evolution on the Bloch sphere for the quasimomentum q state. $\hat{h}_{I(II)}$ indicates the direction of \mathbf{h} for the first (second) shaking pulse. The orange disk denotes the precession plane of the pseudo-spin during the intermittent period.

was measured to be $\approx 0.17t_d$ for $A/2\pi = 8$ kHz ($t_d/h = 0.4$ kHz), justifying the effective two-band description of the shaken lattice system. In numerical simulations of an atom in the 1D shaken lattice potential, the atom loss rate due to the higher-band coupling was estimated to be $0.08t_d$, which is less than a half of the experimentally measured value. Further experimental optimization might help reduce the loss rate, such as phase stabilization of the lattice laser beams and transverse confinement of atoms with additional yz lattices beams. It is worth noting that atom-atom interactions, which are present in our spin-balanced sample, can be a source of heating and atom loss in a periodically driven optical lattice system [129].

6.4.3 Ramsey interferometry

In the shaking spectroscopy, the dispersion curve of $\omega_{sp}(q)$ was measured for the two-photon resonant coupling and it confirms the axial component of \mathbf{h}_2 is given by $h_{2,z} = \Delta_2 - 2t_r \cos(q)$. For verifying the winding structure of $\mathbf{h}_2(q)$, therefore, it would be sufficient to demonstrate the asymmetric property of its transverse component, $h_{2,\rho}(-q) = -h_{2,\rho}(q)$.

As a means to probe the asymmetric property of $h_{2,\rho}(q)$, we employ a Ramsey interferometry scheme, where two separate pulses of resonant lattice shaking are applied with a variable time interval T_e . The lattice shaking sequence is described in figure 6.4(a), where the frequency modulations are set as $\delta\omega(t) = A_I \sin(\omega_I t + \varphi_I)$ for the first pulse in $0 < t < \tau_I$ and as $\delta\omega(t) = A_{II} \sin(\omega_{II} t' + \varphi_{II})$ with $t' = t - (\tau_I + T_e)$ for the second pulse in $0 < t' < \tau_{II}$. Here, $\omega_{I(II)} = \omega_{sp}^0 / \nu_{I(II)}$ ($\omega_{sp}^0 / 2\pi = 13.4$ kHz) with $\nu_{I(II)} = 1$ or 2 so that during the first (second) pulse duration, the $\nu_{I(II)}$ -photon resonant coupling is generated in the lattice system. In a rotating frame with frequency $\omega_{sp}^0 = \nu_{I(II)} \omega_{I(II)}$, the effective Bloch Hamiltonian of the resonantly shaken lattice system is given by $H_q(t) = -2\bar{t}_r \cos(q)\mathbb{I} + \mathbf{h}(q, t) \cdot \boldsymbol{\sigma}$ with $\mathbf{h}(q, t) = -2t_r \cos(q)\sigma_z + h_\rho(q, t)[\cos(\theta(t))\sigma_x + \sin(\theta(t))\sigma_y]$. During the Ramsey interferometry sequence, the transverse component of $\mathbf{h}(q, t)$ is dynamically controlled with the lattice shaking parameters, $\{\nu_{I(II)}, A_{I(II)}, \varphi_{I(II)}\}$.

For an atom initially prepared in the $|q, s\rangle$ state, its final state after the Ramsey interferometry sequence is given by

$$\begin{pmatrix} c_p(q) \\ c_s(q) \end{pmatrix} = R_{\hat{\mathbf{h}}_{II}(q)}(\xi_{II}) R_{\hat{\mathbf{z}}}(h_z(q)T_e/\hbar) R_{\hat{\mathbf{h}}_I(q)}(\xi_I) \begin{pmatrix} 0 \\ 1 \end{pmatrix}, \quad (6.8)$$

where $\mathbf{h}_{I(II)}$ is the \mathbf{h} vector in the first (second) lattice shaking and $\xi_{I(II)} =$

$|\mathbf{h}_{\text{I(II)}}|\tau_{\text{I(II)}}/\hbar$. Here the global phase factor arising from the term of $-2\bar{t}_r \cos(q)\mathbb{I}$ in H_q is ignored under a proper gauge transformation. $R_{\hat{\mathbf{n}}}(\xi)$ represents a rotation around the $\hat{\mathbf{n}}$ axis by ξ on the Bloch sphere formed by $|q, p\rangle$ and $|q, s\rangle$, and thus, the system's overall evolution is described as a composition of three sequential rotations which correspond to the time evolutions in the first pulse, the intermediate period, and the second pulse, respectively [figure 6.4(b)]. As the time T_e of the intermediate period increases, the atom population in the $|q, p\rangle$ state, $n_p(q) = |c_p(q)|^2$ would show oscillations, and its oscillation amplitude and phases can reveal the geometric relation between $\mathbf{h}_{\text{I}}(q)$ and $\mathbf{h}_{\text{II}}(q)$.

In our experiment, we examine two cases of $(\nu_{\text{I}}, \nu_{\text{II}}) = (1, 1)$ and $(2, 1)$ with $\varphi_{\text{I(II)}} = 0$ and $\tau_{\text{I(II)}} = 2\pi/\omega_{\text{I(II)}}$. We measure the momentum distribution $n(k)$ after applying the two pulses of lattice shaking with increasing T_e . In figure 6.5(a), the measurement result for the $(\nu_{\text{I}}, \nu_{\text{II}}) = (1, 1)$ case is presented, where the shaking amplitude is set to be $A_{\text{I(II)}}/2\pi = 5$ kHz to obtain $\xi_{\text{I(II)}} = \pi/4$ for $q = \pm 0.7\pi$. The population oscillations with increasing T_e are clearly observed for each q and the oscillation frequency is found to be in good quantitative agreement with $\omega_{sp}(q)$ [figure 6.7(a)]. Next, the measurement result for $(\nu_{\text{I}}, \nu_{\text{II}}) = (2, 1)$ is presented in figure 6.5(b). In the measurement, the driving amplitude for the first pulse ($\nu_{\text{I}} = 2$) is changed to $A_{\text{I}}/2\pi = 8$ kHz to keep $\xi_{\text{I}} = \pi/4$ for $q = \pm 0.7\pi$, whereas that for the second pulse ($\nu_{\text{II}} = 1$) is the same as in the previous $(\nu_{\text{I}}, \nu_{\text{II}}) = (1, 1)$ measurement. Remarkably, we observe that the Ramsey signals exhibit an asymmetric fringe pattern with respect to $k = 0$, which is in stark contrast to the $(\nu_{\text{I}}, \nu_{\text{II}}) = (1, 1)$ case where the Ramsey signals are mirror-symmetric. Based on the fact that the transverse component of $\mathbf{h}_{\text{II}}(q)$ with $\nu_{\text{II}} = 1$ is uniform over the BZ, the observed asymmetric fringe signals indicate that the transverse component of $\mathbf{h}_{\text{I}}(q)$ with $\nu_{\text{I}} = 2$ has opposite

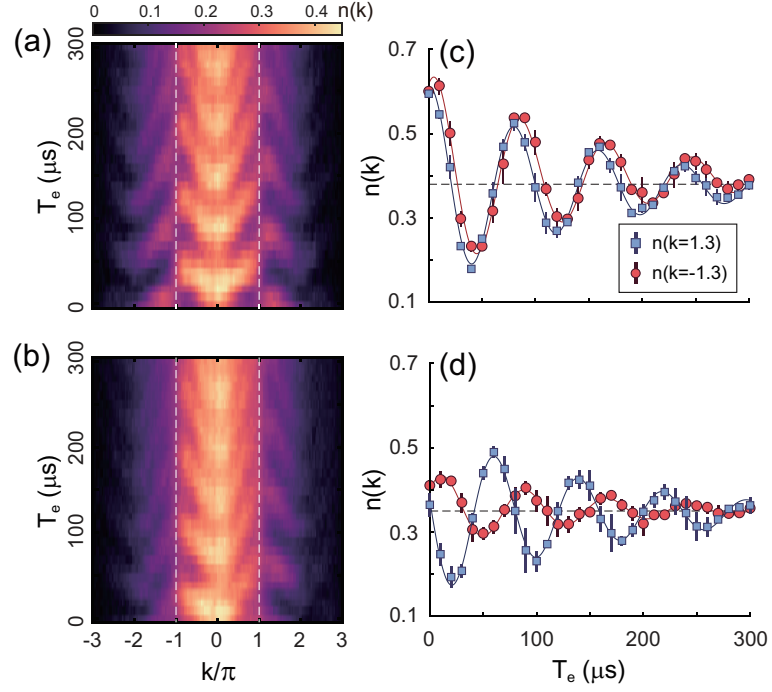


Figure 6.5: Momentum-resolved Ramsey interferometry signal. Momentum distribution $n(k)$ as a function of T_e for (a) $(\nu_I, \nu_{II}) = (1, 1)$ and (b) $(2, 1)$, where $\varphi_{I(II)} = 0$ and $\tau_{I(II)} = 2\pi/\omega_{I(II)}$. (c), (d) $n(k)$ at $k = \pm 1.3\pi$ as a function of T_e in (a) and (b), respectively. The solid lines are the damped sinusoidal function fits to the data. Each data point was obtained from seven measurements and its error bar indicates their standard deviation.

directions for $q > 0$ and $q < 0$, i.e., $h_{2,\rho}(-q) = -h_{2,\rho}(q)$, thus corroborating the winding structure of $\mathbf{h}_2(q)$.

In figures 6.5(c) and (d), we display the population $n(k)$ at $k = \pm 1.3\pi$, corresponding to $n_p(q = \mp 0.7\pi)$, as a function of T_e for the $(\nu_I, \nu_{II}) = (1, 1)$ and $(2, 1)$ cases, respectively. The population shows damped oscillations with increasing T_e and the damping might be attributed to atom-atom interactions and/or the spatial inhomogeneity of the trapped sample. From the damped sinusoidal functions fit to the data, we measured the phase difference between the two oscillation curves to be 0.10π for $(\nu_I, \nu_{II}) = (1, 1)$ and 0.77π for $(\nu_I, \nu_{II}) = (2, 1)$, which are slightly different from the expected values of 0 and π , respectively. We attribute such a small deviation to the off-resonant coupling effect, which is neglected in our model description and will be further discussed in the next section.

As a further comparison of the $(\nu_I, \nu_{II}) = (1, 1)$ and $(2, 1)$ cases, we also examine the dependence of the Ramsey signal on the driving phases φ_I and φ_{II} by measuring $n(k = \pm 1.3\pi)$ as a function of φ_I and φ_{II} with a fixed evolution time $T_e = 100 \mu s$ [figure 6.6]. For $(\nu_I, \nu_{II}) = (1, 1)$, the two populations at $k = \pm 1.3\pi$ oscillate in phase with period of 2π in both φ_I and φ_{II} . In contrast, for $(\nu_I, \nu_{II}) = (2, 1)$, they show out-of-phase oscillations with a different period of π in φ_I and 2π in φ_{II} . This observation is consistent with the different φ -dependence of $\hat{\rho}_1$ and $\hat{\rho}_2$. The π periodicity of the Ramsey signal with increasing φ_I for $\nu_I = 2$ is a direct consequence of that the inter-orbital coupling is generated via two-photon process.

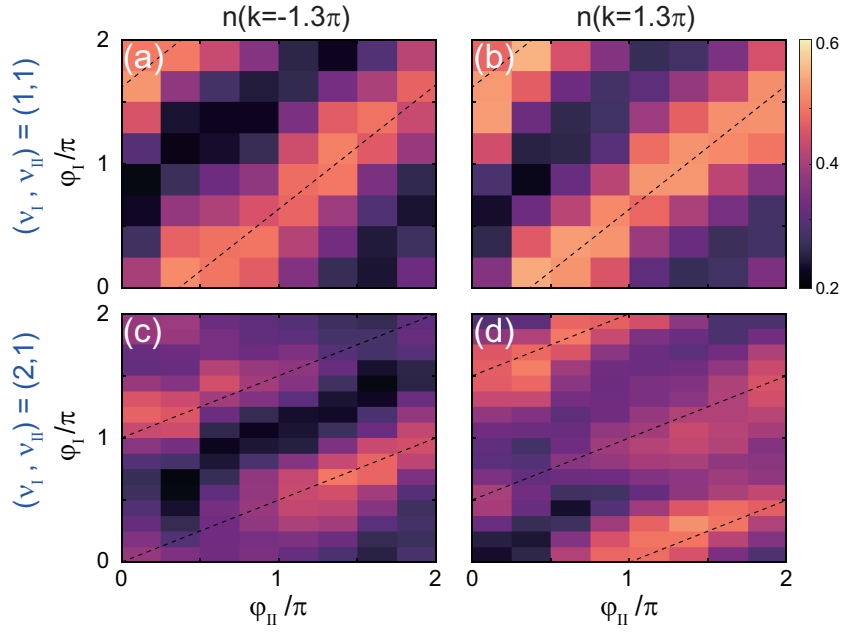


Figure 6.6: Driving phase dependence of the Ramsey fringe signal. Atomic densities $n(k)$ measured at (a,c) $k = -1.3\pi$ and (b,d) $k = 1.3\pi$ as functions of the driving phases φ_I and φ_{II} for $T_e = 100 \mu\text{s}$. $(\nu_I, \nu_{II}) = (1, 1)$ in (a,b) and $(2, 1)$ in (c,d). The experimental conditions are the same as those in figure 5. The dashed lines are guides to the eyes, indicating the maxima of the Ramsey fringes. In the case of $(\nu_I, \nu_{II}) = (2, 1)$, the fringe signal shows π -periodicity with increasing φ_I .

6.5 Discussions

6.5.1 Off-resonance coupling effect

In the model description of the resonantly shaken lattice system, we consider only the effects of the resonant coupling between the s and p orbitals. Although the model is efficient in capturing the essential topological features of the system, its improvement, in particular, by including the off-resonant inter-orbital coupling effects would be necessarily desirable for further development of the ladder system. To evaluate the limitations of the current model, we make a quantitative comparison between the experimental results in the Ramsey interferometry measurement and the prediction from the model. In figure 6.7, we characterize the Ramsey interferometry data presented in figure 6.5(a) and (b) with the oscillating frequency $\omega_f(k)$ and the phase $\phi(k)$, where $\{\omega_f(k), \phi(k)\}$ are determined from a damped sinusoidal function fit to the fringe signal $n(T_e; k)$ at each k . In the $(\nu_I, \nu_{II}) = (1, 1)$ case, we find that the measured $\{\omega_f(k), \phi(k)\}$ are well described by the model [figure 6.7(a) and (c)]. Here, the model prediction was numerically obtained by calculating equation 6.7 for the experimental conditions. On the other hand, in the $(\nu_I, \nu_{II}) = (2, 1)$ case, we observe that the measured oscillation phase $\phi(k)$ shows a quantitatively non-negligible deviation from the model prediction [figure 6.7(d)]. The deviation is pronounced near $k = 0$ and $\pm\pi$. These momentum regions are where the two-photon resonant coupling is weak for $h_{2,\rho}(q) \propto \sin(q)$ so that it is not only technically difficult to precisely determine ϕ but also likely to be sensitive to any off-resonant coupling effect.

In the two-photon resonance condition, the dominant off-resonant coupling must arise from the one-photon inter-orbital transition process. We spec-

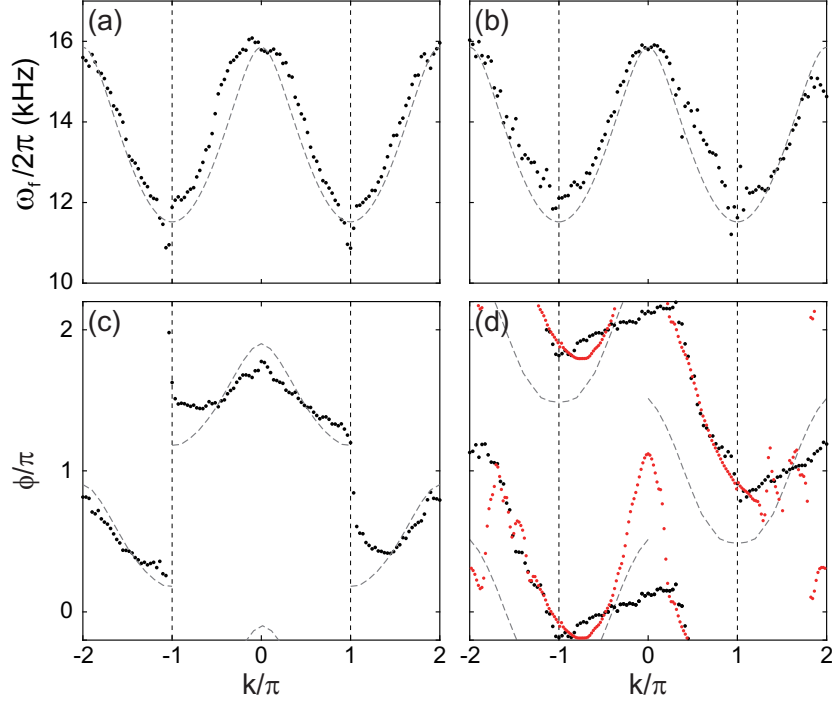


Figure 6.7: Characterization of the Ramsey fringe signals. The oscillation frequency $\omega_f(k)$ and phase $\phi(k)$ were determined from a damped sinusoidal function fit to the experimental data for each k . (a) and (c) for the data with $(\nu_I, \nu_{II}) = (1, 1)$ in figure 5(a), and (b) and (d) for the data with $(\nu_I, \nu_{II}) = (2, 1)$ in figure 5(b). The grey dashed lines indicate the model prediction calculated from equation (8). The red dots in (d) show the numerical result for the case where a uniform transverse vector of $(\max[h_\rho]/3)\hat{\mathbf{x}}$ is added to \mathbf{h}_I (see the text for details).

ulate that its effect might be approximated to direct *leakage* links between the two legs, and then represented by a uniform transverse component in \mathbf{h} as observed in the case of one-photon resonant coupling. To test the possibility, we recalculate equation 6.7 for the $(\nu_I, \nu_{II}) = (2, 1)$ experiment with adding a transverse field of $h_x \hat{\mathbf{x}}$ to \mathbf{h}_I for the first pulse period. We observe that the numerical result evolves somewhat closely to the experimental data when h_x increases to $\max[h_\rho]/3$ [figure 6.7(d)], supporting the leakage-link picture for the off-resonant coupling effect. The presence of such leakage links has an important implication that depending on the complex amplitude of the leakage links, \mathbf{h} might not be confined in a plane so that its winding number would be ill-defined. The off-resonant coupling effects, including those from the coupling to higher orbitals, warrant further theoretical and experimental investigations in future study.

6.5.2 Shaking with two resonant frequencies

The observation that one- and two-photon resonant couplings bring about the distinctive effects of direct and cross inter-leg links, respectively, prompts us to discuss an extension of the inter-leg link control in the ladder by using both types of resonant couplings. Specifically, we consider a situation in which the lattice shaking is applied as $\delta\omega_L(t) = A \sin(\omega t) + \tilde{A} \sin(2\omega t + \varphi)$ with $\Delta_2 = 0$. Here, together with the ω driving generating two-photon resonant coupling, the 2ω driving provides one-photon resonant coupling. We find that the inter-orbital coupling effects of the two drivings appears additive in the effective Hamiltonian at the same level of approximation used in equation 6.6, giving

$$\mathbf{h}(q) = \tilde{t}_v \hat{\boldsymbol{\rho}}_1(\varphi) + 2t_d \sin(q) \hat{\mathbf{y}} - 2t_r \cos(q) \hat{\mathbf{z}},$$

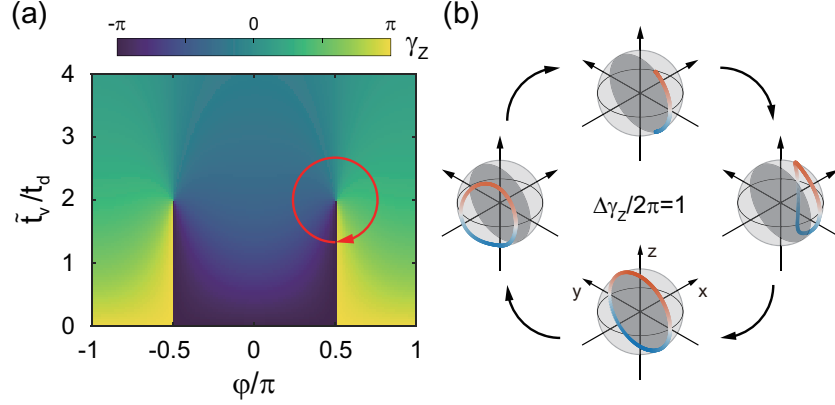


Figure 6.8: Topological charge pumping in the Creutz ladder. (a) Zak phase γ_Z in the plane of \tilde{t}_v/t_d and φ . The critical points are located at $\{\tilde{t}_v/t_d, \varphi\} = \{2, \pm\pi/2\}$. Along the path encircling one of the critical points, γ_Z continuously changes by 2π . (b) Evolution cycle of the pseudo-spin trajectory of the ground band on the Bloch sphere as the system adiabatically moves along the red encircling path in (a). The trajectory line covers the whole Bloch sphere in each cycle, resulting in one lattice site shift of atoms in the Creutz ladder.

with $\tilde{t}_v = (\tilde{A}/A)t_v$. This suggests that the direct inter-leg links can be generated independently in the Creutz ladder by simply adding a 2ω driving; furthermore, its complex amplitude can be controlled with the driving parameters \tilde{A} and φ . Even with the off-resonant coupling effects discussed in the previous subsection, this two-tone driving method would provide a flexible way to control the inter-leg links of the Creutz ladder system.

The extended control of the inter-leg links will enable to explore many interesting aspects of the topological ladder system. First of all, the topological phase transition of the Creutz ladder can be studied in a controlled manner, which occurs at $\{\tilde{t}_v, \varphi\}_c = \{2t_d, \pm\pi/2\}$, accompanied by the band gap closing at $q = \pm\pi/2$ and a sudden change of the winding number of $\mathbf{h}(q)$. Anomalous scaling of defect formation was predicted for the phase transition dynamics due

to the topological properties of the system [122]. Equipped with the dynamic control of the inter-leg links, we can also envisage a realization of a topological charge pump in the Creutz ladder [103]. For example, when the direct link parameters $\{\tilde{t}_v, \varphi\}$ are controlled to adiabatically encircle one of the critical points in the parameter space, the Zak phase, γ_Z , continuously changes by 2π per cycle (figure 6.8), which would result in one lattice site shift of atoms in the ladder.

6.6 Conclusion

We have demonstrated the realization of the Creutz ladder in a periodically shaken 1D optical lattice via two-photon resonant coupling. The topological structure of the Creutz ladder was characterized with the winding structure of $\mathbf{h}_2(q)$ in the BZ. By the shaking spectroscopy, the longitudinal component of \mathbf{h}_2 was directly measured as $h_z = -2t_r \cos(q)$, and using the Ramsey interferometry, the asymmetric relation of its transverse component, $h_{2,\rho}(-q) = -h_{2,\rho}(q)$, was demonstrated. From the observation that one- and two-photon resonant couplings generate direct and diagonal inter-leg links, respectively, in the ladder system, we suggested the two-tone driving method of simultaneously exploiting both resonant couplings, which would allow the controlled study of the topological phase transition dynamics and the realization of a topological charge pump. As another extension of this work, topological flat band engineering may be pursued with the Creutz ladder system, which would provide interesting opportunities for observing possible emergence of correlated topological phases [130, 131]. In interacting two-leg ladder systems, many correlated topological phases and associated edge states were theoretically discussed [102, 104, 124–126]. Finally,

we also expect that the two-photon resonant coupling method can be readily applied to 2D optical lattice systems, providing an alternative route to investigate anomalous quantum Hall states [132, 133].

Chapter 7

Topological pumping in resonantly driven optical lattice

In this chapter, we numerically study the topological properties of a resonantly shaken one-dimensional optical lattice system in a two-band approximation, where the lattice position is periodically driven with two harmonic frequencies to induce the on-site and site-hopping interband transitions. Using a Floquet Hamiltonian description, we show that a pair of degenerate edge states appear for a certain critical driving condition and that the corresponding topological phase is protected by the chiral symmetry of the periodically driven system. The Zak phase of the Floquet band oscillates in time due to the micromotion under the periodic driving and we find that it has a quantized value only when the symmetry condition is explicitly satisfied. We describe the topological charge pumping effect arising from a cyclic change of the driving parameters and discuss its experimental realization with a current optical lattice system.

7.1 Introduction

Topological insulator has been extensively investigated because of its intriguing gapless surface states protected by underlying symmetry [98]. In recent, this unusual quantum phases have been realized and studied in periodically driven system, which is referred as Floquet topological insulator [68, 134–139]. Based on the Floquet theorem, the dynamics governed by periodic time-dependent Hamiltonian can be well described by time-independent Floquet Hamiltonian, replacing properties of static system. Under the proper Floquet engineering, system can acquire interesting topological properties.

The ultracold atoms in optical lattice is suitable platform to investigate the Floquet topological insulator, due to its ability to tune the parameters in large space, and isolation from environment. Periodic driving with proper resonant condition can generate non-trivial topological phases. Raman laser coupling can implement synthetic gauge field [61, 96, 97, 116], and shaking optical lattices can induce next-nearest hopping [66, 105, 140, 141] in optical lattice system, which lead to topological phases.

These Floquet engineerings are based on the time-independent description of the driven system. However, Floquet Hamiltonian actually depends on the choice of initial time, which is referred as micromotion [79]. Because micromotion can strongly affect the topological properties and corresponding observables of the system, studying micromotion will improve understanding on the Floquet topological phases.

Topological charge pumping is one of peculiar example of manifestation of topology in 1D quantum transport, where transported charge per pump cycle is connected to topological invariant [142–145]. It was suggested that topological

charge pumping can be realized in Floquet 1D system [146], but the effect of micromotion has not been much dealt with.

Recently, we demonstrated that a 1D Floquet topological ladder can arise in resonantly shaken 1D optical lattice [121, 141], whose structure is similar to the topological two-leg ladder, the Creutz model [92]. Under the proper resonant shaking frequency, non-trivial edge states occur due to the site-hopping interband transition between two band states. In this work, we present a numerical study on resonantly shaken one-dimensional optical lattice and investigate topological charge pumping. We find that the bulk-edge correspondence of the Floquet bands depends on stroboscopic timeframe, because of symmetry of driven Hamiltonian. As a result, Zak phase oscillates within each period, while the Floquet system maintains degenerate edge states. This crucially affects the adiabatic transport, resulting in micromotion in pumped charge.

7.2 Resonantly shaken optical lattice

7.2.1 Two-band model description

Let us consider a fermionic atom in a 1D optical lattice potential, $V(x - x_0(t))$, where the lattice position $x_0(t)$ is time-dependent. The lattice position is determined by the relative phase of the two laser beams involved in forming the optical lattice, and in experiment, its driving can be simply achieved by mechanically modulating the position of a retro-reflecting mirror for the laser beams. In the co-moving reference frame with the driven optical lattice, the system's Hamiltonian is given by

$$\hat{H}(t) = \frac{\hat{p}^2}{2m} + V(x) - F(t)\hat{x}, \quad (7.1)$$

where m is the atomic mass and $F(t) = -m\ddot{x}_0(t)$ represents the inertial force arising from the driving.

In the tight binding approximation, the Hamiltonian is expressed as

$$\begin{aligned} \hat{H}(t) = \sum_{j,\alpha} \left[\epsilon_\alpha c_{j,\alpha}^\dagger c_{j,\alpha} - (t_\alpha c_{j,\alpha}^\dagger c_{j+1,\alpha} + \text{H.c.}) \right. \\ \left. - F(t)a \left(j c_{j,\alpha}^\dagger c_{j,\alpha} + \sum_{\beta \neq \alpha} \eta_{\alpha\beta} c_{j,\alpha}^\dagger c_{j,\beta} \right) \right], \end{aligned} \quad (7.2)$$

where $c_{j,\alpha}$ ($c_{j,\alpha}^\dagger$) is the annihilation (creation) operator for the atom in the Wannier state $|j, \alpha\rangle$ on lattice site j in α band. $\epsilon_\alpha = \langle j, \alpha | \hat{H}_{\text{stat}} | j, \alpha \rangle$ and $t_\alpha = -\langle j, \alpha | \hat{H}_{\text{stat}} | j+1, \alpha \rangle$ with $H_{\text{stat}} = \frac{p^2}{2m} + V(x)$ are the on-site energy and nearest-neighbor hopping amplitude of the α band in the stationary system, respectively. a is the lattice spacing and $\eta_{\alpha\beta} = \frac{1}{a} \langle j, \alpha | \hat{x} | j, \beta \rangle$ is the dimensionless dipole matrix element for on-site interband transition [147]. Under the gauge transformation with $\hat{U}(t) = \exp[-i\theta(t) \sum_{j,\alpha} j c_{j,\alpha}^\dagger c_{j,\alpha}]$ and $\theta(t) = -\frac{a}{\hbar} \int_0^t dt' F(t')$, the system's Hamiltonian is re-expressed as

$$\begin{aligned} \hat{H}(t) = \sum_{j,\alpha} \left[\epsilon_\alpha c_{j,\alpha}^\dagger c_{j,\alpha} - (t_\alpha e^{-i\theta(t)} c_{j,\alpha}^\dagger c_{j+1,\alpha} + \text{H.c.}) \right. \\ \left. - F(t)a \sum_{\beta \neq \alpha} \eta_{\alpha\beta} c_{j,\alpha}^\dagger c_{j,\beta} \right], \end{aligned} \quad (7.3)$$

where the third term in Eq. 7.2 is absorbed into the time-dependent tunneling amplitude.

We investigate a case where the optical lattice is periodically driven with two harmonic frequencies, ω and 2ω , i.e., $x_0(t) = x_\omega \cos(\omega t) + x_{2\omega} \cos(2\omega t + \varphi)$ with φ being the relative phase of the two harmonic driving, and the modulation frequency 2ω is close to the energy gap between the two lowest, s and p bands, resulting strong band hybridization. Here we assume that the two lowest bands

are energetically well separated from higher bands in the static lattice system so that the effects of their coupling to the higher bands under the driving are negligible. We note that this condition can be met by engineering an optical lattice potential with a double well structure (see Sec.V). Taking the two-band approximation, we obtain the Bloch Hamiltonian for the system from Eq. 7.3 in the basis of $\hat{\Psi}_q = (c_{q,p}, c_{q,s})^T$, where $c_{q,s(p)}$ is the annihilation operator for momentum q in the $s(p)$ band, as

$$\begin{aligned}\hat{\mathcal{H}}(q, t) = & \left(\bar{\epsilon} - 2\bar{t} \cos[q - \theta(t)] \right) \mathbb{I} - F(t) a \eta_{sp} \sigma_x \\ & + \left(\epsilon - 2t \cos[q - \theta(t)] \right) \sigma_z,\end{aligned}\tag{7.4}$$

where $2\bar{\epsilon} = (\epsilon_p + \epsilon_s)$, $2\epsilon = (\epsilon_p - \epsilon_s)$, $2\bar{t} = (t_p + t_s)$, $2t = (t_p - t_s)$, \mathbb{I} is the identity matrix, and $\boldsymbol{\sigma} = \{\sigma_x, \sigma_y, \sigma_z\}$ are the Pauli matrices. q is expressed in units of $1/a$. In the two-harmonic driving, $F(t) = F_{0,\omega} \cos(\omega t) + F_{0,2\omega} \cos(2\omega t + \varphi)$ with $F_{0,\omega'} = m x'_{\omega} \omega'^2$, giving $\theta(t) = -K_{\omega} \sin(\omega t) - K_{2\omega} \sin(2\omega t + \varphi)$ with $K_{\omega'} = F_{0,\omega'} a / \hbar \omega'$.

7.2.2 Effective static description

In periodically driven system, Floquet Hamiltonian is difficult to be expressed in a simple form [81]. However, in the high-frequency limit, where the driving frequency is sufficiently larger than any other energy scales, we can introduce perturbative expansion of Floquet Hamiltonian to capture physically essential features of driven system [79, 82, 85, 118]. From the expansion method, long-time dynamics of the system can be described by effective Hamiltonian, which is time-independent description.

We applied unitary transformation that rotates with frequency $\hbar\omega = \epsilon$ to investigate resonant process. Then, from the periodically driven Hamiltonian

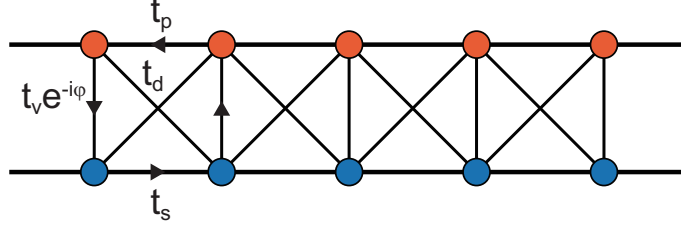


Figure 7.1: Effective ladder model of resonantly shaken optical lattice. Band states compose legs of the ladder, and coherent 1(2)-photon resonant interband coupling offers vertical (diagonal) hopping between legs. Here, t_α denotes the intraleg hopping amplitude of α band, t_v and t_d indicate amplitude of interband coupling. Relative driving phase φ adds hopping phase on t_v . The opposite sign of intraleg hopping ($t_s > 0, t_p < 0$) results in π flux per plaquette.

expanded in a Fourier form as $\hat{\mathcal{H}}(t) = \sum_m e^{im\omega t} \hat{\mathcal{H}}_m$, we can obtain the effective time-independent Hamiltonian using the high-frequency expansion method,

$$\hat{\mathcal{H}}_{\text{eff}} = \hat{\mathcal{H}}_0 + \sum_{m>0} \frac{[\hat{\mathcal{H}}_m, \hat{\mathcal{H}}_{-m}]}{m\hbar\omega}, \quad (7.5)$$

up to first order term [79, 82, 85, 118]. We obtained the effective Hamiltonian for $\hat{\mathcal{H}}(t)$ in a form of

$$\hat{\mathcal{H}}_{\text{eff}}(q) \approx \bar{E}(q)\mathbb{I} + \mathbf{h}(q) \cdot \boldsymbol{\sigma}, \quad (7.6)$$

where $\bar{E}(q) = \bar{\epsilon} - 2\bar{t}\mathcal{J}_0(K_\omega)\cos(q)$, and the vector $\mathbf{h}(q) = \{-t_v\cos(\varphi), -t_v\sin(\varphi) - 2t_d\sin(q), -2t'\cos(q)\}$, with $t_v = \hbar\omega K_{2\omega}\eta_{sp}$, $t_d = K_\omega\eta_{sp}t\mathcal{J}_1(K_\omega)$, $t' = t\mathcal{J}_0(K_\omega)$. Here \mathcal{J}_n is n th order Bessel function of the first kind. It is shown that t_v is induced by fast driving with frequency 2ω in zeroth-order process (1-photon process), while the t_d is induced by slow driving with frequency ω in first-order process (2-photon process).

The system can be depicted as a two-leg ladder system as shown in Fig. 7.1 under the synthetic dimensional framework [95]. t_v and t_d correspond

to the amplitudes of the direct and diagonal links between the two legs, so effective Hamiltonian (7.6) realizes a generalized Creutz ladder model. Specifically, topologically nontrivial states can exist in the system because of diagonal links in the ladder [101]. In the limit of $\bar{\epsilon} = \bar{t} = 0$, which is a smooth deformation, effective Hamiltonian has chiral symmetry at $\varphi = \pm\pi/2$, as $\sigma_x \hat{\mathcal{H}}_{\text{eff}}(q) \sigma_x = -\hat{\mathcal{H}}_{\text{eff}}(q)$. Two distinctive topological phases are separated by critical point $\{t_v/t_d, \varphi\} = \{2, \pm\pi/2\}$, where gap closing occurs. Interestingly, when $\varphi \neq \pm\pi/2$, symmetry of the effective Hamiltonian is broken. Therefore, two distinct topological phases can be adiabatically connected in $\{t_v/t_d, \varphi\}$ space. Then, if the system follows a cyclic path in parameter space $\{t_v/t_d, \varphi\}$, pumped charge per cycle is quantized to integer values [103].

7.3 Topological properties and micromotions

The effective Hamiltonian (7.6) can offer clear and intuitive picture on topological nature of resonantly shaken optical lattice. In the high frequency limit, where the driving frequency is sufficiently larger than any other energy scale in the system, physical properties of the system would be enough to be described with effective Hamiltonian. However, away from this limit, micromotion within each period can play crucial role in dynamics and measurement. It is practical to exactly evaluate Floquet time-evolution operator without further approximation, which naturally carries information on micromotion.

For periodically driven system, Floquet states are eigenstates of a time-evolution operator over one driving period $T = 2\pi/\omega$,

$$\hat{U}(T, 0) = \mathcal{T} \exp \left(-\frac{i}{\hbar} \int_0^T \hat{\mathcal{M}}(t) dt \right), \quad (7.7)$$

where \mathcal{T} is time-ordering operator, and $\hat{\mathcal{M}}(t) = \hat{H}(t)$ or $\hat{\mathcal{H}}(q, t)$ for finite real space or bulk momentum Hamiltonian. Its eigenvalue and eigenstates are given by $\hat{U}(T, 0)|\psi_n\rangle = e^{-i\varepsilon_n T/\hbar}|\psi_n\rangle$, where $\varepsilon_n \in [-\frac{\hbar\omega}{2}, \frac{\hbar\omega}{2}]$ is quasienergy. As the initial eigenstate $|\psi_n\rangle$ at $t = 0$ will be also eigenstate at $t = mT$, the dynamics of the system can be described in stroboscopic manner by Floquet Hamiltonian

$$\hat{H}_F = \frac{i}{T} \log[\hat{U}(T, 0)]. \quad (7.8)$$

Quasienergy eigenvalues and eigenstates are numerically obtained by diagonalizing Floquet time-evolution operator with $\hat{U}(T, 0) = \prod_{n=0}^{N-1} \hat{U}(t_{n+1}, t_n)$ and $\hat{U}(t_{n+1}, t_n) \approx \exp[-\frac{i}{\hbar} \hat{\mathcal{M}}(t_n) \Delta t]$, where $t_n = \frac{nT}{N}$ and $\Delta t = \frac{T}{N}$. We consider the parameters $\epsilon_s = 0$, $\epsilon_p = 4.4E_r$, $t_s = 0.03E_r$, $t_p = -0.31E_r$, which are chosen at previous experimental demonstration [141], where $E_r = \hbar\pi^2/2ma^2$, and using modulation frequency $\hbar\omega = \epsilon = 2.2E_r$.

7.3.1 Edge states and symmetry

When the frequency of the periodic driving meets the condition $\hbar\omega \approx \epsilon$, periodic force induces coherent interband coupling, and corresponding Floquet states can possess topological states. At $x_\omega \neq 0$ and $x_{2\omega} = 0$, we can find degenerate in-gap states exponentially localized at opposite edges which is a hallmark of 1D topological phase [Fig. 7.2 (a) and (b)], indicating that the 2-photon resonant shaking generates non-trivial topological state.

Topological property of the system can be changed when we introduce high-frequency component, $x_{2\omega} \neq 0$. At $\varphi = \pm\pi/2$, a pair of in-gap states maintain degeneracy until the critical point $x_{2\omega}^c$ that is a gap closing point of bulk spectrum [Fig 7.2(c)]. Therefore, it suggests that resonantly shaken optical lattice has two distinctive topological phases, and their topology is protected by

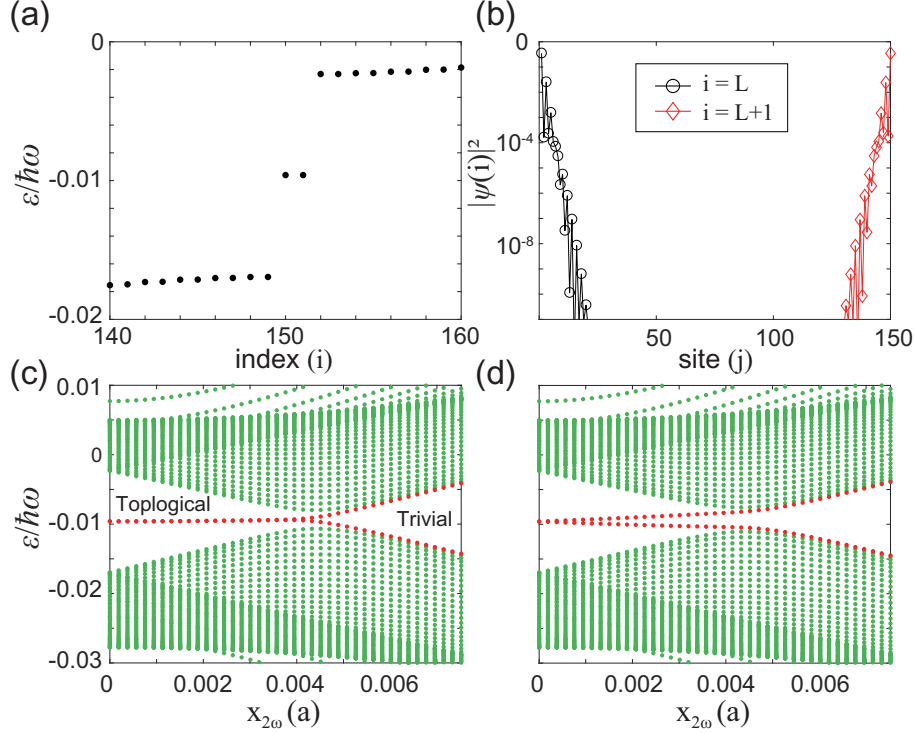


Figure 7.2: (a) Quasienergy spectrum of shaken 1D optical lattice of length $L = 150$. Driving parameter is given by $\hbar\omega = \epsilon$ and $x_\omega = 0.11a$, without high frequency driving $x_{2\omega} = 0$. (b) Probability density of wave functions for the in-gap states in (a). (c) Quasienergy spectrum as a function of $x_{2\omega}$ at $\varphi = 0.5\pi$. In-gap states survive and maintain its degeneracy until critical point. (d) Quasienergy spectrum as a function of $x_{2\omega}$ at $\varphi = 0.45\pi$.

some symmetry. If $\varphi \neq \pm\pi/2$, degeneracy of edge states are lifted by arbitrary small $x_{2\omega}$ [Fig. 7.2(d)]. This gives us full controllability on topological property of the driven optical lattice.

In static system, topological property can be characterized by bulk invariant of the bands, following bulk-edge correspondence. For example, bulk winding number or Zak phase of 1D system with chiral symmetry has direct relation to the number of edge states. In Floquet system, topological invariant

also can be similarly defined with quasienergy bands, but symmetry should be considered in time as well as in spatial dimension. Therefore, choice of timeframe can play an important role in symmetry, eigenstates, and topological properties.

To simplify the discussion, we neglect the identity term in $\hat{\mathcal{H}}(q, t)$ by gauge transformation, which is equivalent to the limit of $t_s = -t_p$ and $\epsilon_s = -\epsilon_p$. Since it can be viewed as a smooth deformation, topological property, such as the number of edge states, is preserved. Then smoothly-deformed Hamiltonian is given by

$$\tilde{\mathcal{H}}(q, t) = -\tilde{F}(t)a\eta_{sp}\sigma_x + \left(\epsilon - 2t \cos[q - \tilde{\theta}(t)]\right)\sigma_z, \quad (7.9)$$

where we introduce $\tilde{F}(t) = F_{0,\omega} \cos[\omega(t + t_0)] + F_{0,2\omega} \cos[2\omega(t + t_0) + \varphi]$ and $\tilde{\theta}(t) = -\frac{a}{\hbar} \int_0^t dt' \tilde{F}(t')$ are similar as before except the addition of initial time $t_0 \in [0, 2\pi/\omega]$. When $\omega t_0 = \pm \frac{\pi}{2}$ and $\varphi = \pm \frac{\pi}{2}$, the Hamiltonian has chiral symmetry as it satisfies relation

$$\sigma_x \tilde{\mathcal{H}}(q, t) \sigma_x = -\tilde{\mathcal{H}}(q, -t). \quad (7.10)$$

Due to the chiral symmetry, the number of edge states corresponds to Zak phase of quasienergy bands [134, 148, 149]. From the smooth deformation, Zak phase of Floquet bands in original Hamiltonian 7.4 can be related to the number of edge states.

7.3.2 Micromotions

In our system, the micromotion can be directly observed by charge transportation. As the quasienergy of Floquet state is preserved under the driving, we can estimate charge transport based on adiabatic theorem. The transport of

the system is directly related to the Berry curvature of the band in $q - t$ space Ω_{qt}^n [150]. The transported charge of n th band is given by

$$\Delta c_n(t) = -\frac{1}{2\pi} \int_0^t dt' \int_{\text{BZ}} dq \Omega_{qt}^n, \quad (7.11)$$

where $\Omega_{qt}^n = i[\langle \frac{\partial \psi_n}{\partial q} | \frac{\partial \psi_n}{\partial t} \rangle - \langle \frac{\partial \psi_n}{\partial t} | \frac{\partial \psi_n}{\partial q} \rangle]$. If we consider closed path in Brillouin zone, it can be equivalently expressed by [151, 152],

$$\begin{aligned} \Delta c_n(t) &= \frac{i}{2\pi} \int_0^t dt' \int_{\text{BZ}} dq \partial_{t'} \langle \psi_n(t') | \partial_q | \psi_n(t') \rangle \\ &= \frac{1}{2\pi} \int_0^t dt' \partial_{t'} \gamma_n(t'), \end{aligned} \quad (7.12)$$

where $\gamma_n(t) = i \int_{\text{BZ}} dq \langle \psi_n(t) | \partial_q | \psi_n(t) \rangle$ is Zak phase of n th band [91].

We numerically calculated Zak phase of quasienergy bands of $\hat{U}(t_0 + T, t_0) = \mathcal{T} \exp[-\frac{i}{\hbar} \int_{t_0}^{t_0+T} \hat{\mathcal{H}}(q, t) dt]$, to evaluate its dependence on timeframe. In Figure 7.3, we present an overview on Zak phase of the resonantly shaken optical lattice. Figure 7.3(a)-(c) show the Zak phase of lower Floquet band γ_- at $t_0 = 0, T/4, T/2$, as a function of $\{x_{2\omega}, \varphi\}$ at $x_\omega = 0.11a$. The critical point located at $\{x_{2\omega}^c, \varphi^c\} = \{0.0044a, \pm\pi/2\}$ is fixed under the variation of t_0 , showing preserved topological property. This critical point precisely corresponds to the $t_v/t_d = 2$ in effective Hamiltonian description. Zak phase is continuous around the critical point except the branch cut of size 2π , but, overall features different within t_0 .

Zak phase is only quantized at $\omega t_0 = \frac{\pi}{2}$ and $\varphi = \pm\frac{\pi}{2}$ [Fig. 7.3b], where $\tilde{\mathcal{H}}(q, t)$ has chiral symmetry. Zak phase of lower quasienergy bands is $\gamma_- = \pi \pmod{2\pi}$ when $x_{2\omega} < x_{2\omega}^c$, which clearly corresponds to the $n_{\text{edge}} = 1$ at each edge. If $x_{2\omega} > x_{2\omega}^c$, $\gamma_- = 0$ indicates the trivial phase without edge states.

When $\omega t_0 \neq \pm\frac{\pi}{2}$ or $\varphi \neq \pm\frac{\pi}{2}$, Zak phase does not correspond to the number of edge states, because $\tilde{\mathcal{H}}(q, t)$ has no chiral symmetry. Nonetheless, we can discuss topological property of the system. $\hat{U}(t_0 + T, t_0)$ is topologically

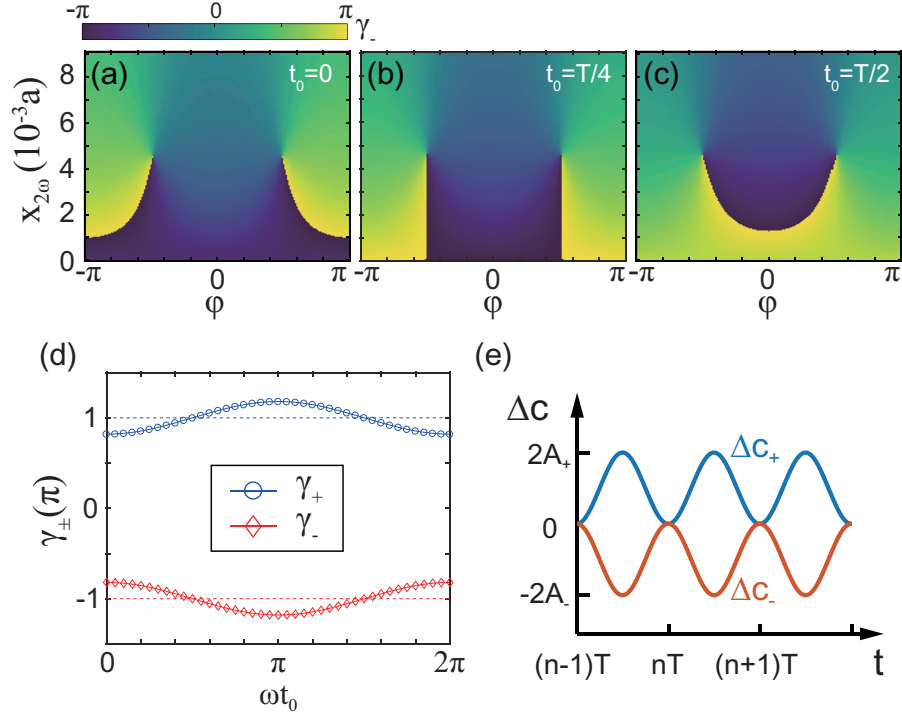


Figure 7.3: (a) Zak phase of lower Floquet band γ_- in parameter space $\{x_{2\omega}, \varphi\}$ with fixed $x_\omega = 0.11a$, at $t_0 = 0$, (b) $t_0 = T/4$, and (c) $t_0 = T/2$. (d) Zak phase at $\varphi = \pi/2$, $x_\omega = 0.11a$, and $x_{2\omega} = 0$, as a function of t_0 . (e) Micromotion of transported charge. Amplitude of micromotion is given by $2A_{\pm} = [\max(\gamma_{\pm}) - \min(\gamma_{\pm})]/2\pi$. Here, we assume $x_\omega \gg x_{2\omega}$.

equivalent in t_0 , as no gap closing occurs along the t_0 . Obviously, quasienergy is equal in all timeframe, so the number of edge states is preserved in t_0 . For example, degenerate edge states exist at $\omega t_0 = 0 \neq \pm \frac{\pi}{2}$ [Fig. 7.2(a)]. However, because the Zak phase of quasienergy bands is ill-defined, its value is not quantized to zero or π [Fig. 7.3(d)]. We can claim that non-trivial edge states are preserved through the driving period, if the periodically driven Hamiltonian has well-defined symmetry at certain timeframe t_0 . On the other hand, relative driving phase can actually lift the degeneracy of edge modes, because φ

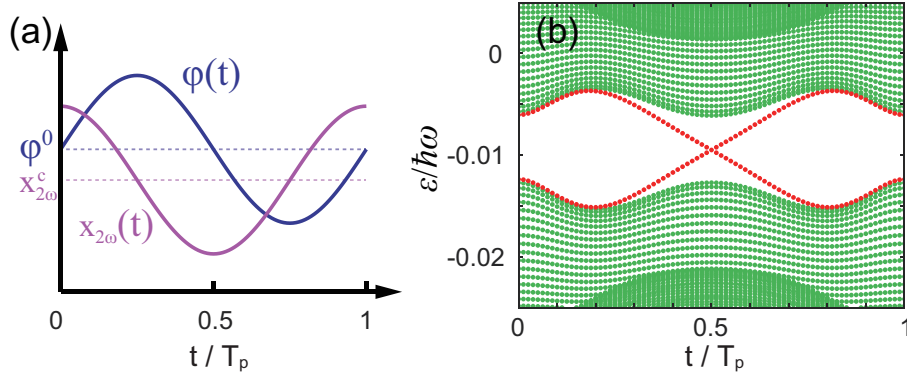


Figure 7.4: (a) Example of topological pumping trajectory with $\varphi(t) = \varphi^0 + \frac{\pi}{4} \sin(2\pi t/T_p)$, $x_{2\omega}(t) = x_{2\omega}^c + x_{2\omega}^m \cos(2\pi t/T_p)$. Here, $\varphi^0 = \pi/2 \in \{\varphi^c\}$ and $x_{2\omega}^m = 0.43x_{2\omega}^c$. This trajectory encircles the topological critical point $\{x_{2\omega}^c, \pi/2\}$. (d) Floquet quasienergy spectrum of finite system with $L = 150$, along the trajectory given in (a). In this spectrum, propagating edge modes exist between the bulk bands.

can change the quasienergy of the system. Indeed, driven Hamiltonian does not have well-defined symmetry at any t_0 when $\varphi \neq \pm\frac{\pi}{2}$.

In our resonantly shaken Hamiltonian (7.4), Zak phase oscillates within period for each parameter set, such as shown in Fig. 7.3(d). Following equation 7.12, transported charge will oscillate, and its amplitude is determined by Zak phase [Fig. 7.3(e)]. This is direct measurable quantity from micromotion in our periodically driven system.

7.4 Topological charge pumping

In charge pump scheme, we consider cyclic change of $x_{2\omega}(t)$ and $\varphi(t)$ in pumping period T_p , which satisfies $x_{2\omega}(t + T_p) = x_{2\omega}(t)$ and $\varphi(t + T_p) = \varphi(t)$. In equilibrium 1D system under time-dependent cyclic perturbation, eigenstates are periodic in two dimensions, because Hamiltonian will have periodic bound-

any condition in q and t . If parameter changes slow enough, system follows instantaneous eigenstates of the Hamiltonian. Following adiabatic transport relation (7.11), pumped charge over one cycle is quantized to the first Chern number [143, 150].

Our topological charge pumping scheme is based on the Floquet states of the resonantly shaken optical lattice. Although Hamiltonian cannot be exactly periodic under the change of parameters, system can follow instantaneous Floquet states in the adiabatic limit [153]. Therefore, we can get insight on dynamics in the adiabatic limit by looking through Floquet quasienergy spectrum. In Fig. 7.4(a), we visualize an example of pumping trajectory which is given by $\varphi(t) = \varphi^0 + \frac{\pi}{4} \sin(2\pi t/T_p)$, $x_{2\omega}(t) = x_{2\omega}^c + x_{2\omega}^m \cos(2\pi t/T_p)$, where $\varphi^0 = \pi/2 \in \{\varphi^c\}$ and $x_{2\omega}^m = 0.43x_{2\omega}^c$. When the trajectory encircles the critical point $\{x_{2\omega}^c, \varphi^c\}$, quasi-energy spectrum along the path clearly shows chiral propagating edge modes in bulk gap, which is an analogue of Chern insulator [Fig. 7.4(b)]. Therefore, system will show quantized transportation per each cycle. Because the energy gap between bulk bands does not close along the time, adiabatic condition can be satisfied when the T_p is sufficiently slower than the smallest band gap energy.

In numerical simulation, we consider initial state as spinless fermions fully filled in the lower (or upper) Floquet band, $|\psi_{\pm}(q, 0)\rangle$. Then the time-evolved states $|\psi_{\pm}(q, t)\rangle$ are calculated by solving the time-dependent Schrödinger equation under the periodically driven Hamiltonian (7.4), under the change of parameters $x_{2\omega}(t)$ and $\varphi(t)$. Local current j_{\pm} is calculated by computing expectation value of velocity operator $\hat{v}(q, t) = \partial \hat{\mathcal{H}}(q, t) / \partial (\hbar q)$, with relation $j_{\pm}(t) = (1/2\pi) \int_{\text{BZ}} \langle \psi_{\pm}(q, t) | \hat{v}(q, t) | \psi_{\pm}(q, t) \rangle$ [103, 150]. Pumped charge is calculated by integrating the local current $\Delta c_{\pm}(t) = \int_0^t d\tau j_{\pm}(\tau)$.

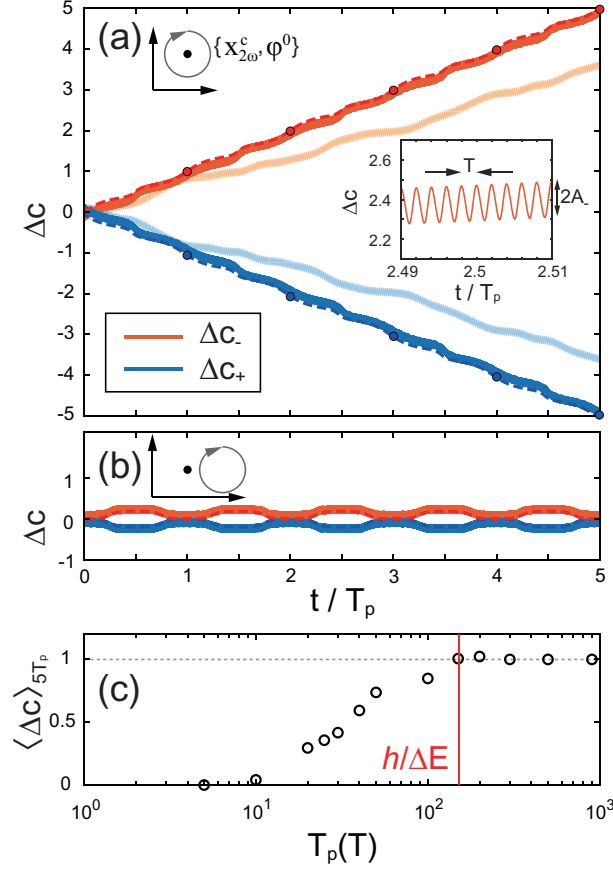


Figure 7.5: Numerically calculated pumped charge (a) when the trajectory encircles the critical point $\{x_{2\omega}^c, \varphi^0 = \pi/2\}$, (b) or not $\{x_{2\omega}^c, \varphi^0 = \pi\}$. Here the pumping period is $T_p = 900T$, and $x_{2\omega}^m = 0.43x_{2\omega}^c$. Inset shows micromotion of pumped charge, whose period is exactly the inverse of resonant driving frequency, $T = 2\pi/\omega$. Dashed lines are expected ΔC calculated from effective Hamiltonian $\hat{\mathcal{H}}_{\text{eff}}$. Faded lines shown in (a) are numerical results with non-adiabatic condition, $T_p = 50T$. (c) Mean transported charge over 5 cycles along the trajectory in (a). Red line indicates the scale of smallest energy gap ΔE during charge pumping.

Figure 7.5 shows the numerical results on the charge pumping. In the adiabatic condition, i.e. $T_p = 900T \gg h/\Delta E$, where ΔE is the smallest gap between two Floquet bands, the pumped charge over one cycle is quantized. When the parameters $x_{2\omega}(t)$ and $\varphi(t)$ encircles the topological critical point, charge in the system shifts by one site over each pumping cycle T_p , i.e. $\Delta c_{\pm}(nT_p) = \mp n$ [Fig. 7.5(a)]. When the trajectory of the pumping does not encircle the topological critical point, for example $\varphi^0 = \pi$, net transport after one cycle is zero [Fig. 7.5(b)]. This clearly indicates the connection between transport and topological property. The pumped charge of the upper band is also quantized but with opposite direction, because $\gamma_{-}(t) = -\gamma_{+}(t)$ in two band model.

The numerical results is in agreement with dynamics of effective Hamiltonian description, except the oscillation with period of T . This is originated from micromotion of the system. If we assume $T_p \gg T$, the values of $x_{2\omega}(t)$ and $\varphi(t)$ are almost maintained during short period T . Under this condition, instantaneous Floquet states and its Zak phase can be approximately defined. Since Zak phase of the system oscillates, pumped charge shows micromotion in addition to the global adiabatic current [Fig. 7.5(a), inset].

We note that topological relation in transport does not hold at the non-adiabatic condition. The numerical estimation of mean pumped charge over 5 cycles indicates that the adiabaticity is broken around $T_p = h/\Delta E$ [Fig. 7.5(c)].

7.5 Discussions

In typical experimental condition, ultracold atoms are initially prepared in the lowest band of the static optical lattice. In this regard, loading atoms onto the Floquet states is important preparing topological states. One possible approach

is slowly introducing the periodic driving in the system, to continuously connect the lowest band of the static lattice to the one of Floquet bands. If the gap is always opened during the loading process, atoms can be fully loaded onto the Floquet states in the adiabatic limit. Adiabatic passage can be obtained by ramping up the driving at initial frequency ω_i and slowly changing frequency to the target frequency ω_f , which can minimize Landau-Zener type interband transition. Practical initial frequency ω_i can be suggested in the range of $\epsilon/2\hbar < \omega_i < \epsilon/\hbar$, to reduce undesirable higher-order interband couplings during frequency ramp.

We note that topology of the Floquet band also should be considered for efficient loading [154]. Because the lowest band of the static optical lattice is topologically trivial, gap closing is inevitable if the target Floquet state is topologically non-trivial. Therefore, to make adiabatic passage, atoms should be first loaded onto topologically trivial Floquet state. For example, atoms can be loaded onto lower Floquet band linearly ramping up the driving amplitude from zero to the $x_\omega = 0.11a$, $x_{2\omega} > x_{2\omega}^c$ at frequency $\omega_i = 0.75(\epsilon/\hbar)$ initially, then increasing frequency to $\omega_f = \epsilon/\hbar$ slowly. Non-trivial Floquet states can be prepared by route where $x_{2\omega}$ and φ does not cross the topological critical point.

In this work, our numerical results are based on the two-band approximation. Away from this approximation, higher bands in static optical lattice can be resonantly coupled with two lowest bands. In this case, two-band topological phase can be interfered due to the participation of the other bands, or suffered by heating from subsequent interband transition to higher bands. For example, measurement on signature of topological ladder in shaken 1D optical lattice implies the participation of higher bands.

To mitigate these effects, double well optical lattice can be employed,

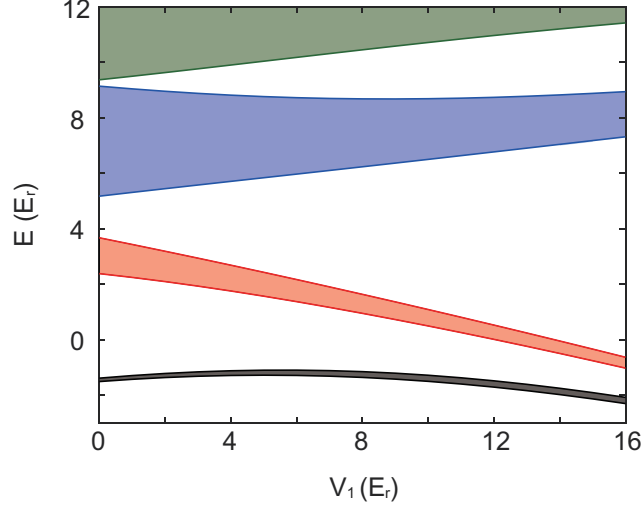


Figure 7.6: Dispersion of double well optical lattice as a function of V_1 , at $V_0 = 8E_r$.

which is given by

$$\hat{H}(t) = \frac{\hat{p}^2}{2m} + \frac{V_0}{2} \cos\left(\frac{2\pi}{a}x\right) + \frac{V_1}{2} \cos\left(\frac{4\pi}{a}x\right) - F(t)\hat{x}. \quad (7.13)$$

By increasing the depth of short lattice potential, V_1 , the lowest two bands are energetically isolated from higher bands [Fig. 7.6]. As the strength of n -photon resonant interband coupling is approximately given by order of $(K_\omega)^n$ [147], it can effectively suppress the effect from the higher bands. For example, when $V_0 = 8E_r$, $V_1 = 8E_r$, and $2\hbar\omega = \epsilon_p - \epsilon_s$, p -band is coupled to d -band via $n = 4 \sim 6$ process, while s - p bands are coupled via 2-photon process. In numerical estimation, we found that the participation of higher bands is under 1% up to $K_\omega < 1.4$, where driving offers sufficient gap between Floquet bands. Therefore, effective two-band model can be realized because of negligible resonant coupling to higher bands.

We have dealt with Floquet topological engineering of single-particle Hamiltonian. This can be readily extended to many-body physics by adding

interatomic interactions, which can offer opportunity for exploring many-body effects on topological properties [102]. However, interactions redistribute absorbed energy from driving field, so Floquet system will be heat up to infinite temperature [155]. In addition, heating can be enhanced further because of complicated excitation spectrum by interaction [129, 156, 157]. One approach to observe interacting Floquet states is to find and engineer prethermal state, which is transient but stable Floquet state before infinite thermalization [158]. In recent, prethermalization was observed in driven optical lattice system [159, 160], and the existence of prethermal regimes for resonantly driven system were theoretically expected [161, 162]. Therefore, experimental investigation on prethermal state at resonant condition would be interesting future work.

7.6 Summary

We numerically study topological property and topological charge pumping in resonantly shaken 1D optical lattice. Driven Hamiltonian have symmetry in specific timeframe where Zak phase corresponds to the number of edge states. In other stroboscopic timeframe, Zak phase is ill-defined, but degenerate edge states are preserved in all timeframe. Therefore, although resonant driving generates non-trivial edge states in the system regardless of timeframe, selection of timeframe is important to measure quantity related to the Zak phase. The temporal oscillation of Zak phase is directly related to the micromotion in adiabatic transport. As a result, when the system adiabatically undergoes topological charge pumping sequence, transported charge after pumping period T_p is quantized, but oscillates in a shaking period T . It suggests that micromotion would be vanished if periodic driving maintains the symmetry of Hamiltonian at

any timeframe. Our results demonstrate Floquet topological states in resonantly driven 1D optical lattice, and importance of micromotion on experimental measurement.

Chapter 8

Conclusions and Outlook

The main topic of this thesis was the realization of the topological ladder with resonant modulation. The ladder Hamiltonian was engineered in 1D optical lattice under the concept of synthetic dimension, where the degrees of freedom are regarded as extra dimension. Here, the band degree of freedom was first introduced for topological band engineering. By implementing moving optical lattice (or, Raman transition) and periodic shaking of lattice position with proper resonant condition, the artificial gauge field and next-nearest-neighbor hopping were successfully demonstrated, which led to the realization of topological ladders: Harper-Hofstadter like ladder and Creutz ladder.

In chapter 5, resonant coupling between band states are triggered by Raman transition. Raman transition acts as a moving optical lattice, and it offers a complex phase on resonant transition between band states, which leads to uniform artificial gauge field in ladder description composed of real and synthetic lattice sites. The band state resolved momentum distribution of the ground state was directly measured by band-mapping technique, and experimental results indicate chiral ground state. These chiral ground state were stable until the

localized limit at strong resonant coupling. The experimental results on quench dynamics, which can be interpreted as skipping orbit motion, also signifies the effect of strong gauge field. The momentum asymmetry in quench dynamics, originated from the weak next-nearest-neighbor hopping (or, nearest-neighbor hopping accompanied with band state changing), was also further examined with numerically predicted dynamics.

In chapter 6, we introduced the periodic shaking of the lattice position with frequency that is resonant to the energy difference between band states. Interband transition occurs when the integer multiples of shaking frequency reached band gap energy, and it was described by ladder model under the synthetic dimensional concept. Two resonant conditions, 1-photon and 2-photon resonant processes, are expected to generate vertical and diagonal hopping in the ladder description, which lead to realization of Creutz ladder. In these systems, the structure of effective Hamiltonian is examined by the resonant condition and interferometry with band state resolved momentum distribution. Observed experimental signatures indicated that 2-photon resonant process can generate topological states. In chapter 7, the extended scheme with two harmonic frequencies was suggested to demonstrate topological charge pumping. Zak phase of the system can be continuously manipulated by changing the relative driving amplitude and phase between two modulations. The adiabatic changing of parameters in closed trajectory will fix the transported charge to integer number. The micromotion and symmetry of the system were also discussed.

In this thesis, the experiments were demonstrated in the small interatomic interaction regime, and the topological band engineering is based on single particle physics. In condensed matter physics, many intriguing phenomena are driven by strong interaction, such as Kondo effect [163] and metal-insulator transi-

tion [164]. When the interaction is strong enough, the topological band and the correlation physics will compete with each other. Moreover, new topological states can arise by spontaneous symmetry breaking due to interaction. Therefore, implementing strong interaction in our engineered topological band will allow us to expand our knowledge on topological physics. For alkaline-earth-like Yb quantum gas, the ratio between interaction and kinetic energy can be tuned by depth of optical lattice, or the interatomic interaction can be manipulated through the scattering between two different electronic states, which is often called as *orbital Feshbach resonance* [165–167]. With the strong interaction, the stability of topological states in Hofstadter model which competes with magnetic order can be studied in optical lattice setup with artificial gauge field [168, 169]. Also, 1D topological Hubbard model could be studied with the inclusion of repulsive on-site interactions [102, 170]. Moreover, interaction induced topological Kondo insulator [171–173] could be simulated in the 1D limit with our ladder system composed of different band states [174–177]. With the aid of tomography technique that employs interference between wave functions of different band states [140], detailed information on correlate topological physics could be investigated.

Because our topological bands are realized with periodic modulation, the heating issue will be critical for the interacting system. According to eigenstate thermalization hypothesis (ETH), driven many-body systems heat up to infinite temperature, because driving energy will be redistributed and dissipated into the system through the interaction [155, 178]. This inhibits the observation of exotic correlated topological phases. One route to resolve the heating issue is to find prethermal regime, which is a interaction time scale of Floquet Hamiltonian settled down to exotic phases before the infinite heating [81, 179–182]. The

heating mechanisms in interacting quantum gases in driven optical lattice have been demonstrated recently [129,156,157,183], and signatures of prethermalization were observed [159,160]. Once understanding on heating mechanisms and prethermalization in our system are achieved, intriguing correlated topological phases could be observed in prethermal regime with strong interaction.

Bibliography

- [1] R. P. Feynman, “Simulating physics with computers,” *International Journal of Theoretical Physics*, vol. 21, pp. 467–488, 1982.
- [2] F. Arute, *et al.* “Quantum supremacy using a programmable superconducting processor,” *Nature*, vol. 574, pp. 505–510, 2019.
- [3] A. W. Harrow and A. Montanaro, “Quantum computational supremacy,” *Nature*, vol. 549, pp. 203–209, 2017.
- [4] J. Preskill, “Quantum Computing in the NISQ era and beyond,” *Quantum*, vol. 2, p. 79, 2018.
- [5] S. Lloyd, “Universal Quantum Simulators,” *Science*, vol. 273, pp. 1073–1078, 1996.
- [6] D. S. Abrams and S. Lloyd, “Simulation of Many-Body Fermi Systems on a Universal Quantum Computer,” *Physical Review Letters*, vol. 79, pp. 2586–2589, 1997.
- [7] N. C. Jones, R. Van Meter, A. G. Fowler, P. L. McMahon, J. Kim, T. D. Ladd, and Y. Yamamoto, “Layered Architecture for Quantum Computing,” *Physical Review X*, vol. 2, p. 031007, 2012.

- [8] M. H. Devoret and R. J. Schoelkopf, “Superconducting Circuits for Quantum Information: An Outlook,” *Science*, vol. 339, pp. 1169–1174, 2013.
- [9] M. Kjaergaard, M. E. Schwartz, J. Braumüller, P. Krantz, J. I.-J. Wang, S. Gustavsson, and W. D. Oliver, “Superconducting Qubits: Current State of Play,” *Annual Review of Condensed Matter Physics*, vol. 11, pp. 369–395, 2020.
- [10] E. Manousakis, “A Quantum-Dot Array as Model for Copper-Oxide Superconductors: A Dedicated Quantum Simulator for the Many-Fermion Problem,” *Journal of Low Temperature Physics*, vol. 126, pp. 1501–1513, 2002.
- [11] U. R. Fischer and R. Schützhold, “Quantum simulation of cosmic inflation in two-component Bose-Einstein condensates,” *Physical Review A*, vol. 70, p. 063615, 2004.
- [12] D. Porras and J. I. Cirac, “Effective Quantum Spin Systems with Trapped Ions,” *Physical Review Letters*, vol. 92, p. 207901, 2004.
- [13] A. M. Zagoskin, S. Savel’ev, and F. Nori, “Modeling an Adiabatic Quantum Computer via an Exact Map to a Gas of Particles,” *Physical Review Letters*, vol. 98, p. 120503, 2007.
- [14] I. Georgescu, S. Ashhab, and F. Nori, “Quantum simulation,” *Reviews of Modern Physics*, vol. 86, pp. 153–185, 2014.
- [15] S. Somaroo, C. H. Tseng, T. F. Havel, R. Laflamme, and D. G. Cory, “Quantum Simulations on a Quantum Computer,” *Physical Review Letters*, vol. 82, pp. 5381–5384, 1999.

- [16] D. Jaksch, C. Bruder, J. I. Cirac, C. W. Gardiner, and P. Zoller, “Cold Bosonic Atoms in Optical Lattices,” *Physical Review Letters*, vol. 81, pp. 3108–3111, 1998.
- [17] X.-L. Deng, D. Porras, and J. I. Cirac, “Quantum phases of interacting phonons in ion traps,” *Physical Review A*, vol. 77, p. 033403, 2008.
- [18] T. Byrnes, N. Y. Kim, K. Kusudo, and Y. Yamamoto, “Quantum simulation of Fermi-Hubbard models in semiconductor quantum-dot arrays,” *Physical Review B*, vol. 78, p. 075320, 2008.
- [19] M. Greiner, O. Mandel, T. Esslinger, T. W. Hänsch, and I. Bloch, “Quantum phase transition from a superfluid to a Mott insulator in a gas of ultracold atoms,” *Nature*, vol. 415, pp. 39–44, 2002.
- [20] F. Yamaguchi and Y. Yamamoto, “Quantum simulation of the t - J model,” *Superlattices and Microstructures*, vol. 32, pp. 343–345, 2002.
- [21] J. J. García-Ripoll, E. Solano, and M. A. Martin-Delgado, “Quantum simulation of Anderson and Kondo lattices with superconducting qubits,” *Physical Review B*, vol. 77, p. 024522, 2008.
- [22] J. Simon, W. S. Bakr, R. Ma, M. E. Tai, P. M. Preiss, and M. Greiner, “Quantum simulation of antiferromagnetic spin chains in an optical lattice,” *Nature*, vol. 472, pp. 307–312, 2011.
- [23] J. Struck, C. Ölschläger, R. L. Targat, P. Soltan-Panahi, A. Eckardt, M. Lewenstein, P. Windpassinger, and K. Sengstock, “Quantum Simulation of Frustrated Classical Magnetism in Triangular Optical Lattices,” *Science*, vol. 333, pp. 996–999, 2011.

- [24] L. Pollet, J. D. Picon, H. P. Büchler, and M. Troyer, “Supersolid Phase with Cold Polar Molecules on a Triangular Lattice,” *Physical Review Letters*, vol. 104, p. 125302, 2010.
- [25] A. Friedenauer, H. Schmitz, J. T. Glueckert, D. Porras, and T. Schaetz, “Simulating a quantum magnet with trapped ions,” *Nature Physics*, vol. 4, pp. 757–761, 2008.
- [26] M. Nakahara, *Geometry, Topology, and Physics*. London: A. Hilger, 1990.
- [27] K. V. Klitzing, G. Dorda, and M. Pepper, “New Method for High-Accuracy Determination of the Fine-Structure Constant Based on Quantized Hall Resistance,” *Physical Review Letters*, vol. 45, pp. 494–497, 1980.
- [28] R. B. Laughlin, “Quantized Hall conductivity in two dimensions,” *Physical Review B*, vol. 23, pp. 5632–5633, 1981.
- [29] D. J. Thouless, M. Kohmoto, M. P. Nightingale, and M. den Nijs, “Quantized Hall Conductance in a Two-Dimensional Periodic Potential,” *Physical Review Letters*, vol. 49, pp. 405–408, 1982.
- [30] M. V. Berry, “Quantal phase factors accompanying adiabatic changes,” *Proceedings of the Royal Society of London. A. Mathematical and Physical Sciences*, vol. 392, pp. 45–57, 1984.
- [31] F. D. M. Haldane, “Model for a Quantum Hall Effect without Landau Levels: Condensed-Matter Realization of the ”Parity Anomaly”, ” *Physical Review Letters*, vol. 61, pp. 2015–2018, 1988.

- [32] A. Altland and M. R. Zirnbauer, “Nonstandard symmetry classes in mesoscopic normal-superconducting hybrid structures,” *Physical Review B*, vol. 55, pp. 1142–1161, 1997.
- [33] A. P. Schnyder, S. Ryu, A. Furusaki, and A. W. W. Ludwig, “Classification of topological insulators and superconductors in three spatial dimensions,” *Physical Review B*, vol. 78, p. 195125, 2008.
- [34] S. Ryu, A. P. Schnyder, A. Furusaki, and A. W. W. Ludwig, “Topological insulators and superconductors: tenfold way and dimensional hierarchy,” *New Journal of Physics*, vol. 12, p. 065010, 2010.
- [35] D. C. Tsui, H. L. Stormer, and A. C. Gossard, “Two-Dimensional Magnetotransport in the Extreme Quantum Limit,” *Physical Review Letters*, vol. 48, pp. 1559–1562, 1982.
- [36] R. B. Laughlin, “Anomalous Quantum Hall Effect: An Incompressible Quantum Fluid with Fractionally Charged Excitations,” *Physical Review Letters*, vol. 50, pp. 1395–1398, 1983.
- [37] M. H. Anderson, J. R. Ensher, M. R. Matthews, C. E. Wieman, and E. A. Cornell, “Observation of Bose-Einstein Condensation in a Dilute Atomic Vapor,” *Science*, vol. 269, pp. 198–201, 1995.
- [38] C. C. Bradley, C. A. Sackett, J. J. Tollett, and R. G. Hulet, “Evidence of Bose-Einstein Condensation in an Atomic Gas with Attractive Interactions,” *Physical Review Letters*, vol. 75, pp. 1687–1690, 1995.
- [39] K. B. Davis, M. O. Mewes, M. R. Andrews, N. J. van Druten, D. S. Durfee,

- D. M. Kurn, and W. Ketterle, “Bose-Einstein Condensation in a Gas of Sodium Atoms,” *Physical Review Letters*, vol. 75, pp. 3969–3973, 1995.
- [40] B. DeMarco and D. S. Jin, “Onset of Fermi Degeneracy in a Trapped Atomic Gas,” *Science*, vol. 285, pp. 1703–1706, 1999.
- [41] F. Schreck, L. Khaykovich, K. L. Corwin, G. Ferrari, T. Bourdel, J. Cubizolles, and C. Salomon, “Quasipure Bose-Einstein Condensate Immersed in a Fermi Sea,” *Physical Review Letters*, vol. 87, p. 080403, 2001.
- [42] A. G. Truscott, K. E. Strecker, W. I. McAlexander, G. B. Partridge, and R. G. Hulet, “Observation of Fermi Pressure in a Gas of Trapped Atoms,” *Science*, vol. 291, pp. 2570–2572, 2001.
- [43] I. Bloch, J. Dalibard, and W. Zwerger, “Many-body physics with ultracold gases,” *Reviews of Modern Physics*, vol. 80, pp. 885–964, 2008.
- [44] I. Bloch, J. Dalibard, and S. Nascimbène, “Quantum simulations with ultracold quantum gases,” *Nature Physics*, vol. 8, pp. 267–276, 2012.
- [45] C. Chin, R. Grimm, P. Julienne, and E. Tiesinga, “Feshbach resonances in ultracold gases,” *Reviews of Modern Physics*, vol. 82, pp. 1225–1286, 2010.
- [46] W. Hofstetter, J. I. Cirac, P. Zoller, E. Demler, and M. D. Lukin, “High-Temperature Superfluidity of Fermionic Atoms in Optical Lattices,” *Physical Review Letters*, vol. 89, p. 220407, 2002.
- [47] D. Jaksch and P. Zoller, “The cold atom Hubbard toolbox,” *Annals of Physics*, vol. 315, pp. 52–79, 2005.

- [48] N. Cooper, J. Dalibard, and I. Spielman, “Topological bands for ultracold atoms,” *Reviews of Modern Physics*, vol. 91, p. 015005, 2019.
- [49] W. S. Bakr, J. I. Gillen, A. Peng, S. Fölling, and M. Greiner, “A quantum gas microscope for detecting single atoms in a Hubbard-regime optical lattice,” *Nature*, vol. 462, pp. 74–77, 2009.
- [50] J. F. Sherson, C. Weitenberg, M. Endres, M. Cheneau, I. Bloch, and S. Kuhr, “Single-atom-resolved fluorescence imaging of an atomic Mott insulator,” *Nature*, vol. 467, pp. 68–72, 2010.
- [51] M. Endres, M. Cheneau, T. Fukuhara, C. Weitenberg, P. Schauß, C. Gross, L. Mazza, M. C. Bañuls, L. Pollet, I. Bloch, and S. Kuhr, “Observation of Correlated Particle-Hole Pairs and String Order in Low-Dimensional Mott Insulators,” *Science*, vol. 334, pp. 200–203, 2011.
- [52] C. Weitenberg, M. Endres, J. F. Sherson, M. Cheneau, P. Schauß, T. Fukuhara, I. Bloch, and S. Kuhr, “Single-spin addressing in an atomic Mott insulator,” *Nature*, vol. 471, pp. 319–324, 2011.
- [53] D. Greif, M. F. Parsons, A. Mazurenko, C. S. Chiu, S. Blatt, F. Huber, G. Ji, and M. Greiner, “Site-resolved imaging of a fermionic Mott insulator,” *Science*, vol. 351, pp. 953–957, 2016.
- [54] M. F. Parsons, A. Mazurenko, C. S. Chiu, G. Ji, D. Greif, and M. Greiner, “Site-resolved measurement of the spin-correlation function in the Fermi-Hubbard model,” *Science*, vol. 353, pp. 1253–1256, 2016.
- [55] S. Taie, H. Ozawa, T. Ichinose, T. Nishio, S. Nakajima, and Y. Takahashi,

- “Coherent driving and freezing of bosonic matter wave in an optical Lieb lattice,” *Science Advances*, vol. 1, p. e1500854, 2015.
- [56] G.-B. Jo, J. Guzman, C. K. Thomas, P. Hosur, A. Vishwanath, and D. M. Stamper-Kurn, “Ultracold Atoms in a Tunable Optical Kagome Lattice,” *Physical Review Letters*, vol. 108, p. 045305, 2012.
- [57] A. Mielke, “Ferromagnetism in the Hubbard model on line graphs and further considerations,” *Journal of Physics A: Mathematical and General*, vol. 24, pp. 3311–3321, 1991.
- [58] G. Montambaux, L.-K. Lim, J.-N. Fuchs, and F. Piéchon, “Winding Vector: How to Annihilate Two Dirac Points with the Same Charge,” *Physical Review Letters*, vol. 121, p. 256402, 2018.
- [59] R. A. Williams, S. Al-Assam, and C. J. Foot, “Observation of Vortex Nucleation in a Rotating Two-Dimensional Lattice of Bose-Einstein Condensates,” *Physical Review Letters*, vol. 104, p. 050404, 2010.
- [60] M. Aidelsburger, M. Atala, S. Nascimbène, S. Trotzky, Y.-A. Chen, and I. Bloch, “Experimental Realization of Strong Effective Magnetic Fields in an Optical Lattice,” *Physical Review Letters*, vol. 107, p. 255301, 2011.
- [61] M. Aidelsburger, M. Atala, M. Lohse, J. T. Barreiro, B. Paredes, and I. Bloch, “Realization of the Hofstadter Hamiltonian with Ultracold Atoms in Optical Lattices,” *Physical Review Letters*, vol. 111, p. 185301, 2013.
- [62] H. Miyake, G. A. Siviloglou, C. J. Kennedy, W. C. Burton, and W. Ket-

- terle, “Realizing the Harper Hamiltonian with Laser-Assisted Tunneling in Optical Lattices,” *Physical Review Letters*, vol. 111, p. 185302, 2013.
- [63] M. Y. Azbel, “Energy spectrum of a conduction electron in a magnetic field,” *JETP*, vol. 19, p. 634, 1964.
- [64] P. G. Harper, “Single Band Motion of Conduction Electrons in a Uniform Magnetic Field,” *Proceedings of the Physical Society. Section A*, vol. 68, pp. 874–878, 1955.
- [65] D. R. Hofstadter, “Energy levels and wave functions of Bloch electrons in rational and irrational magnetic fields,” *Physical Review B*, vol. 14, pp. 2239–2249, 1976.
- [66] G. Jotzu, M. Messer, R. Desbuquois, M. Lebrat, T. Uehlinger, D. Greif, and T. Esslinger, “Experimental realization of the topological Haldane model with ultracold fermions,” *Nature*, vol. 515, pp. 237–240, 2014.
- [67] J. W. McIver, B. Schulte, F.-U. Stein, T. Matsuyama, G. Jotzu, G. Meier, and A. Cavalleri, “Light-induced anomalous Hall effect in graphene,” *Nature Physics*, vol. 16, pp. 38–41, 2020.
- [68] T. Oka and H. Aoki, “Photovoltaic Hall effect in graphene,” *Physical Review B*, vol. 79, p. 081406, 2009.
- [69] M.-S. Kim, M. Lee, J. H. Han, and Y. Shin, “Experimental apparatus for generating quantum degenerate gases of ytterbium atoms,” *Journal of the Korean Physical Society*, vol. 67, p. 1719–1725, 2015.

- [70] M. Lee, J. H. Han, J. H. Kang, M.-S. Kim, and Y. Shin, “Double resonance of Raman transitions in a degenerate Fermi gas,” *Physical Review A*, vol. 95, p. 043627, 2017.
- [71] T. W. Hansch. and B. Couillaud, “Laser frequency stabilization by polarization spectroscopy of a reflecting reference cavity,” *Optics Communications*, vol. 35, pp. 441–444, 1980.
- [72] D. J. McCarron, S. A. King, and S. L. Cornish, “Modulation transfer spectroscopy in atomic rubidium,” *Measurement Science and Technology*, vol. 19, p. 105601, 2008.
- [73] S. Taie, Y. Takasu, S. Sugawa, R. Yamazaki, T. Tsujimoto, R. Murakami, and Y. Takahashi, “Realization of a $SU(2) \times SU(6)$ System of Fermions in a Cold Atomic Gas,” *Physical Review Letters*, vol. 105, p. 190401, 2010.
- [74] S. Stellmer, R. Grimm, and F. Schreck, “Detection and manipulation of nuclear spin states in fermionic strontium,” *Physical Review A*, vol. 84, p. 043611, 2011.
- [75] M. Greiner, I. Bloch, O. Mandel, T. W. Hänsch, and T. Esslinger, “Exploring Phase Coherence in a 2D Lattice of Bose-Einstein Condensates,” *Physical Review Letters*, vol. 87, p. 160405, 2001.
- [76] M. Köhl, H. Moritz, T. Stöferle, K. Günter, and T. Esslinger, “Fermionic Atoms in a Three Dimensional Optical Lattice: Observing Fermi Surfaces, Dynamics, and Interactions,” *Physical Review Letters*, vol. 94, p. 080403, 2005.

- [77] J. Heinze, S. Götze, J. S. Krauser, B. Hundt, N. Fläschner, D.-S. Lühmann, C. Becker, and K. Sengstock, “Multiband Spectroscopy of Ultracold Fermions: Observation of Reduced Tunneling in Attractive Bose-Fermi Mixtures,” *Physical Review Letters*, vol. 107, p. 135303, 2011.
- [78] R. Wei and E. J. Mueller, “Magnetic-field dependence of Raman coupling in alkali-metal atoms,” *Physical Review A*, vol. 87, p. 042514, 2013.
- [79] N. Goldman and J. Dalibard, “Periodically Driven Quantum Systems: Effective Hamiltonians and Engineered Gauge Fields,” *Physical Review X*, vol. 4, p. 031027, 2014.
- [80] J. H. Shirley, “Solution of the Schrödinger Equation with a Hamiltonian Periodic in Time,” *Physical Review*, vol. 138, pp. B979–B987, 1965.
- [81] M. Bukov, L. D’Alessio, and A. Polkovnikov, “Universal high-frequency behavior of periodically driven systems: from dynamical stabilization to Floquet engineering,” *Advances in Physics*, vol. 64, pp. 139–226, 2015.
- [82] S. Rahav, I. Gilary, and S. Fishman, “Effective Hamiltonians for periodically driven systems,” *Physical Review A*, vol. 68, p. 013820, 2003.
- [83] M. M. Maricq, “Application of average Hamiltonian theory to the NMR of solids,” *Physical Review B*, vol. 25, pp. 6622–6632, 1982.
- [84] W. Magnus, “On the exponential solution of differential equations for a linear operator,” *Communications on Pure and Applied Mathematics*, vol. 7, pp. 649–673, 1954.

- [85] A. Eckardt and E. Anisimovas, “High-frequency approximation for periodically driven quantum systems from a Floquet-space perspective,” *New Journal of Physics*, vol. 17, p. 093039, 2015.
- [86] H. Lignier, C. Sias, D. Ciampini, Y. Singh, A. Zenesini, O. Morsch, and E. Arimondo, “Dynamical Control of Matter-Wave Tunneling in Periodic Potentials,” *Physical Review Letters*, vol. 99, p. 220403, 2007.
- [87] J. Struck, C. Ölschläger, M. Weinberg, P. Hauke, J. Simonet, A. Eckardt, M. Lewenstein, K. Sengstock, and P. Windpassinger, “Tunable Gauge Potential for Neutral and Spinless Particles in Driven Optical Lattices,” *Physical Review Letters*, vol. 108, p. 225304, 2012.
- [88] X. G. Wen, “Topological orders in rigid states,” *International Journal of Modern Physics B*, vol. 04, pp. 239–271, 1990.
- [89] S.-S. Chern, “On the Curvatura Integra in a Riemannian Manifold,” *Annals of Mathematics*, vol. 46, pp. 674–684, 1945.
- [90] W. P. Su, J. R. Schrieffer, and A. J. Heeger, “Solitons in Polyacetylene,” *Physical Review Letters*, vol. 42, pp. 1698–1701, 1979.
- [91] J. Zak, “Berry’s phase for energy bands in solids,” *Physical Review Letters*, vol. 62, pp. 2747–2750, 1989.
- [92] M. Creutz, “End States, Ladder Compounds, and Domain-Wall Fermions,” *Physical Review Letters*, vol. 83, pp. 2636–2639, 1999.
- [93] M. Atala, M. Aidelsburger, J. T. Barreiro, D. Abanin, T. Kitagawa, E. Demler, and I. Bloch, “Direct measurement of the Zak phase in topological Bloch bands,” *Nature Physics*, vol. 9, pp. 795–800, 2013.

- [94] O. Boada, A. Celi, J. I. Latorre, and M. Lewenstein, “Quantum Simulation of an Extra Dimension,” *Physical Review Letters*, vol. 108, p. 133001, 2012.
- [95] A. Celi, P. Massignan, J. Ruseckas, N. Goldman, I. Spielman, G. Juzelinis, and M. Lewenstein, “Synthetic Gauge Fields in Synthetic Dimensions,” *Physical Review Letters*, vol. 112, p. 043001, 2014.
- [96] M. Mancini, G. Pagano, G. Cappellini, L. Livi, M. Rider, J. Catani, C. Sias, P. Zoller, M. Inguscio, M. Dalmonte, and L. Fallani, “Observation of chiral edge states with neutral fermions in synthetic Hall ribbons,” *Science*, vol. 349, pp. 1510–1513, 2015.
- [97] B. K. Stuhl, H.-I. Lu, L. M. Ayccock, D. Genkina, and I. B. Spielman, “Visualizing edge states with an atomic Bose gas in the quantum Hall regime,” *Science*, vol. 349, pp. 1514–1518, 2015.
- [98] M. Z. Hasan and C. L. Kane, “Colloquium: Topological insulators,” *Reviews of Modern Physics*, vol. 82, pp. 3045–3067, 2010.
- [99] B. Song, L. Zhang, C. He, T. F. J. Poon, E. Hagiye, S. Zhang, X.-J. Liu, and G.-B. Jo, “Observation of symmetry-protected topological band with ultracold fermions,” *Science Advances*, vol. 4, p. eaao4748, 2018.
- [100] L. Livi, G. Cappellini, M. Diem, L. Franchi, C. Clivati, M. Frittelli, F. Levi, D. Calonico, J. Catani, M. Inguscio, and L. Fallani, “Synthetic Dimensions and Spin-Orbit Coupling with an Optical Clock Transition,” *Physical Review Letters*, vol. 117, p. 220401, 2016.
- [101] D. Hugel and B. Paredes, “Chiral ladders and the edges of quantum Hall insulators,” *Physical Review A*, vol. 89, p. 023619, 2014.

- [102] J. Jünemann, A. Piga, S.-J. Ran, M. Lewenstein, M. Rizzi, and A. Bermudez, “Exploring Interacting Topological Insulators with Ultracold Atoms: The Synthetic Creutz-Hubbard Model,” *Physical Review X*, vol. 7, p. 031057, 2017.
- [103] N. Sun and L.-K. Lim, “Quantum charge pumps with topological phases in a Creutz ladder,” *Physical Review B*, vol. 96, p. 035139, 2017.
- [104] X. Li, E. Zhao, and W. Vincent Liu, “Topological states in a ladder-like optical lattice containing ultracold atoms in higher orbital bands,” *Nature Communications*, vol. 4, p. 1523, 2013.
- [105] S.-L. Zhang and Q. Zhou, “Shaping topological properties of the band structures in a shaken optical lattice,” *Physical Review A*, vol. 90, p. 051601, 2014.
- [106] M. A. Khomehchi, C. Qu, M. E. Mossman, C. Zhang, and P. Engels, “Spin-momentum coupled Bose-Einstein condensates with lattice band pseudospins,” *Nature Communications*, vol. 7, p. 10867, 2016.
- [107] O. Dutta, M. Gajda, P. Hauke, M. Lewenstein, D.-S. Lühmann, B. A. Malomed, T. Sowiński, and J. Zakrzewski, “Non-standard Hubbard models in optical lattices: a review,” *Reports on Progress in Physics*, vol. 78, p. 066001, 2015.
- [108] C. L. Kane, R. Mukhopadhyay, and T. C. Lubensky, “Fractional Quantum Hall Effect in an Array of Quantum Wires,” *Physical Review Letters*, vol. 88, p. 036401, 2002.

- [109] E. Cornfeld and E. Sela, “Chiral currents in one-dimensional fractional quantum Hall states,” *Physical Review B*, vol. 92, p. 115446, 2015.
- [110] J.-M. Hou, “Hidden-Symmetry-Protected Topological Semimetals on a Square Lattice,” *Physical Review Letters*, vol. 111, p. 130403, 2013.
- [111] B. Liu, X. Li, and W. V. Liu, “Topological phases via engineered orbital hybridization in noncentrosymmetric optical lattices,” *Physical Review A*, vol. 93, p. 033643, 2016.
- [112] S. Barbarino, L. Taddia, D. Rossini, L. Mazza, and R. Fazio, “Synthetic gauge fields in synthetic dimensions: interactions and chiral edge modes,” *New Journal of Physics*, vol. 18, p. 035010, 2016.
- [113] X.-L. Qi and S.-C. Zhang, “Topological insulators and superconductors,” *Reviews of Modern Physics*, vol. 83, pp. 1057–1110, 2011.
- [114] N. Goldman, J. C. Budich, and P. Zoller, “Topological quantum matter with ultracold gases in optical lattices,” *Nature Physics*, vol. 12, pp. 639–645, 2016.
- [115] S. Kolkowitz, S. L. Bromley, T. Bothwell, M. L. Wall, G. E. Marti, A. P. Koller, X. Zhang, A. M. Rey, and J. Ye, “Spin–orbit-coupled fermions in an optical lattice clock,” *Nature*, vol. 542, pp. 66–70, 2017.
- [116] J. H. Han, J. H. Kang, and Y. Shin, “Band Gap Closing in a Synthetic Hall Tube of Neutral Fermions,” *Physical Review Letters*, vol. 122, p. 065303, 2019.

- [117] J. H. Kang, J. H. Han, and Y. Shin, “Realization of a Cross-Linked Chiral Ladder with Neutral Fermions in a 1D Optical Lattice by Orbital-Momentum Coupling,” *Physical Review Letters*, vol. 121, p. 150403, 2018.
- [118] N. Goldman, J. Dalibard, M. Aidelsburger, and N. R. Cooper, “Periodically driven quantum matter: The case of resonant modulations,” *Physical Review A*, vol. 91, p. 033632, 2015.
- [119] C. V. Parker, L.-C. Ha, and C. Chin, “Direct observation of effective ferromagnetic domains of cold atoms in a shaken optical lattice,” *Nature Physics*, vol. 9, pp. 769–774, 2013.
- [120] L.-C. Ha, L. W. Clark, C. V. Parker, B. M. Anderson, and C. Chin, “Roton-Maxon Excitation Spectrum of Bose Condensates in a Shaken Optical Lattice,” *Physical Review Letters*, vol. 114, p. 055301, 2015.
- [121] W. Zheng and H. Zhai, “Floquet topological states in shaking optical lattices,” *Physical Review A*, vol. 89, p. 061603, 2014.
- [122] A. Bermudez, D. Patanè, L. Amico, and M. A. Martin-Delgado, “Topology-Induced Anomalous Defect Production by Crossing a Quantum Critical Point,” *Physical Review Letters*, vol. 102, p. 135702, 2009.
- [123] L. Mazza, A. Bermudez, N. Goldman, M. Rizzi, M. A. Martin-Delgado, and M. Lewenstein, “An optical-lattice-based quantum simulator for relativistic field theories and topological insulators,” *New Journal of Physics*, vol. 14, p. 015007, 2012.
- [124] D. Sticlet, L. Seabra, F. Pollmann, and J. Cayssol, “From fractionally

- charged solitons to Majorana bound states in a one-dimensional interacting model,” *Physical Review B*, vol. 89, p. 115430, 2014.
- [125] L. Mazza, M. Aidelsburger, H.-H. Tu, N. Goldman, and M. Burrello, “Methods for detecting charge fractionalization and winding numbers in an interacting fermionic ladder,” *New Journal of Physics*, vol. 17, p. 105001, 2015.
 - [126] S. Barbarino, D. Rossini, M. Rizzi, R. Fazio, G. E. Santoro, and M. Dalmonte, “Topological Devil’s staircase in atomic two-leg ladders,” *New Journal of Physics*, vol. 21, p. 043048, 2019.
 - [127] T. L. Hughes, E. Prodan, and B. A. Bernevig, “Inversion-symmetric topological insulators,” *Physical Review B*, vol. 83, p. 245132, 2011.
 - [128] L. Li and S. Chen, “Hidden-symmetry-protected topological phases on a one-dimensional lattice,” *EPL (Europhysics Letters)*, vol. 109, p. 40006, 2015.
 - [129] M. Reitter, J. Näger, K. Wintersperger, C. Sträter, I. Bloch, A. Eckardt, and U. Schneider, “Interaction Dependent Heating and Atom Loss in a Periodically Driven Optical Lattice,” *Physical Review Letters*, vol. 119, p. 200402, 2017.
 - [130] T. Neupert, L. Santos, C. Chamon, and C. Mudry, “Fractional Quantum Hall States at Zero Magnetic Field,” *Physical Review Letters*, vol. 106, p. 236804, 2011.
 - [131] E. J. Bergholtz and Z. Liu, “Topological flat band models and fractional

- chern insulators,” *International Journal of Modern Physics B*, vol. 27, p. 1330017, 2013.
- [132] N. Goldman, F. Gerbier, and M. Lewenstein, “Realizing non-Abelian gauge potentials in optical square lattices: an application to atomic Chern insulators,” *Journal of Physics B: Atomic, Molecular and Optical Physics*, vol. 46, p. 134010, 2013.
- [133] X.-J. Liu, X. Liu, C. Wu, and J. Sinova, “Quantum anomalous Hall effect with cold atoms trapped in a square lattice,” *Physical Review A*, vol. 81, p. 033622, 2010.
- [134] T. Kitagawa, E. Berg, M. Rudner, and E. Demler, “Topological characterization of periodically driven quantum systems,” *Physical Review B*, vol. 82, p. 235114, 2010.
- [135] N. H. Lindner, G. Refael, and V. Galitski, “Floquet topological insulator in semiconductor quantum wells,” *Nature Physics*, vol. 7, pp. 490–495, 2011.
- [136] M. S. Rudner, N. H. Lindner, E. Berg, and M. Levin, “Anomalous Edge States and the Bulk-Edge Correspondence for Periodically Driven Two-Dimensional Systems,” *Physical Review X*, vol. 3, p. 031005, 2013.
- [137] M. C. Rechtsman, J. M. Zeuner, Y. Plotnik, Y. Lumer, D. Podolsky, F. Dreisow, S. Nolte, M. Segev, and A. Szameit, “Photonic Floquet topological insulators,” *Nature*, vol. 496, pp. 196–200, 2013.
- [138] L. J. Maczewsky, J. M. Zeuner, S. Nolte, and A. Szameit, “Observation of

- photonic anomalous Floquet topological insulators,” *Nature Communications*, vol. 8, p. 13756, 2017.
- [139] S. Mukherjee, A. Spracklen, M. Valiente, E. Andersson, P. Öhberg, N. Goldman, and R. R. Thomson, “Experimental observation of anomalous topological edge modes in a slowly driven photonic lattice,” *Nature Communications*, vol. 8, p. 13918, 2017.
 - [140] N. Fläschner, B. S. Rem, M. Tarnowski, D. Vogel, D.-S. Lühmann, K. Senstock, and C. Weitenberg, “Experimental reconstruction of the Berry curvature in a Floquet Bloch band,” *Science*, vol. 352, pp. 1091–1094, 2016.
 - [141] J. H. Kang, J. H. Han, and Y. Shin, “Creutz ladder in a resonantly shaken 1D optical lattice,” *New Journal of Physics*, vol. 22, p. 013023, 2020.
 - [142] D. J. Thouless, “Quantization of particle transport,” *Physical Review B*, vol. 27, pp. 6083–6087, 1983.
 - [143] L. Wang, M. Troyer, and X. Dai, “Topological Charge Pumping in a One-Dimensional Optical Lattice,” *Physical Review Letters*, vol. 111, p. 026802, 2013.
 - [144] S. Nakajima, T. Tomita, S. Taie, T. Ichinose, H. Ozawa, L. Wang, M. Troyer, and Y. Takahashi, “Topological Thouless pumping of ultracold fermions,” *Nature Physics*, vol. 12, pp. 296–300, 2016.
 - [145] M. Lohse, C. Schweizer, O. Zilberberg, M. Aidelsburger, and I. Bloch, “A Thouless quantum pump with ultracold bosonic atoms in an optical superlattice,” *Nature Physics*, vol. 12, pp. 350–354, 2016.

- [146] F. Mei, J.-B. You, D.-W. Zhang, X. C. Yang, R. Fazio, S.-L. Zhu, and L. C. Kwek, “Topological insulator and particle pumping in a one-dimensional shaken optical lattice,” *Physical Review A*, vol. 90, p. 063638, 2014.
- [147] M. Weinberg, C. Ölschläger, C. Sträter, S. Prella, A. Eckardt, K. Senstock, and J. Simonet, “Multiphoton interband excitations of quantum gases in driven optical lattices,” *Physical Review A*, vol. 92, p. 043621, 2015.
- [148] J. K. Asbóth, B. Tarasinski, and P. Delplace, “Chiral symmetry and bulk-boundary correspondence in periodically driven one-dimensional systems,” *Physical Review B*, vol. 90, p. 125143, 2014.
- [149] M. Fruchart, “Complex classes of periodically driven topological lattice systems,” *Physical Review B*, vol. 93, p. 115429, 2016.
- [150] D. Xiao, M.-C. Chang, and Q. Niu, “Berry phase effects on electronic properties,” *Reviews of Modern Physics*, vol. 82, pp. 1959–2007, 2010.
- [151] R. D. King-Smith and D. Vanderbilt, “Theory of polarization of crystalline solids,” *Physical Review B*, vol. 47, pp. 1651–1654, 1993.
- [152] R. Resta, “Manifestations of Berry’s phase in molecules and condensed matter,” *Journal of Physics: Condensed Matter*, vol. 12, pp. R107–R143, 2000.
- [153] P. Weinberg, M. Bukov, L. D’Alessio, A. Polkovnikov, S. Vajna, and M. Kolodrubetz, “Adiabatic perturbation theory and geometry of periodically-driven systems,” *Physics Reports*, vol. 688, pp. 1–35, 2017.

- [154] A. Dauphin, D.-T. Tran, M. Lewenstein, and N. Goldman, “Loading ultracold gases in topological Floquet bands: the fate of current and center-of-mass responses,” *2D Materials*, vol. 4, p. 024010, 2017.
- [155] L. D’Alessio and M. Rigol, “Long-time Behavior of Isolated Periodically Driven Interacting Lattice Systems,” *Physical Review X*, vol. 4, p. 041048, 2014.
- [156] T. Boulier, J. Maslek, M. Bukov, C. Bracamontes, E. Magnan, S. Lellouch, E. Demler, N. Goldman, and J. Porto, “Parametric Heating in a 2D Periodically Driven Bosonic System: Beyond the Weakly Interacting Regime,” *Physical Review X*, vol. 9, p. 011047, 2019.
- [157] K. Wintersperger, M. Bukov, J. Näger, S. Lellouch, E. Demler, U. Schneider, I. Bloch, N. Goldman, and M. Aidelsburger, “Parametric Instabilities of Interacting Bosons in Periodically Driven 1D Optical Lattices,” *Physical Review X*, vol. 10, p. 011030, 2020.
- [158] S. A. Weidinger and M. Knap, “Floquet prethermalization and regimes of heating in a periodically driven, interacting quantum system,” *Scientific Reports*, vol. 7, p. 45382, 2017.
- [159] K. Singh, C. Fujiwara, Z. Geiger, E. Simmons, M. Lipatov, A. Cao, P. Dotti, S. Rajagopal, R. Senaratne, T. Shimasaki, M. Heyl, A. Eckardt, and D. Weld, “Quantifying and Controlling Prethermal Nonergodicity in Interacting Floquet Matter,” *Physical Review X*, vol. 9, p. 041021, 2019.
- [160] A. Rubio-Abadal, M. Ippoliti, S. Hollerith, D. Wei, J. Rui, S. Sondhi,

- V. Khemani, C. Gross, and I. Bloch, “Floquet Prethermalization in a Bose-Hubbard System,” *Physical Review X*, vol. 10, p. 021044, 2020.
- [161] A. Herrmann, Y. Murakami, M. Eckstein, and P. Werner, “Floquet prethermalization in the resonantly driven Hubbard model,” *EPL (Europhysics Letters)*, vol. 120, p. 57001, 2017.
- [162] K. Mizuta, K. Takasan, and N. Kawakami, “High-frequency expansion for Floquet prethermal phases with emergent symmetries: Application to time crystals and Floquet engineering,” *Physical Review B*, vol. 100, p. 020301, 2019.
- [163] J. Kondo, “Resistance Minimum in Dilute Magnetic Alloys,” *Progress of Theoretical Physics*, vol. 32, pp. 37–49, 1964.
- [164] N. F. Mott, “Metal-Insulator Transition,” *Reviews of Modern Physics*, vol. 40, pp. 677–683, 1968.
- [165] R. Zhang, Y. Cheng, H. Zhai, and P. Zhang, “Orbital Feshbach Resonance in Alkali-Earth Atoms,” *Physical Review Letters*, vol. 115, p. 135301, 2015.
- [166] G. Pagano, M. Mancini, G. Cappellini, L. Livi, C. Sias, J. Catani, M. Inguscio, and L. Fallani, “Strongly Interacting Gas of Two-Electron Fermions at an Orbital Feshbach Resonance,” *Physical Review Letters*, vol. 115, p. 265301, 2015.
- [167] M. Höfer, L. Riegger, F. Scazza, C. Hofrichter, D. Fernandes, M. Parish, J. Levinsen, I. Bloch, and S. Fölling, “Observation of an Orbital Interaction-Induced Feshbach Resonance in ^{173}Yb ,” *Physical Review Letters*, vol. 115, p. 265302, 2015.

- [168] D. Cocks, P. P. Orth, S. Rachel, M. Buchhold, K. Le Hur, and W. Hofstetter, “Time-Reversal-Invariant Hofstadter-Hubbard Model with Ultracold Fermions,” *Physical Review Letters*, vol. 109, p. 205303, 2012.
- [169] P. P. Orth, D. Cocks, S. Rachel, M. Buchhold, K. L. Hur, and W. Hofstetter, “Correlated topological phases and exotic magnetism with ultracold fermions,” *Journal of Physics B: Atomic, Molecular and Optical Physics*, vol. 46, p. 134004, 2013.
- [170] H. Guo and S.-Q. Shen, “Topological phase in a one-dimensional interacting fermion system,” *Physical Review B*, vol. 84, p. 195107, 2011.
- [171] M. Dzero, K. Sun, V. Galitski, and P. Coleman, “Topological Kondo Insulators,” *Physical Review Letters*, vol. 104, p. 106408, 2010.
- [172] V. Alexandrov, M. Dzero, and P. Coleman, “Cubic Topological Kondo Insulators,” *Physical Review Letters*, vol. 111, p. 226403, 2013.
- [173] M. Dzero, J. Xia, V. Galitski, and P. Coleman, “Topological Kondo Insulators,” *Annual Review of Condensed Matter Physics*, vol. 7, pp. 249–280, 2016.
- [174] V. Alexandrov and P. Coleman, “End states in a one-dimensional topological Kondo insulator in large- N limit,” *Physical Review B*, vol. 90, p. 115147, 2014.
- [175] A. M. Lobos, A. O. Dobry, and V. Galitski, “Magnetic End States in a Strongly Interacting One-Dimensional Topological Kondo Insulator,” *Physical Review X*, vol. 5, p. 021017, 2015.

- [176] F. T. Lisandrini, A. M. Lobos, A. O. Dobry, and C. J. Gazza, “Topological Kondo insulators in one dimension: Continuous Haldane-type ground-state evolution from the strongly interacting to the noninteracting limit,” *Physical Review B*, vol. 96, p. 075124, 2017.
- [177] J. C. Pillay and I. P. McCulloch, “Topological phase transition and the effect of Hubbard interactions on the one-dimensional topological Kondo insulator,” *Physical Review B*, vol. 97, p. 205133, 2018.
- [178] A. Lazarides, A. Das, and R. Moessner, “Equilibrium states of generic quantum systems subject to periodic driving,” *Physical Review E*, vol. 90, p. 012110, 2014.
- [179] E. Canovi, M. Kollar, and M. Eckstein, “Stroboscopic prethermalization in weakly interacting periodically driven systems,” *Physical Review E*, vol. 93, p. 012130, 2016.
- [180] A. Chandran and S. L. Sondhi, “Interaction-stabilized steady states in the driven $O(N)$ model,” *Physical Review B*, vol. 93, p. 174305, 2016.
- [181] N. H. Lindner, E. Berg, and M. S. Rudner, “Universal Chiral Quasisteady States in Periodically Driven Many-Body Systems,” *Physical Review X*, vol. 7, p. 011018, 2017.
- [182] D. Abanin, W. De Roeck, W. W. Ho, and F. Huveneers, “A Rigorous Theory of Many-Body Prethermalization for Periodically Driven and Closed Quantum Systems,” *Communications in Mathematical Physics*, vol. 354, pp. 809–827, 2017.

- [183] M. Messer, K. Sandholzer, F. Görg, J. Minguzzi, R. Desbuquois, and T. Esslinger, “Floquet Dynamics in Driven Fermi-Hubbard Systems,” *Physical Review Letters*, vol. 121, p. 233603, 2018.

초 록

물질의 상은 Landau 이론에 따라 자발적인 대칭성 깨짐으로 분류되어 왔다. 그러나 양자 홀 효과의 발견은 물질의 상을 분류하는 새로운 패러다임을 제시하게 되었다. 양자 홀 효과의 상태들은 대칭성이 깨지지 않지만, 밴드 구조의 위상적 불변 수에 따라 그 상이 결정되게 된다. 위상적 불변수에 의해 결정되고 미세한 변화에 둔감한 물리적 성질들을 특징으로, 위상적 물질들은 현대 응집물질 물리의 최전방을 대표하게 되었다.

상호작용하는 위상 절연체와 같은 복잡한 양자 다체 시스템은 현대 물리의 어려운 문제로 남아있다. 광격자내의 초저온 원자들은 외부 환경에 대해 잘 고립되어 있고 원자간 상호작용을 포함한 실험 요소들을 쉽게 조절할 수 있어 상호작용하는 위상 물리를 탐구하기에 적합하다. Harper-Hofstadter 모델과 Haldane 모델과 같은 잘 알려진 격자 모델을 참고하면 격자 내에 강한 자기장을 도입하거나 next-nearest-neighbor 터널링을 도입함으로써 위상 밴드들을 만들 수 있다. 이 학위논문에서는 공진하는 변조를 이용한 1차원 광격자에서 위상 사다리를 구현한 일들을 다룬다. 1차원 광격자의 Bloch 상태들을 인공 차원으로 간주하여 실제 광격자점과 같이 사다리 모델을 구성하게 된다.

고정된 광격자에 움직이는 광격자를 도입함으로써 생성되는 Bloch 상태 간의 복소 터널링 위상에 대하여 연구하였다. 만들어진 인공 사다리 모델에서 원자가 단위 격자를 한바퀴 돌게 되면 위상을 얻게되는데, 이는 전하를 띤 입자가 자기장 내에서 얻게되는 Aharonov-Bohm 위상과 동등한 것이다. 생성된 인공 게이지 장은 시간 반전 대칭을 깨트려 Harper-Hofstadter 모델과 비슷한 상황을 만들어낸다. 밴드 상태와 운동량 분석을 통해 비대칭 바닥상태를 직접 관측하였고, 생성된 비대칭 바닥상태의 안정성도 조사할 수 있었다. 시스템을 갑자기 변화시켰을 때 나타나는 동역학도 시스템 내에 균일하고 강한 게이지 장이 존재

한다는 것을 입증할 수 있었고, 또한 이의 운동량 의존성은 인공 사다리 모델에서 특징적인 next-nearest-neighbor 터널링이 존재한다는 것을 의미한다.

격자 위치가 공진운동하는 1차원 광격자를 이용해 Creutz 사다리를 구현하였다. 광격자를 흔드는 주파수가 두 밴드 상태간 에너지 차이의 절반이 되는 조건이 되면, 이광자 과정을 통해 밴드 상태가 바뀌는 nearest-neighbor 터널링이 유도되고, 이는 사다리 모델로 기술할 때 next-nearest-neighbor 터널링과 같다. 이러한 대각선 터널링은 Brillouin 영역에서 유사 스핀의 꼬임 구조를 만들고 위상 끝 상태를 형성한다. 측정된 공진 주파수와 간섭 결과들은 유효 해밀토니안이 위상적 유사 스핀 꼬임 구조를 가지고 있다는 것을 명확히 보여준다. 더 나아가 위상 전하 펌프 구현을 위해 1차원 광격자를 두개의 배음 주파수로 변조하는 방법을 제안하였다.

주요어 : 초저온 원자, 페르미 기체, 위상 절연체, 위상 사다리, 플로케 시스템,
위상 전하 펌프

학 번 : 2015-30971